LDV MEASUREMENTS AND ANALYSIS OF GAS AND PARTICULATE PHASE VELOCITY PROFILES IN A VERTICAL JET PLUME IN A 2D BUBBLING FLUIDIZED BED

by

Alexander G. Mychkovsky

A dissertation submitted in partial fulfillment
of the requirements for the degree of
Doctor of Philosophy
(Mechanical Engineering)
in The University of Michigan
2010

Doctoral Committee:

      Professor Steven L. Ceccio, Co-Chair
      Professor Volker Sick, Co-Chair
      Professor Marc Perlin
      Professor Jennifer Sinclair Curtis, University of Florida

To Mulligan

ACKNOWLEDGMENTS

TABLE OF CONTENTS

LIST OF FIGURES

LIST OF TABLES

NOMENCLATURE

A	Cross-sectional area
A_S	Surface area of an individual particle
Ar	Archimedes' Number
b	Half of the jet plume width
C	Speed of light
C_B	Speed of acoustic wave in a Bragg Cell
C_D	Particle drag coefficient
C_1	3D correction coefficient for the velocity profile
C_2	3D correction coefficient for the velocity profile squared
d_p	Diameter of an individual particle
D_j	Jet orifice diameter
D_m	LDV measurement volume diameter
f	Frequency
f_D	Force of drag on the particulate phase
F_D	Force of drag on an individual particle
g	acceleration of gravity
H	Height of emulsion with respect to fluidization distributor surface
I	Intensity
j	Momentum rate

k	Optical wave number
K_1, K_2	Ergun equation constants
L	Laser beam diameter
$\dot{m}$	Mass flow rate
$\dot{m}_o$	Mass flow rate of gas that originates at the jet inlet orifice
n	Index of refraction
P	Pressure
q	Acoustic wave number
$\dot{Q}$	Volumetric flow rate
r	Optical amplitude reflectance
R	Optical intensity reflectance
Re	Reynolds number
T	Temperature
v	Local, mean vertical component of velocity
V	Spatially averaged, mean vertical component of velocity
$\mathcal{V}_p$	Volume of an individual particle
w	Width of the bed gap
w_p	Weight of the particulate phase
W_p	Weight of an individual particle
x	Transverse (horizontal) coordinate
$x_{1/2}$	Half-velocity point
y	Axial (vertical) coordinate
y_o	Virtual origin location

z	3rd dimension coordinate across the bed gap

Greek Letters

δ_f	Fringe spacing in LDV measurement volume
Λ	acoustic wave length
λ	Optical wave length
ε	Volumetric void fraction
ρ	Density
μ	Viscosity
θ	Angle of laser beam with respect to the Bragg Cell
φ	Angle of laser beam intersection at LDV measurement volume
ϕ	Particle sphericity
Ω	Angular frequency
η	Transverse coordinate scaled with respect to the axial distance from the virtual origin
ζ	Transverse coordinate scaled with respect to half the width of the jet plume
ξ	Transverse coordinate scaled with respect to the half-velocity point.

Subscripts

avg	Average value with respect to the 3rd dimension across the bed gap
b	Bed
B	Bragg
D	Drag

Lc	Laser cavity length
g	Gas phase
j	Jet inlet value
fl	Fluidization
m	Maximum transverse value at a given axial distance
mf	Minimum fluidization
p	Particulate phase
peak	Maximum value with respect to the 3rd dimension across the bed gap
s	Slip

Acronyms

HDPE	High density polyethylene
LDV	Laser Doppler velocimetry
SMD	Sauter mean diameter
UHMW	Ultra-high molecular weight
VMD	Volume mean diameter
2D	Two dimensional
3D	Three dimensional

ABSTRACT

Fluidized beds are commonly used as chemical reactors and solid fuel combustors, where high-speed gas jets are employed to introduce reactants to the system. Quantitative gas and particulate phase velocity measurements are needed to characterize the transport phenomena of these jet plumes into the particulate emulsion. Two component Laser Doppler velocimetry (LDV) was used to investigate the gas and particulate phase velocities and resulting transport of a vertically injected gas jet plume in a two-dimensional bubbling bed.

LDV measurements of this optically dense multiphase flow are challenging due to laser intensity fluctuations, which mix with the recorded burst frequencies. This problem was resolved by optimizing the Bragg Cell configuration and burst signal processing. The jet gas was seeded with ice crystals, and bursts from the bed particles and gas tracers were simultaneously acquired. These bursts were differentiated based on their intensity and coincidence to determine the gas and particulate phase velocities.

The behavior of the single-phase gas jet in the empty bed was examined. The self-similar velocity profile growth was consistent the development of a free two-dimensional turbulent jet. The bed was filled with high-density polyethylene microspheres. The gas and particulate phase velocity profiles of the jet were measured. Similarity profiles are presented and the resulting void fraction, mass flow and momentum transport calculations are analyzed. The effect of fluidization velocity on the jet dynamics was examined and was shown to influence the rate of mass entrainment into the jet plume and the momentum exchange between the phases.

The ratio of the maximum gas and particulate phase velocities appeared to follow a similar trend for all test conditions. Hence, the ratio of the drag force coupling to the particulate or gas phase momentum is constant at a given axial location from the jet inlet. Additionally, the mass-averaged velocity ratio for the two phases, which is equivalent to

the ratio of the centerline velocities, develops in a similar fashion. This phenomenon is observed for high-speed gas jets in bubbling beds with spherical particle entrainment when $Re_p > 1,000$ so that $C_D \sim 0.4$.

CHAPTER 1:

INTRODUCTION

This introduction provides an overview of fluidized beds and prior work regarding jets in bubbling beds. The subsequent chapters describe the measurement techniques, data analysis, and results of this research.

1.1 Bubbling Fluidized Beds

1.1.1 Definition and Applications

In its simplest form, a fluidized bed is created by blowing gas upwards through a confined emulsion of particles. The gas flow rate must be sufficient so that it exerts a vertical drag force on the particles that counteracts their effective weight. This reduces the contact friction between the solid particles to such a level that they are able move about one another with ease. Therefore the gas-particle ensemble in the fluidized bed behaves like a liquid, free to flow and deform.

Fluidized beds are often employed because of their high mixing and heat transfer rates. They are predominately used as chemical processors for polyethylene synthesis, catalytic cracking, and coal or biomass gasification. They are also used for physical processes such as coating and drying in pharmaceuticals. Within the past several years, there has been a renewed interest in fluidized bed combustors in the energy industry. Pulverized coal can be burned nearly isothermally at temperatures below those at which NO_X forms. Additionally, SO_X emission is significantly reduced because the combustion gasses are sufficiently mixed with a sulfur absorbing chemical, typically limestone. This type of fluidized bed combustor is a so-called 'clean coal power plant', which requires little or no external emission controls such as scrubbers.

1.1.2 Components

The basic components of a fluidized bed system are illustrated in Figure 1.1 (Pell, 1990). The distributor is a grid or porous plate that supports the solid particles. Gas is introduced into the bed emulsion at a superficial velocity from the plenum through the distributor. The riser is considered the entire tall vertical section consisting of the fluidized bed region, transitional splash zone and freeboard region. In practical applications, mechanical devices such as heat exchanger tubes and baffles are located in the fluidized bed emulsion. At the top of the riser, cyclones capture and return entrained bed material.
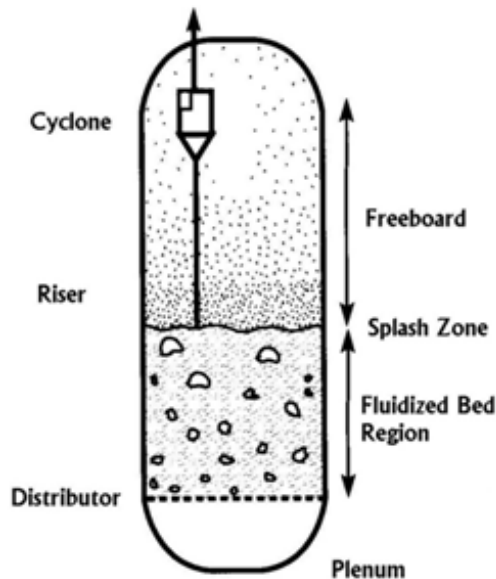
Figure 1.1: Basic components of a bubbling fluidized bed (Pell, 1990). Gas flows upwards through the distributor plate to fluidize the particulate emulsion. Bubbles can form in the emulsion and some particles are entrained along the height of the riser where they are captured by the cyclone in the dilute freeboard region.

1.1.3 Fluidization Regimes and Powder Classifications

When solid particles are fluidized, the emulsion behavior depends on the degree of fluidization as well as the particulate and fluid phase properties. When the gas flows through the bed at a very low rate, the emulsion is not disturbed and acts as a porous medium. This condition is called a packed or fixed bed. As the fluidization flow rate is increased, the emulsion begins to expand. The particles still remain largely in contact

2

with each other; however they begin to move slightly; vibrating, rotating, and jostling about. The Ergun equation (1.1) was developed to relate the pressure drop in a packed bed to the gas flow rate and the properties of the solids and gas phases. It is a semi-empirical relationship that presents the sum of viscous and inertial contributions, respectively. At low flow rates the viscous forces dominate so that the pressure drop is linearly related to the superficial fluidization velocity.

$$\frac{\Delta P}{H} = 150 \frac{(1-\varepsilon)^2}{\varepsilon^3} \frac{\mu_g V_{fl}}{(\phi d_p)^2} + 1.75 \frac{(1-\varepsilon)}{\varepsilon^3} \frac{\rho_g V_{fl}^2}{\phi d_p}$$
(1.1)

Once the drag force of the interstitial gas balances the effective weight (considering gravity and buoyancy) of the particulate emulsion, the bed has reached the fluidized state. The drag force per unit area is equivalent to the vertical gas pressure drop across the particulate emulsion, and therefore can be related to solids hold up according to equation (1.2).

$$\frac{\Delta P}{H} = (\rho_p - \rho_g)(1 - \varepsilon_{mf})g$$
(1.2)

Often, the density of the particles is several orders of magnitude greater than the density of the fluidizing gas. When applying the Ergun equation, one has to know the minimum fluidization voidage, ε_{mf}, which is difficult to accurately measure and is thus frequently unknown. Wen & Yu (1966) developed an expression for the minimum fluidization velocity for a range of particle types and sizes by assuming the following approximations to hold based on experimental data:

$$\frac{(1-\varepsilon_{mf})^2}{\varepsilon_{mf}^3 \phi^2} \qquad \frac{1}{\varepsilon_{mf}^3 \phi} \qquad \text{are constant}$$

Combining the above equations, a dimensionless form of the Ergun equation can be expressed in terms of the particle Reynolds number and Archimedes number

$$Re_{mf} = \left(K_1^2 + K_2 Ar_p\right)^{1/2} - K_1$$
(1.3)

where

$$Re_{mf} = \frac{V_{mf} d_p \rho_g}{\mu_g}$$
(1.4)

3

$$Ar_p = \frac{d_p^3 \rho_g (\rho_p - \rho_g) g}{\mu_g^2} \tag{1.5}$$

For fine particles, $K_1 = 33.7$ and $K_2 = 0.0408$ (Wen & Yu, 1966) and for coarse particles, $K_1 = 28.7$ and $K_2 = 0.0494$ (Chitester *et al.*, 1984). Since the bulk emulsion is stationary, the total mass of the solids is constant.

$$M_p = \rho_p (1 - \varepsilon_{mf}) H A_b \tag{1.6}$$

Therefore, the combination of equations (1.2) and (1.6) indicates that the pressure drop across a fluidized emulsion is constant. In fact, the value of the minimum fluidization velocity is usually determined experimentally by either 1) gradually increasing the fluidization velocity in a packed bed and noting where the pressure drop stops changing or 2) gradually decreasing the fluidization velocity in a bubbling bed and noting where the pressure drop begins decreasing (Figure 1.2). The slight hysteresis between the fluidization and defluidization curves is due to stationary friction forces and can be exacerbated by additional inter-particle forces due to electrostatic charge and surface cohesion.
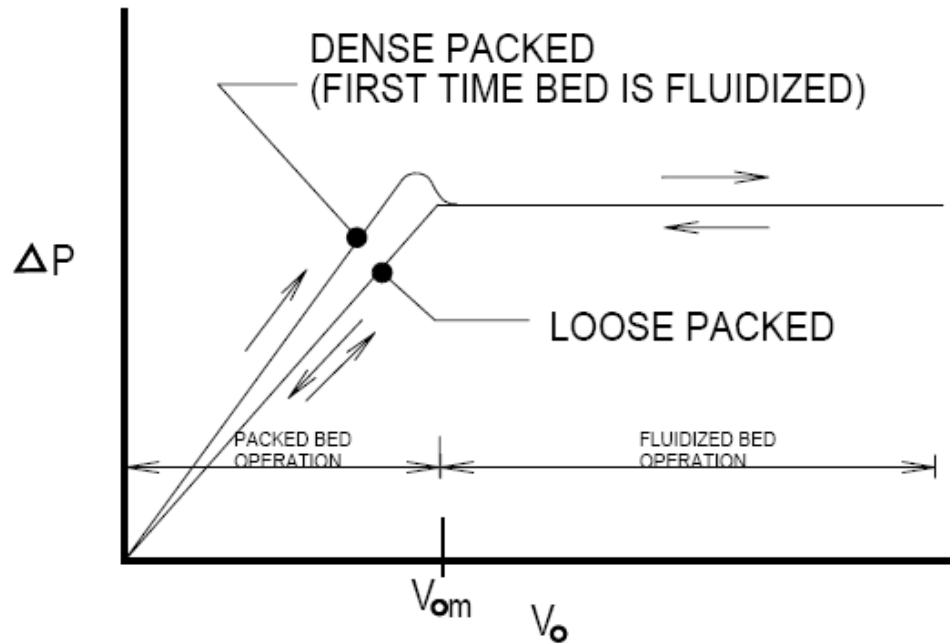
Figure 1.2: Fluidization curve (Chase, 2010). Here V_o is the fluidization velocity. The pressure drop increases linearly with fluidization velocity in the packed bed regime. Once the particulate emulsion is fluidized, the pressure drop remains constant and is equivalent to the effective weight of the particulate phase per unit bed cross-sectional area.

4

The dynamics of the emulsion beyond the minimum fluidization velocity depends on the properties of the particles in the emulsion. The emulsion can either experience meta-stable expansion, bubble, or channel and jet. One of the first successful attempts to classify solid particle fluidization properties was carried out by Geldart. Geldart (1986) created a sort of 'phase diagram', shown in Figure 1.3, which can be used to characterize powder behavior in a fluidized bed. The corresponding modes of fluidization are illustrated in Figure 1.3.
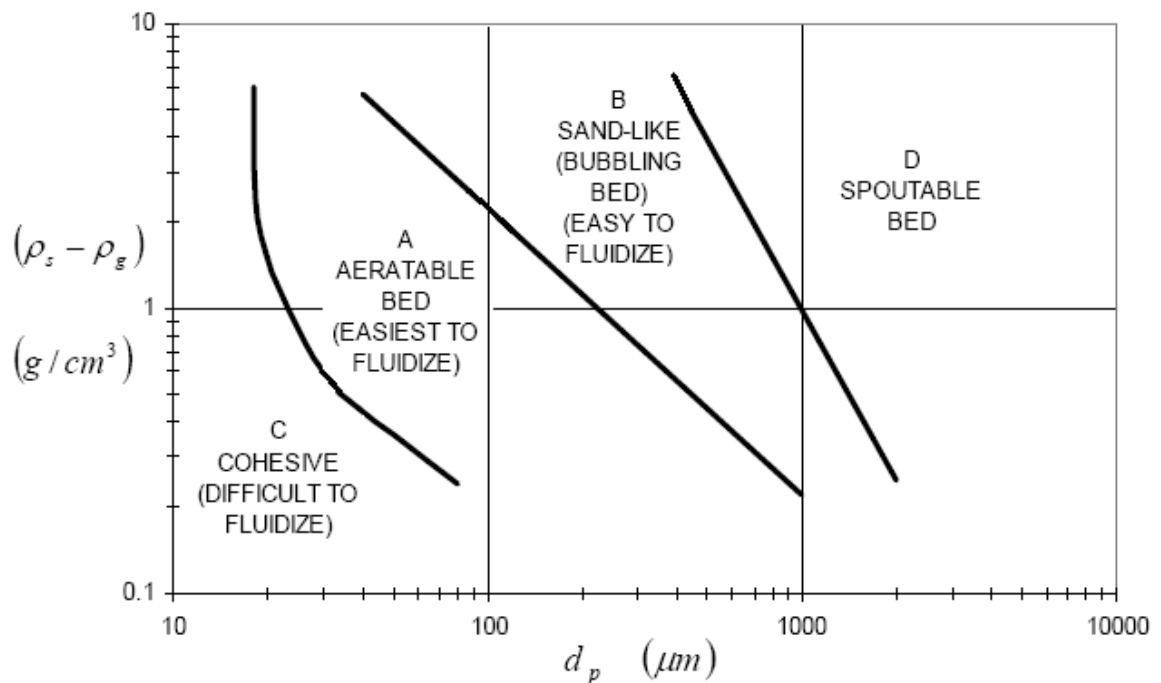
Figure 1.3: Geldart powder classifications (Geldart, 1986). Emulsion behavior is based on particle size and density.
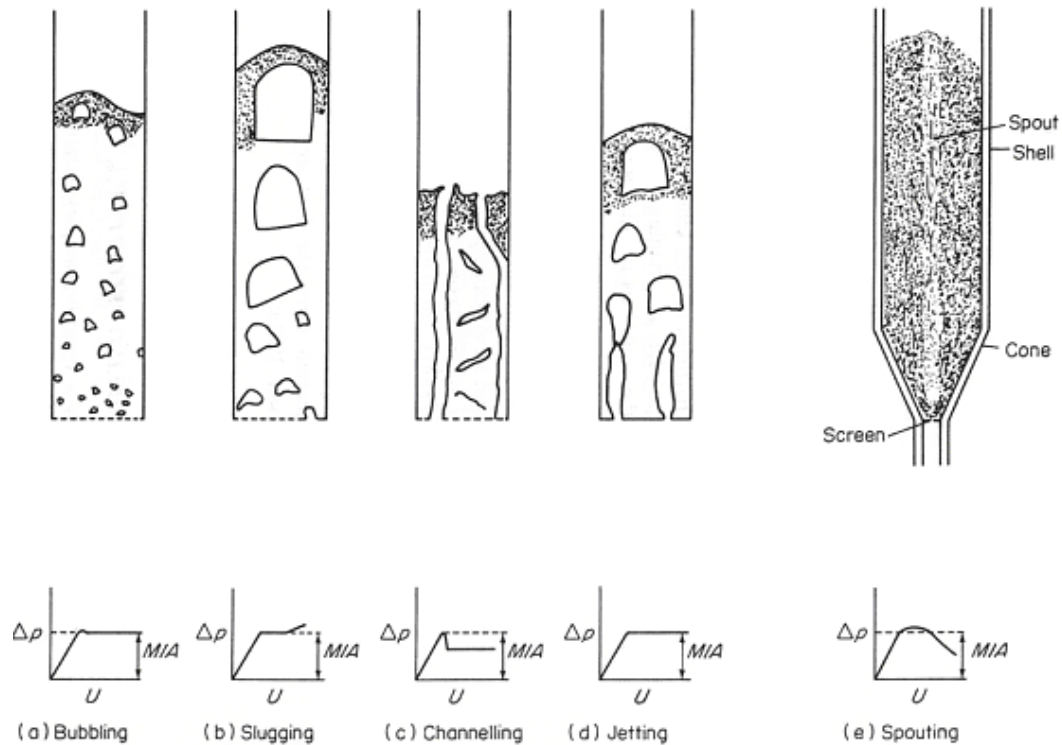
Figure 1.4: Geldart modes of fluidization for the various powder types described in Figure 1.3 (Geldart, 1986).

Group A particles are low density with mean diameters of about 20 to 100 μm. This aeratable powder is characterized by rapid mixing and gross circulation. Fluid cracking catalysts typically are in this category. These particles form a slightly cohesive structure, which allows for metastable expansion of the bed between the minimum fluidization and bubbling states. Bubbles rise faster than the interstitial gas and the small average particle size promotes the bubble splitting so that a maximum stable bubble size can be shown to exist.

Group B powders are composed of dense, sand-like particles. There is little powder circulation in the absence of bubbles. Interparticle forces in this bed structure are negligible. Once the minimum fluidization flow rate is exceeded, the excess gas forms small bubbles at the distributor surface which grow as they ascend through the particulate emulsion. Bubbles in a bed of group B particles can grow to considerable size, which is limited by the riser geometry rather than the particle size.

Group C powders consist of small particles, usually less than 20 μm in diameter. These particles are moist or sticky, soft and irregularly shaped. This produces a bed

structure in which interparticle forces (cohesive, electrostatic, etc.) overcome those exerted by the fluid onto the particles. This makes fluidization difficult, and the powder will often lift as a plug in small diameter tubes or form channels in large diameter tubes.

Group D particles are large (on the order of a millimeter) and dense and they are difficult to fluidize in deep beds. Bubbles rise slower than the interstitial gas. Therefore gas actually flows upwards through the bubbles, which can lead to jets forming in the bed and spouting at the surface, especially if the fluidization gas distribution is uneven.

It is important to note that theories based on data from one group are not necessarily applicable to another. One should also keep in mind that changing the temperature, pressure, or humidity of the fluidizing gas may affect the behavior of the powder, especially if it happens near a 'phase boundary', depicted in Figure 1.3.

As the fluidization velocity is increased beyond the minimum fluidization value, the emulsion void fraction increases and mixing becomes more rapid and turbulent for all types of particles. The range of fluidization regimes for group B particles is illustrated in Figure 1.5 (Gracie & Bi, 1997). When the fluidization velocity exceeds the particle terminal velocity, the entire emulsion of particles is advected downstream. This type of pneumatic particle transport is known as a circulating fluidized bed. The scope of this research is primarily limited to group B particles operating in the bubbling regime.

INCREASING U, ε

| FIXED BED OR DELAYED BUBBLING | BUBBLING REGIME | SLUGGING REGIME | TURBULENT REGIME | FAST FLUIDIZATION | PNEUMATIC CONEYING |

AGGREGATIVE FLUIDIZATION
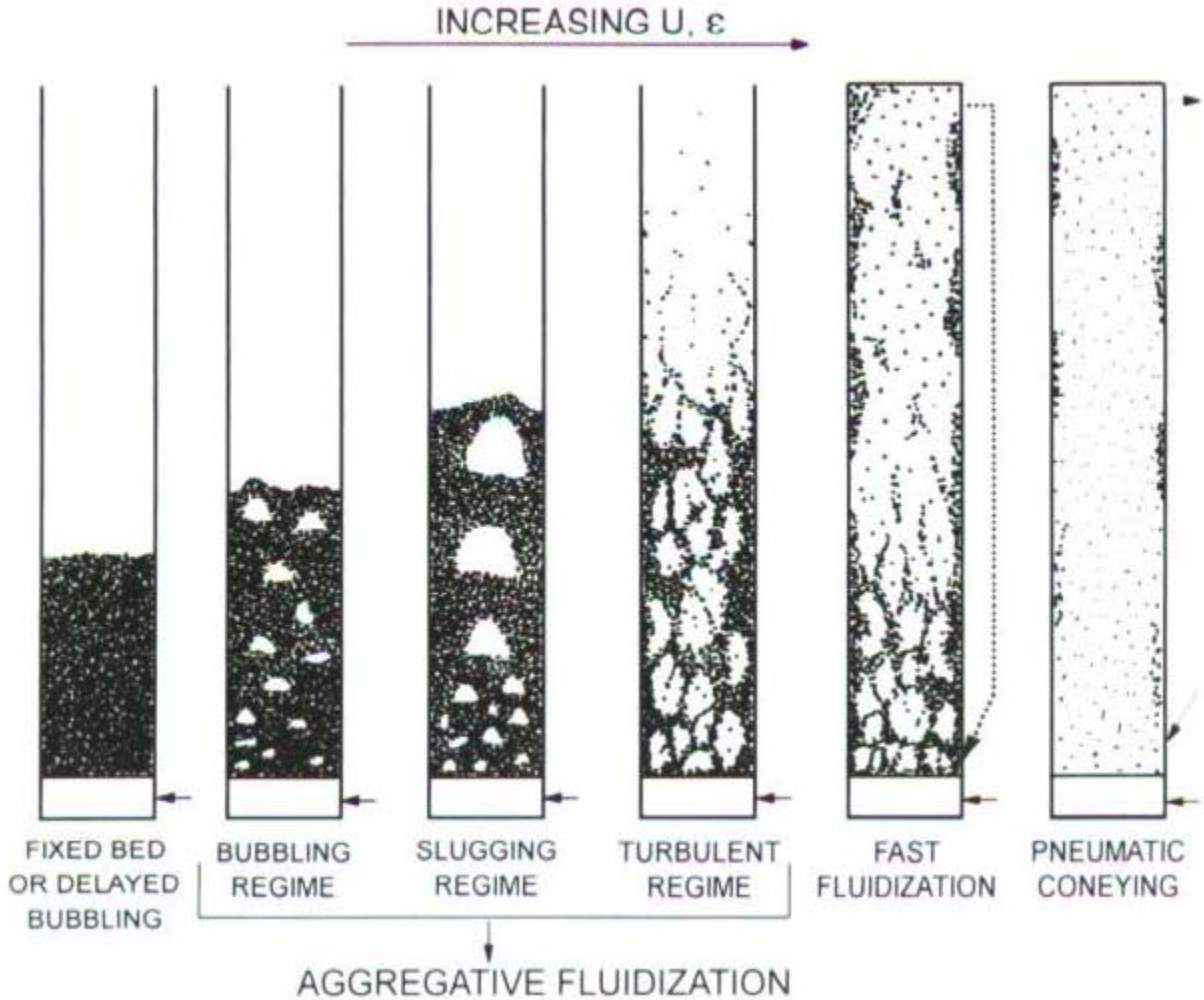
Figure 1.5: Fluidization regimes for Geldart group B particles as a function of fluidization velocity (Grace & Bi, 1997).

1.2 Jets in Fluidized Beds

1.2.1 Overview

As mentioned earlier, fluidized beds are employed as chemical reactors and solid fuel combustors due to their rapid transport. In many system configurations, gas jets are injected into the bubbling particulate emulsion. For example, jets of steam and air are sprayed into fluidized bed reactors during the gasification of coal or biomass.

The jet phenomenon is key to the efficiency of the process since the jet plume is a region of rapid mass, momentum, and energy transfer. The mass transfer determines rate

8

of chemical reactions. The momentum transfer determines plume dynamics (penetration and fluctuations), which needs to be understood so that mechanical damage of internal bed components such as pipes and baffles can be prevented. For reactor/combustor design considerations, the time scales of particle transport are important relative to the processes that are occurring inside the jet region.

When a gas jet is injected into a bubbling bed, particles and interstitial gas in the emulsion are entrained into the jet plume. The nature of the entrainment and subsequent momentum transfer are still not completely understood due, in part, to lack of experimental data. This is because the gas-particle flow is largely opaque in the bubbling emulsion and extremely harsh and abrasive in the jet plume. Therefore, largely empirical relations are often used to describe the jet dynamics. A photograph of a vertical gas jet in the laboratory two-dimensional bubbling bed is shown in Figure 1.6 and a schematic of a horizontal gas jet is illustrated in Figure 1.7 (Xuereb *et al.*, 1992).
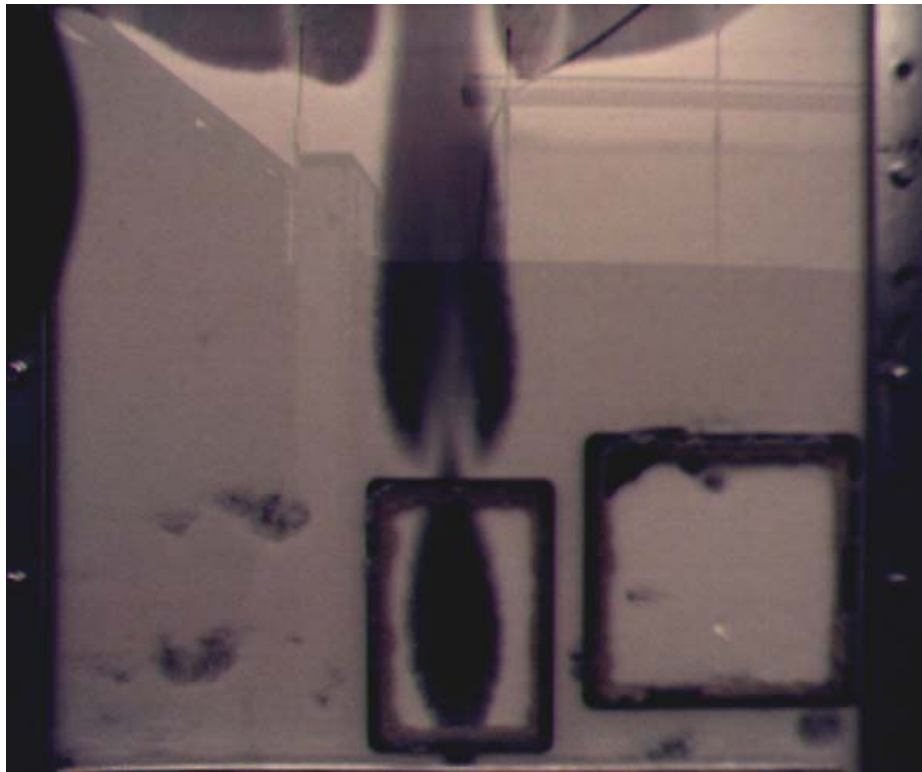
Figure 1.6: Vertical gas jet in the laboratory 2D bubbling fluidized bed. The bed dimensions are 457 mm wide by 1 m tall with a 12.7 mm gap. The walls are transparent acrylic with 102 mm by 153 mm by 5 mm thick quartz viewing windows inserted 50 mm above the vertical jet inlet orifice, which is 9.2 mm in diameter. The square quartz windows may be used for horizontal jet experiments in the future. The vertical jet is located midway across the porous polyethylene fluidization distributor. The particle emulsion is white and the jet plume is black.
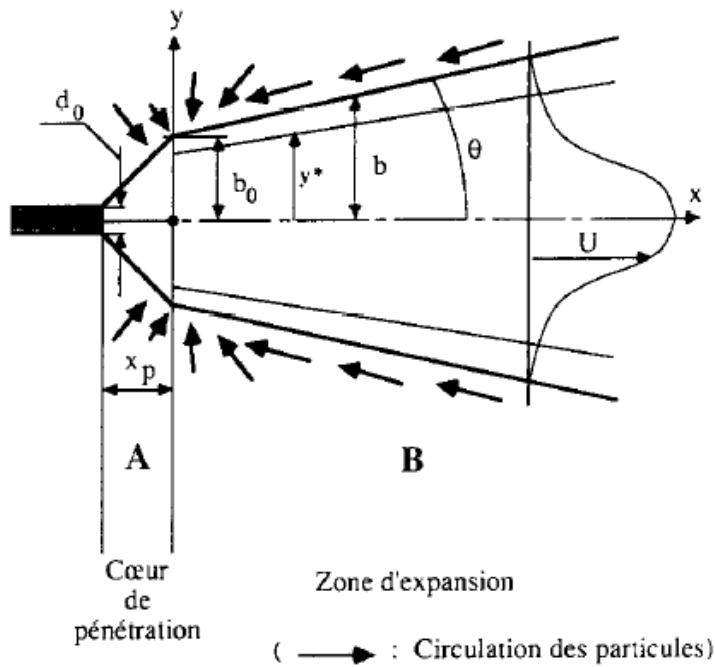
Figure 1.7: Schematic of a horizontal gas jet in a bubbling fluidized bed (Xuereb *et al.*, 1992). Particles propagate along the plume boundary in the emulsion towards the jet nozzle where they are entrained. The jet experiences an initial penetration zone following by a region of linear expansion where the average velocity profile is assumed to be Gaussian and self-similar in shape.

1.2.2 Prior Work

1.2.2.1 Modeling

The most cited work concerning jets in fluidized beds is that of Merry (1971 & 1975), who developed a semi-theoretical expression for the jet penetration length. This model is based on a simple balance of the inlet jet gas momentum with the momentum downstream in the jet plume. Merry treats the two-phase jet as if it were a homogenous jet in which the mean density and velocity vary downstream. It is assumed that the transverse mean velocity profile is self-similar, and a Schlichting bell-curve shaped profile is used. However, it should be noted that this self-similar profile was developed for a 2D wake rather than for a 2D jet (Abramovich & Schindel, 1963; Schlichting, 1979). Merry borrows from Shakhova & Minaev (1970) in assuming that the mean density increases from the gas density at the jet inlet to the mean emulsion density at the

extent of the jet plume. The model is then modified to account for particle acceleration dynamics, which assumes high particle Reynolds numbers so that the coefficient of drag is constant with a value of 0.44. Merry's resulting equation considers the effects of the jet inlet velocity and diameter and particle size and density. However, the effect of fluidization velocity is only considered indirectly via the emulsion void fraction.

Roach (1993) offers a slightly more in-depth look at the jet physics and suggests that the fluidization velocity has a first order influence on the jet penetration. This conclusion was reached by assuming simple power-law relations for the jet plume width and mean velocity with downstream distance, which are dependent on the fluidization state of the emulsion. However, the author concludes that experiments with single jets over a wide range of fluidization velocity ratios are needed to further characterize and quantify this influence.

1.2.2.2 Experimental Techniques and Results

As with modeling, the oldest and most common type of experimental work concerning jets in fluidized beds involves measuring the jet penetration in a bubbling emulsion. Thankfully, data trends concerning jet penetration reported in the literature seem to be largely consistent. Several papers report the effects of varying the different parameters (jet velocity, jet diameter, particle density, particle diameter, and fluidization velocity). Hirsan *et al.* (1980) produced a report which concluded that for a vertical jet, the penetration into a bubbling bed increases with increasing jet nozzle velocity, increases with increasing jet nozzle diameter, decreases with increasing particle density, decreases with increasing particle size, and decreases with increasing bed fluidization velocity. Though these integral scale observations are qualitatively useful, due to insufficient data at the differential scale they cannot offer much quantitative physical insight.

In order to understand the nature of mass, momentum, and energy transfer in the jet, the velocity profiles of both phases at various axial locations must be known. An overview of transverse and axial profile measurements is given by Massimilla (1985). Typically, gas velocities are obtained with Pitot tubes and high speed video is used to determine the particle velocities. Pitot tubes are intrusive and their pressure

11

measurements can only be correlated to gas velocities if the gas and solids momentum contributions can be distinguished from each other. In order to measure the relatively high particle velocities in a jet plume (~10 m/s), significant illumination is needed for cinemagraphic techniques. This is extremely difficult in bubbling beds due to the limited optical access; therefore these measurements tend to be limited to particles near the wall. Other optical techniques, such as optical fiber probes (Zhu *et al.*, 2001) and laser Doppler velocimetry (LDV) (Werther *et al.*, 1996; Breault *et al.*, 2008) have been limited to dilute, circulating fluidized beds.

The experimental data gathered with these techniques indicates that the gas and particulate phase velocity profiles appear roughly self-similar (Filla *et al.*, 1983; Ounnar *et al.*, 2009). However, integration of these profiles to determine the mass flow and momentum rates for the two phases has not been successful. Xuereb *et al.* (1991) noted that the volume flux of air that was determined by integrating the gas velocity profiles far exceeded the value recorded by the air flow meters, and that air entrainment was not enough to account for this difference. Therefore, analysis of the velocity profiles reported in the literature has been limited to simply describing the general shapes and development of the velocity profiles.

1.3 Thesis Objective and Summary

The objective of this research is to simultaneously measure gas and particulate phase velocity profiles in a vertical gas jet in a two-dimensional bubbling fluidized bed. These velocity profiles are analyzed to quantify the mass flow rate, momentum rate, and volume fraction of each phase as a function of axial distance in the jet plume. The mechanism of momentum exchange between the gas and particulate phases is also examined. These pertinent parameters will facilitate the understanding of gas jet dynamics in bubbling fluidized beds.

Chapter 2 provides an overview of laser Doppler velocimetry and discusses Bragg-cell intensity modulation, which can have adverse effects on LDV measurements of bed particle velocities. Chapter 3 describes the specific LDV technique developed to simultaneously measure the gas and particulate phase velocities. The two dimensional nature of the single phase gas jet is discussed in Chapter 4. Chapter 5 explains the two-

phase gas-particle data analysis procedure and uncertainty. The effect of fluidization velocity on jet dynamics and phase velocity scaling is examined in Chapter 6. Chapter 7 presents the conclusions and recommendations for future work.

1.4 Chapter 1 References

G. N. Abramovich & L. Schindel. <u>The Theory of Turbulent Jets</u>. The MIT Press (1963).

R.W. Breault , C.P. Guenther, L.J. Shadle. "Velocity fluctuation interpretation in the near wall region of a dense riser," Powder Tech. **182** (2), 137-145 (2008)

G. Chase.<u>http://chemical.uakron.edu/fclty/chase/Solids/SolidsNotes5%20Fluidization.pdf</u> Jan. 2010

D.C. Chitester, R.M. Kornosky, L-S Fan, J.P. Danko. "Characteristics of fluidization at high pressure," Chem. Eng. Sci. **39** (2), 253-261 (1984).

M. Filla, L. Massimilla, S. Vaccaro. "Gas Jets in Fluidized Beds and Spouts: A Comparison of Experimental Behavior and Models," Can. J. Chem. Eng. **61**, 370-376 (1983).

D. Geldart. <u>Gas Fluidization Technology</u>. John Wiley & Sons, New York. (1986)

J.R. Grace & H. Bi. "Introduction to circulating fluidized beds," in J.R. Grace, T.M. Knowlton & A.A. Avidan, <u>Circulating Fluidized Beds</u>, pp. 1-20, Chapman & Hall (1997).

I. Hirsan, C. Sishtla, T.M. Knowlton. "The effect of bed and jet parameters on vertical jet penetration length in gas fluidized beds," Institute of Gas Technology. 73rd AIChE Meeting, Chicago, Il. (1980).

L. Massimilla. "Gas Jets in Fluidized Beds," in J.F. Davidson, R. Clift, and D. Harrison, <u>Fluidization, Second Ed.</u>, pp. 133-171, Academic Press (1985).

J.M.D. Merry. "Penetration of a vertical jets into fluidized beds," AIChE. **21** (3), 507-510 (1975).

J.M.D. Merry. "Penetration of a horizontal gas jet into a fluidized bed," Trans. Instn. Chem. Engrs. **49**, 189-195 (1971).

A. Ounnar, J. Arrar, F. Bentahar. "Hydrodynamic behaviour of upflowing jet in fluidized bed: velocity profiles of sand particles," Chem. Eng. Process. **48** (2), 617-622 (2009)

P.E. Roach. "The penetration of jets into fluidized beds," Fluid Dynam. Res. **11** (5), 197-216 (1993).

M. Pell. <u>Gas Fluidization (Handbook of Powder Technology, Volume 8)</u>. Elsevier, New York. (1990)

H. Schlichting. Boundary-Layer Theory, 7th Ed. Translated by J. Kestin. McGraw-Hill (1979)

N.A. Shakhova & G.A. Minaev. "An engineering method of calculating a jet in a fluidized bed," Inzhenerno-Fizicheskii Zhurnal. **19** (6), 1002-1011 (1970).

C. Y. Wen & Y. H. Yu. "A generalized method for predicting the minimum fluidization velocity," AIChE J. **12** (3), 610-612 (1966).

J. Werther, B. Hage, C. Rudnick. "A comparison of laser Dopper and single-fibre reflection probes for the measurement of the velocity of solids in a gas-solid circulating fluidized bed," Chem. Eng. Process. **35** (5), 381-391 (1996)

C. Xuereb, C. Laguerie, T. Baron. "Etude du comportement de jets continues horizontaux ou inclines introduits dans un lit fluidise par un gaz I: Morphologie des jets," Powder Tech. **67** (1), 46-56 (1991)

C. Xuereb, C. Laguerie, T. Baron. "Etude du comportement de jets continues horizontaux ou inclines introduits dans un lit fluidise par un gaz Deuxieme partie: profiles de vitesse du gaz dans les jets horizontaux," Powder Tech. **64** (3), 271-283 (1991)

C. Xuereb, C. Laguerie, T. Baron. "Etude du comportement de jets continues horizontaux ou inclines introduits dans un lit fluidise par un gaz III: modelisation de la zone d'ecoulement developpe du jet," Powder Tech. **72** (1), 7-16 (1992)

J.-X. Zhu, G.-Z. Li, S.-Z. Qin, F.-Y. Li, H. Zhang, Y.-L. Yang . "Direct measurements of particle velocities in gas–solids suspension flow using a novel five-fiber optical probe," Powder Tech. **115** (2), 184-192 (2001)

CHAPTER 2:

LDV MEASUREMENTS IN OPTICALLY DENSE FLOWS

In this chapter, the obstacles associated with conducting LDV measurements in optically dense flows are addressed. These challenges are primarily due to laser beam intensity fluctuations caused by Bragg Cell frequency shifting and laser cavity mode hopping. These phenomena and the associated frequency mixing with Doppler burst signals have been published in Mychkovsky *et al.* (2009)

2.1 An Overview of Laser Doppler Velocimetry

Laser Doppler velocimetry is an established measurement technique and overviews of the fundamentals are provided in Durst *et al.* (1976) and Stevenson (1982). The basic operating principle is that an LDV signal is recorded when a particle scatters light as it traverses the interference fringe pattern established by intersecting monochromatic laser beams (Figure 2.1). Therefore particle velocity is directly proportional to the frequency of the scattered light.
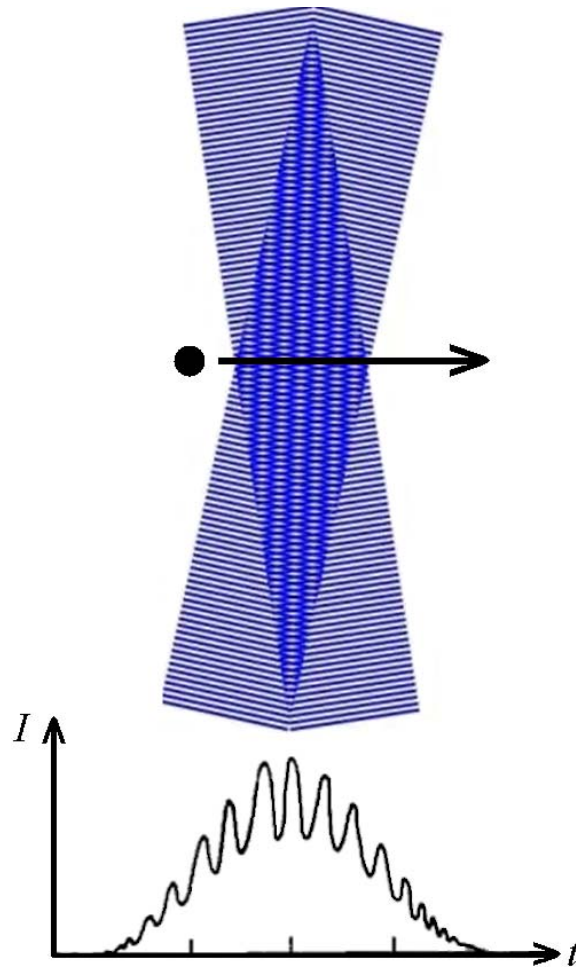
Figure 2.1: Basic principle of Laser Doppler Velocimetry. As illustrated above, a particle scatters the light of the interference fringe pattern as it traverses the intersection of two monochromatic laser beams. The frequency of this optical signal (shown below) is recorded and is directly related to the particle speed.

In order to remove the directional ambiguity of the velocity associated with a specific Doppler frequency, one of the intersecting laser beams is frequency shifted by an acousto-optic element, usually a Bragg Cell operating at 40 MHz. This slight optical frequency shift causes the fringe pattern to propagate in space at a speed of $\delta_f f_B$ within the measurement volume, where f_B is the Bragg Frequency and the fringe spacing given by

$$\delta_f = \frac{\lambda}{2\sin\left(\dfrac{\varphi}{2}\right)}$$

(2.7)

λ is the light wavelength and φ is the angle between the intersecting beams. Hence the particle velocity is related to the burst frequency of scattered light, f, by

$$v_x = \left(f - f_B\right)\delta_f$$

(2.8)

Therefore, a stationary particle would produce a Doppler signal at f_B, a particle moving in the direction of the fringe motion would produce a Doppler signal less than f_B, and a particle moving in the opposite direction of the fringe motion would produce a Doppler signal greater than f_B. Typically, the beams are oriented so that the fringe pattern moves counter to the bulk particle motion.

2.2 Bragg Cell Intensity Modulation

However, Bragg shifting can also impose temporal intensity fluctuations on the frequency shifted beam (Kaczmarek *et al.,* 2004). In practice, an intensity modulation of the shifted beam occurring at twice the Bragg frequency has been detected. When present in a LDV system, a laser intensity fluctuation at $2f_B$ can produce spurious velocity measurements. It is therefore important that the cause of the amplitude modulation be understood, and that steps are taken to minimize it.

In the present work, the classical relationships that describe the physics of light beam interactions with a Bragg Cell are revisited and it is shown how reflection through the cell can lead to detectable intensity fluctuations, followed by a discussion on the conditions necessary to mitigate these effects for the application to LDV.

2.2.1 Complete Bragg Cell Intensity Reflectance

A Bragg Cell is an acousto-optic device used to split a laser beam into a zero order unshifted beam and first order shifted beam. As illustrated in Figure 2.2, a laser beam enters the Bragg Cell at a shallow angle θ with respect to normal. Within the device, a piezo-electric transducer creates an acoustic wave in the Bragg Cell media, which is usually quartz or glass. The interaction of the laser light with the acoustic wave is governed by the photoelastic effect, or the change in medium permittivity, and thus refractive index, under the action of mechanical strain. Therefore, propagation of the acoustic wave in the crystal creates gradients in the material refractive index, and the light beam will interact with this inhomogeneous media. When θ is set to the "Bragg Angle", constructive interference of the shifted beam is achieved.
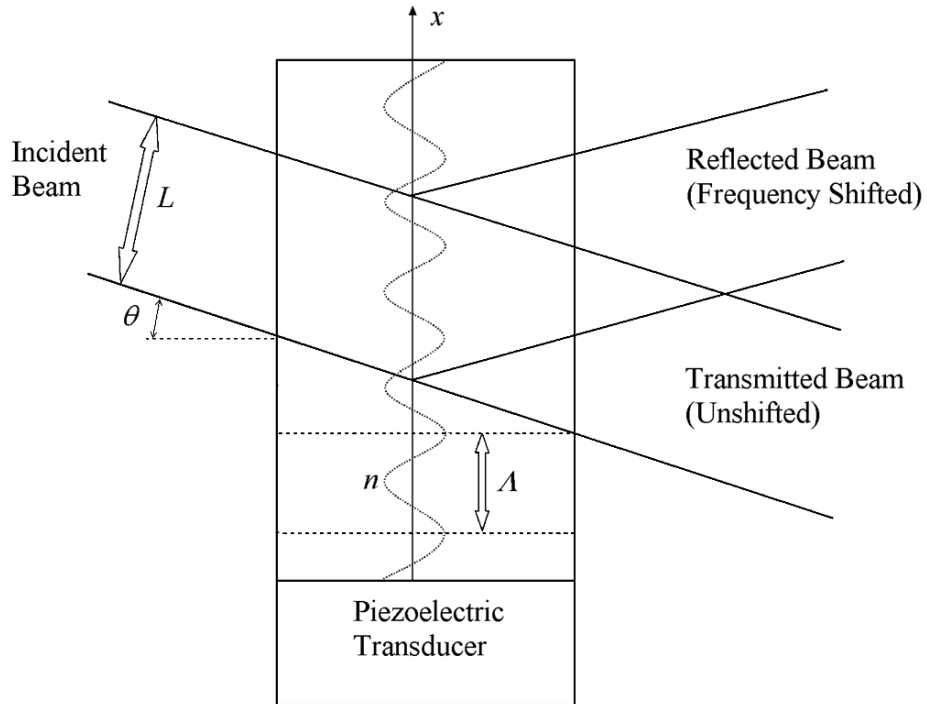
Figure 2.2: Bragg Cell schematic. An incident laser beam enters the acousto-optic element at a shallow angle θ. A portion of the beam is reflected and frequency shifted.

The propagation of light through the Bragg Cell can be described using the physical concept of light scattering, or partial reflection due to the gradients in the index of refraction (Saleh & Teich, 2007). In the present work, the laws of reflection are used to analyze the propagation of light through the Bragg Cell. In the classical derivation of

the amplitude reflectance, certain terms are neglected once the Bragg Condition is invoked. In the following derivation, these terms are retained and it is shown how they lead to the intensity modulation of the reflected beam.

The index of refraction, n, within the cell can be represented as a sinusoid

$$n(x) = n_o - \Delta n_o \cos(qx - \Omega t) \tag{2.9}$$

where n_o is the undisturbed index of refraction and Δn_o is the amplitude variation in index of refraction due to the acoustic wave within the Bragg Cell medium. The acoustic wave propagates in the positive x direction and Ω is its angular frequency. The amplitude reflectance, r_B, is the summation of all the incremental reflections within the Bragg cell across the laser beam diameter, L, and can be written as

$$r_B = \int_{-L/2}^{L/2} \exp(j2kx \sin\theta) \frac{dr}{dx} dx \tag{2.10}$$

where $q = 2\pi/\Lambda$, $k = 2\pi/\lambda$, and Λ and λ are the acoustic and optical wavelengths, respectively. The amplitude reflectance coefficient is r, which comes from the Fresnel equations. The solution to this integral expression is

$$r_B = j \frac{1}{2} \frac{dr}{dn} q\Delta n_o L \left\{ \begin{array}{l} \exp(j\Omega t)\text{sinc}\left[(2k\sin\theta - q)\frac{L}{2\pi}\right] \\ -\exp(-j\Omega t)\text{sinc}\left[(2k\sin\theta + q)\frac{L}{2\pi}\right] \end{array} \right\} \tag{2.11}$$

where the first term is called r_+ and the second r_-. Usually r_- is neglected after applying the Bragg condition $2k\sin\theta = q$ as it is small compared to r_+. However, in order to reveal the temporal fluctuations that may be present in the intensity reflectance, it is necessary to keep both terms for this analysis. The intensity reflectance is obtained by squaring the magnitude of the amplitude reflectance.

$$|r_B|^2 = \left(\frac{1}{2}\frac{dr}{dn}q\Delta n_o L\right)^2 \left\{ \begin{array}{l} \text{sinc}^2\left[(2k\sin\theta - q)\frac{L}{2\pi}\right] + \text{sinc}^2\left[(2k\sin\theta + q)\frac{L}{2\pi}\right] \\ -2\text{sinc}\left[(2k\sin\theta - q)\frac{L}{2\pi}\right]\text{sinc}\left[(2k\sin\theta + q)\frac{L}{2\pi}\right]\cos(2\Omega t) \end{array} \right\} \tag{2.12}$$

20

The first two terms in the brackets are the steady components and the third term is the time dependent component, which oscillates at twice the Bragg acoustic frequency. The first term is the primary upshifted reflection and when we invoke the Bragg condition

$$\sin \theta_B = \frac{\lambda}{2\Lambda}$$

(2.13)

this term goes to unity. The expression for dr/dn is derived from the Fresnel equations of reflection and can be written as:

$$\frac{dr}{dn} = \frac{-1}{2n_o \sin^2 \theta}$$

(2.14)

Setting θ to the Bragg angle yields

$$|r_B|^2 = \left(2\pi \frac{\Delta n_o}{n_o} \frac{L\Lambda}{\lambda^2}\right)^2 \left\{1 + \text{sinc}^2\left(\frac{2L}{\Lambda}\right) - 2\text{sinc}\left(\frac{2L}{\Lambda}\right)\cos(2\Omega t)\right\}$$

(2.15)

In order to account for laser beam attenuation due to incremental reflections as it propagates through the Bragg cell, the amplitude of $|r_B|^2$ becomes $sin^2\left(2\pi \frac{\Delta n_o}{n_o} \frac{L\Lambda}{\lambda^2}\right)$ so that its value cannot exceed unity (Saleh & Teich, 2007). The intensity reflectance can then be written as:

$$R_B = \sin^2\left(2\pi \frac{\Delta n_o}{n_o} \frac{L\Lambda}{\lambda^2}\right)\left\{1 + \text{sinc}^2\left(\frac{2L}{\Lambda}\right) - 2\text{sinc}\left(\frac{2L}{\Lambda}\right)\cos(2\Omega t)\right\}$$

(2.16)

Consider the three bracketed terms in equation (2.16). If the *sinc* and *sinc²* terms are neglected, the classical solution for reflectance under the Bragg Condition is recovered. However, under certain relevant conditions, these terms cannot be neglected.

Figure 2.3 shows that as the ratio of the beam diameter to the acoustic wavelength *(L/Λ)* increases the second bracketed term quickly drops to zero. This figure also reveals that the amplitude of the time dependent term, *|2sinc(2L/Λ)| = |2sin(2πL/Λ)/(2πL/Λ)|*, also drops but in a slower oscillatory fashion. Note that when *2L/Λ* is an integer value, the temporal component is null. However, this exact condition is very difficult if not impossible to physically achieve in practice, primarily due to uncertainty in the laser beam diameter. Since the magnitudes of the local peaks of the time dependent term decrease as *Λ/(πL)*, the temporal fluctuation in intensity reflectance can be minimized by

expanding the beam diameter. Figure 2.4 shows the amplitude ratio of the temporal fluctuating term to that of the combined steady terms.

Note that in this derivation for Bragg Cell reflectance, the beam diameter is considered to be that from a "top-hat" beam profile. The amplitude reflection expression can be convolved with a Gaussian beam profile to obtain the intensity of a reflected Gaussian beam, but the basic physical processes leading to an intensity fluctuation will remain.
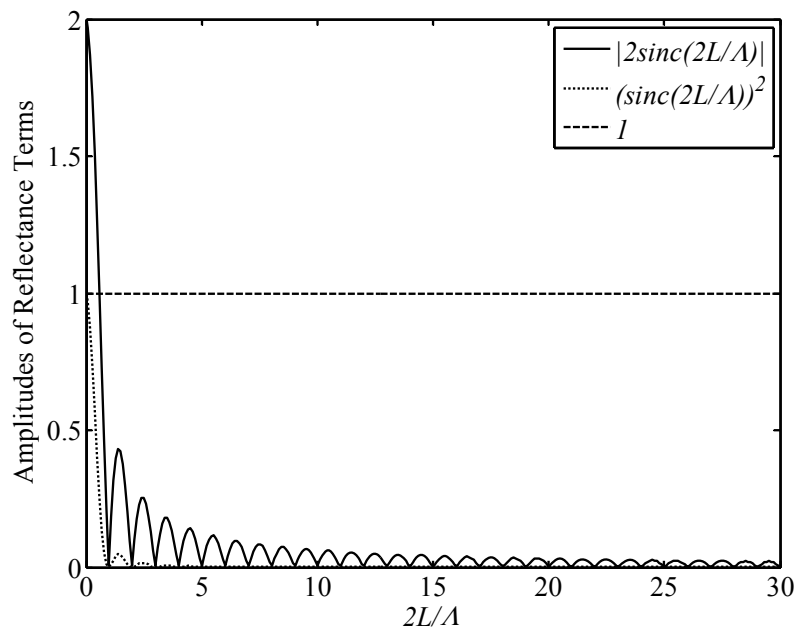
Figure 2.3: The amplitudes of the bracketed intensity reflectance terms in equation (2.16). Note the primary steady term (dashed line) is constant and the time dependent term (solid line) decreases as the ratio of laser beam diameter to Bragg Cell acoustic wavelength.
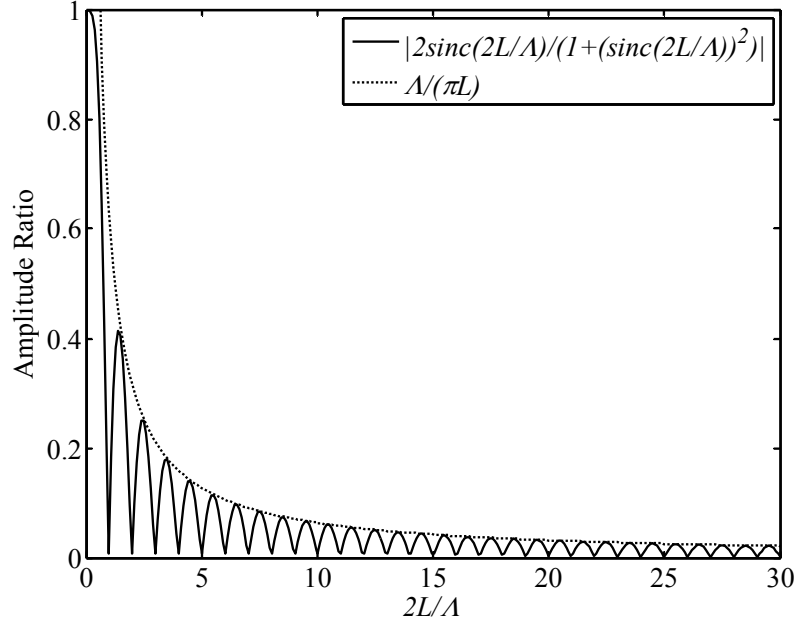
Figure 2.4: The amplitude ratio of the time varying term to the sum of the steady terms and its envelope in equation (2.16). Note that the relative amplitude of the time dependent term decreases as $\Lambda/(\pi L)$.

2.2.2 Bragg Reflectance Optimization for a Two Component LDV System

While expanding the beam diameter will reduce the temporal fluctuations of the Bragg shifted beam, it also has the adverse effect of increasing the sensitivity to the Bragg Condition. Let θ satisfy the Bragg Condition for a set optical wavelength, λ_B so the intensity reflectance at a different wavelength becomes

$$R_B(\lambda) = \sin^2\left(\frac{1}{2}\frac{dr}{dn}q\Delta n_o L\right)\left\{\begin{array}{l} \text{sinc}^2\left[\frac{1}{2}\left(\frac{\lambda_B}{\lambda}-1\right)\frac{2L}{\Lambda}\right]+\text{sinc}^2\left[\frac{1}{2}\left(\frac{\lambda_B}{\lambda}+1\right)\frac{2L}{\Lambda}\right] \\ -2\text{sinc}\left[\frac{1}{2}\left(\frac{\lambda_B}{\lambda}-1\right)\frac{2L}{\Lambda}\right]\text{sinc}\left[\frac{1}{2}\left(\frac{\lambda_B}{\lambda}+1\right)\frac{2L}{\Lambda}\right]\cos(2\Omega t) \end{array}\right\} \quad (2.17)$$

Often, the green (514.5 nm) and blue (488 nm) beams of an Argon Ion laser are used in two component LDV systems. If the angle is set to satisfy the Bragg Condition for the blue beam, Figure 2.5 shows the ratio of the steady intensity reflectance terms for the green beam to that of the Bragg optimized blue beam. The intensity reflectance for the

23

non-optimized green beam rapidly decreases as the beam diameter increases. This phenomenon can also be thought of in terms of Bragg angle tolerance as described in Saleh & Teich (2007).
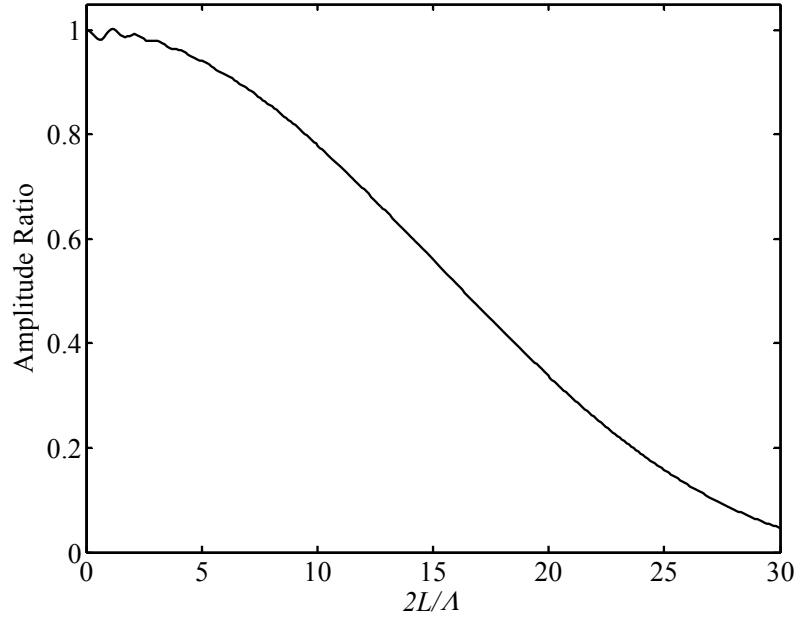
Figure 2.5: Intensity reflectance steady term ratio for a non-optimized beam (λ = 514.5 nm, λ_B = 488 nm) to that of a Bragg optimized beam ($\lambda = \lambda_B$ = 488 nm) using equation (2.17). Note the decrease in relative intensity reflectance for the non-optimized beam as the ratio of laser beam diameter to Bragg Cell acoustic wavelength increases.

Next, how the time dependent coefficients of the non-optimized beams are affected by the beam diameter is discussed. Figure 2.6 shows that the amplitude of the non-optimized beam does not diminish compared to that of the Bragg optimized beam, though they become out of phase as *2L/Λ* increases. Therefore, temporal intensity fluctuations may be noticeable on only one of the Bragg shifted beams.
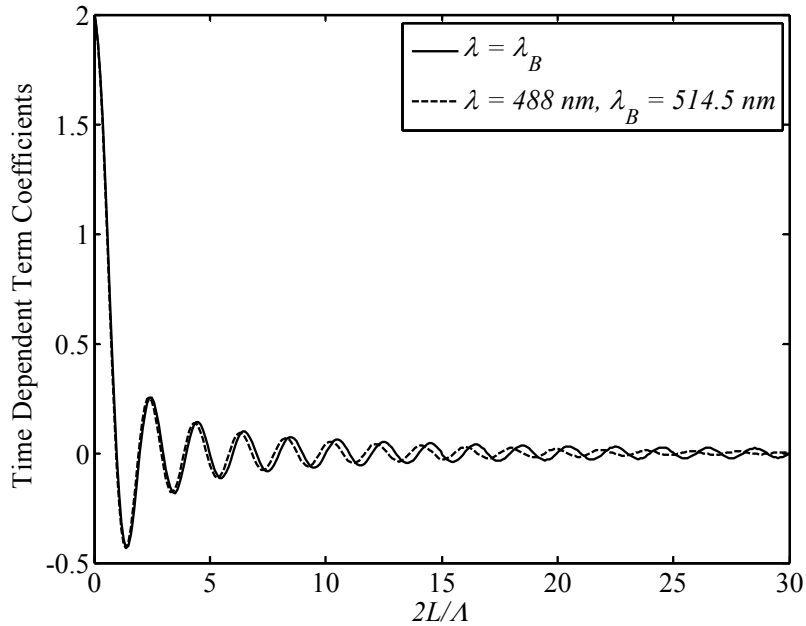
Figure 2.6: Intensity reflectance time dependent term coefficients for a non-optimized beam (λ = 514.5 nm, λ_B = 488 nm) and a Bragg optimized beam ($\lambda = \lambda_B$ = 488 nm) using equation (2.17). Note that the amplitude of non-optimized beam does not diminish compared to that of the Bragg optimized beam, though they become out of phase as the ratio of laser beam diameter to Bragg Cell acoustic wavelength increases.

In the previous section, it was shown that increasing *2L/Λ* will decrease the relative temporal intensity fluctuations for a Bragg optimized beam. Considering the additional effects when the Bragg condition is not exactly satisfied for a given optical wavelength, increasing *2L/Λ* may actually increase the temporal fluctuations for the non-optimized beam, depending on the value of λ_B/λ.

Figure 2.7 shows the relative temporal fluctuations with respect to the steady reflectance as a function of *2L/Λ* for various values of λ_B/λ. The solid black line represents the Bragg optimized condition for the two Argon Ion beams.
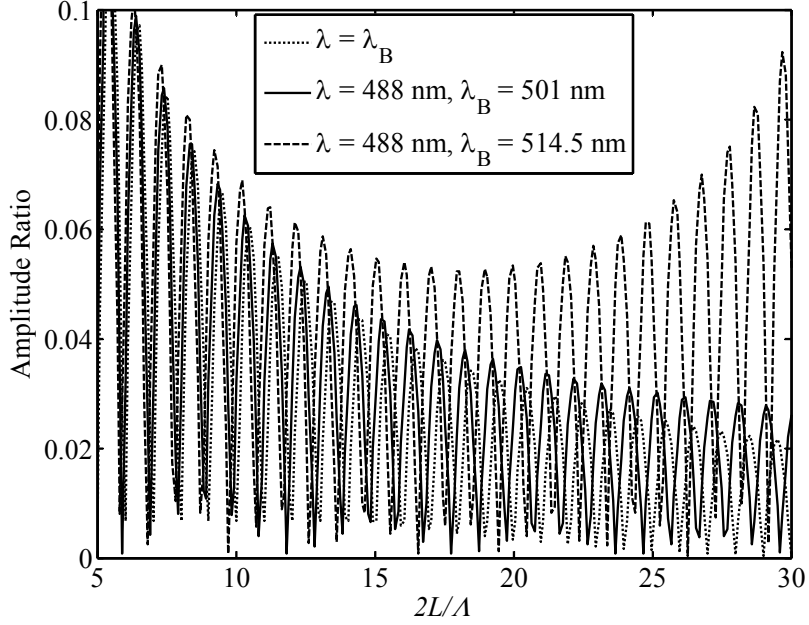
Figure 2.7: Amplitude ratios of the time varying term to the sum of the steady terms for a non-optimized beam ($\lambda = 488$ nm, $\lambda_B = 514.5$ nm), a Bragg optimized beam ($\lambda = \lambda_B = 514.5$nm), and a system optimized beam ($\lambda = 488$ nm, $\lambda_B = 501$ nm) using equation (2.17). Note that both the Bragg optimized beam and system optimized beam decrease as the ratio of laser beam diameter to Bragg Cell acoustic wavelength increases while non-optimized beam experiences a local minimum.

Using the identity *sinc(x) = sin(πx)/(πx)*, the envelope of time dependent to steady term amplitude ratio is determined to be

$$\frac{2\left(\dfrac{\dfrac{\lambda_B}{\lambda}-1}{\dfrac{\lambda_B}{\lambda}+1}\right)\sin\left[\dfrac{1}{2}\left(\dfrac{\lambda_B}{\lambda}-1\right)\pi\dfrac{2L}{\Lambda}\right]}{\sin^2\left[\dfrac{1}{2}\left(\dfrac{\lambda_B}{\lambda}-1\right)\pi\dfrac{2L}{\Lambda}\right]+\left(\dfrac{\dfrac{\lambda_B}{\lambda}-1}{\dfrac{\lambda_B}{\lambda}+1}\right)^2}$$

and is plotted in Figure 2.8. As $\lambda_B \sim \lambda$, this expression reduces to $\Lambda/(\pi L)$.

26
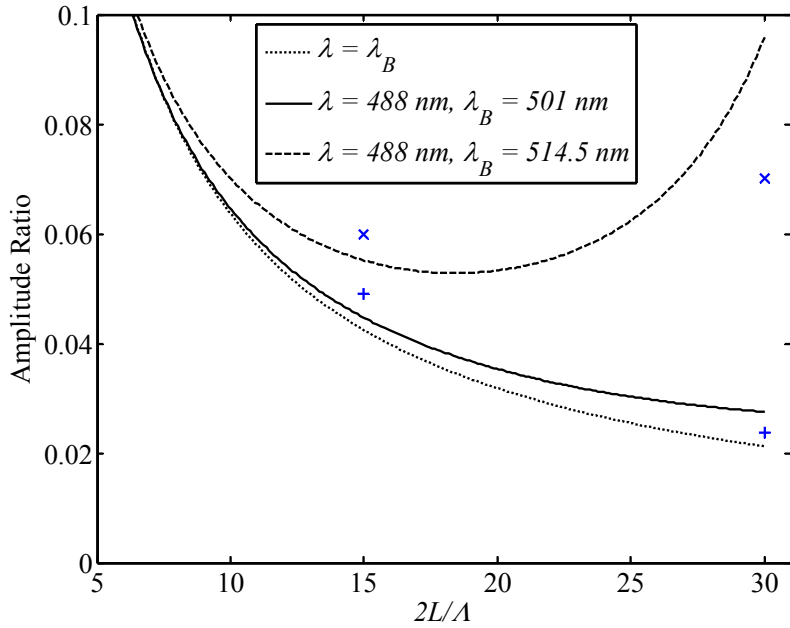
Figure 2.8: Envelopes of the time dependent to steady term amplitude ratios shown in Figure 2.7. Note that both the Bragg optimized beam ($\lambda = \lambda_B = 488$ nm) and system optimized beam ($\lambda = 514.5$ nm, $\lambda_B = 501$nm) decrease as the ratio of laser beam diameter to Bragg Cell acoustic wavelength increases while non-optimized beam ($\lambda = 488$ nm, $\lambda_B = 514.5$ nm) experiences a local minimum. Experimental results for the Bragg optimized and non-Bragg optimized wavelength conditions are plotted as + and x, respectively and are discussed in the following section.

Since the *sinc* function is evenly symmetric, *sinc(x) = sinc(-x)*, then in theory the Bragg angle can be system optimized to have equal intensity reflectance efficiencies for both optical wavelengths. Thus, if we want the primary steady reflectance terms to be equivalent for two colors λ_1 and λ_2, we set

$$\frac{\lambda_B}{\lambda} - 1 = -\frac{\lambda_B}{\lambda} + 1 \tag{2.18}$$

and the resulting system optimized Bragg angle is

$$\sin \theta_B = \left[\Lambda \left(\frac{1}{\lambda_1} + \frac{1}{\lambda_2} \right) \right]^{-1} \tag{2.19}$$

Using the Argon Ion laser parameters where $\lambda_1 = 488$ nm and $\lambda_2 = 514.5$ nm, Figure 2.9 shows that the ratios of the intensity reflectance steady terms with respect to $\lambda_B = 501$ nm are similar. Since the intensity reflectance efficiencies are the same for each color with respect to the Bragg angle, simply increasing the Bragg power, Δn_o, will increase the reflectance for both beams equally.

27
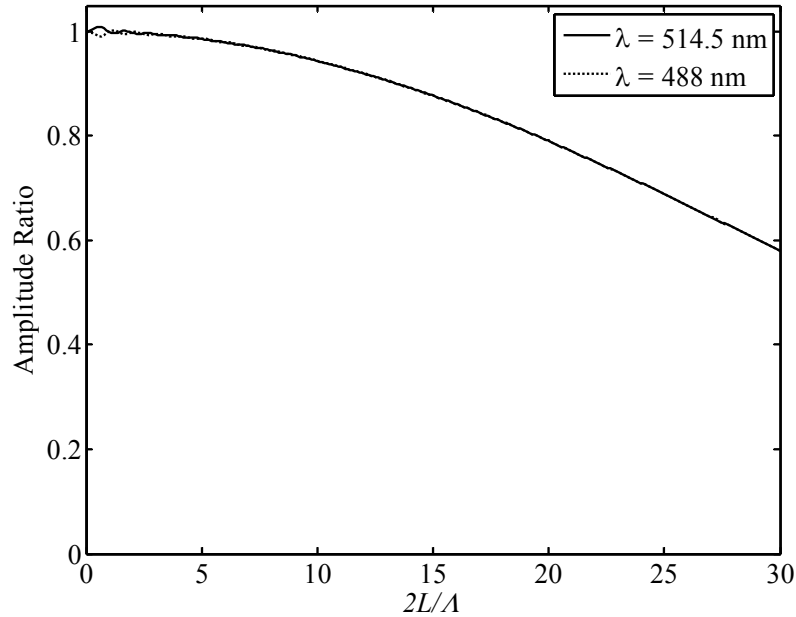
Figure 2.9: Intensity reflectance steady term ratio for two system optimized beams $\lambda = 514.5$ nm, $\lambda_B = 501$ nm and $\lambda = 488$ nm, $\lambda_B = 501$ nm using equation (2.17). Note the relative intensity reflectance for both beams are identical and much stronger than that for the non-optimized beam in Figure 2.5 as the ratio of laser beam diameter to Bragg Cell acoustic wavelength increases.

2.2.3 Application to LDV measurements

The trends described in the prior two sections have been observed in practice. Our experimental setup consisted of a TSI LDV system coupled with a Melles Griot 543-A-A03 Argon Ion laser. The Bragg angle was optimized for the blue 488 nm laser beam. The system had the following parameters:

Nominal laser beam diameter: $L = 0.68$ mm +/- 5%

Bragg frequency: $f_B = 40$ MHz

Bragg acoustic velocity: $C_B = 3,630$ m/s

Bragg acoustic wavelength: $\Lambda = 91$ microns

$2L/\Lambda \sim 15$

For the single beam measurements, a microscope objective lens was placed in the measurement volume, which partially reflected the beam intensity to a photomultiplier tube (PMT) detector in the LDV transceiver assembly. Since the envelopes shown in

28

Figure 2.8 represent maximum values of the relative temporal intensity fluctuations, Bragg shifted beam intensity measurements were recorded with a Tektronix TDS 430A oscilloscope which was triggered by an amplitude threshold after a 20 MHz high pass filter. Single sided, 10,000 point FFTs with sampling period of 2 nanoseconds were then performed on the raw signals. A 2x beam expander was then placed in front of the Bragg Cell, doubling the laser beam diameter so that $2L/\Lambda \sim 30$ for the second test condition.

Typical temporal intensity spectra for the Bragg shifted beams are shown in Figure 2.10 and Figure 2.11. These spectra are normalized with respect to the DC PMT offset. Thus, the peaks at 80 MHz (twice the Bragg frequency), can be compared to the theory derived in the prior section and are plotted as points in Figure 2.8. Figure 2.10 shows that the amplitude ratio decreases from approximately 5% to 2.5% and Figure 2.11 shows that the amplitude ratio slightly increases from about 6% to 7% for the non-Bragg angle optimized green beam. The error in these measurements is within +/- 5% of the normalized peak value. The results for these two conditions are in good agreement with the theoretical trends shown in Figure 2.8. The temporal intensity spectra also reveal that there are no higher order Bragg harmonics at 120 MHz or 160 MHz. When this experiment was performed with the unshifted beams, no noticeable 80 MHz peak was observed for either color beam.
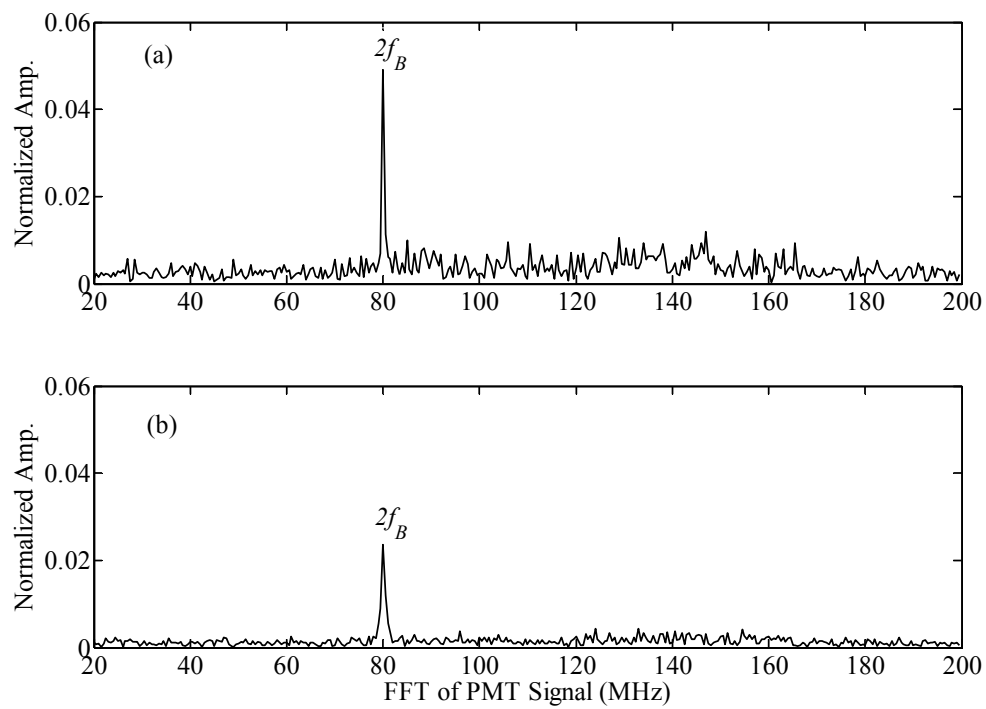
Figure 2.10: Temporal intensity spectra of the Bragg shifted 488 nm beam with *2L/Λ* ~ 15 (a) and *2L/Λ* ~ 30 (b). The Bragg angle was optimized for 488 nm. Beam expansion reduces the intensity fluctuations for the optimized beam.
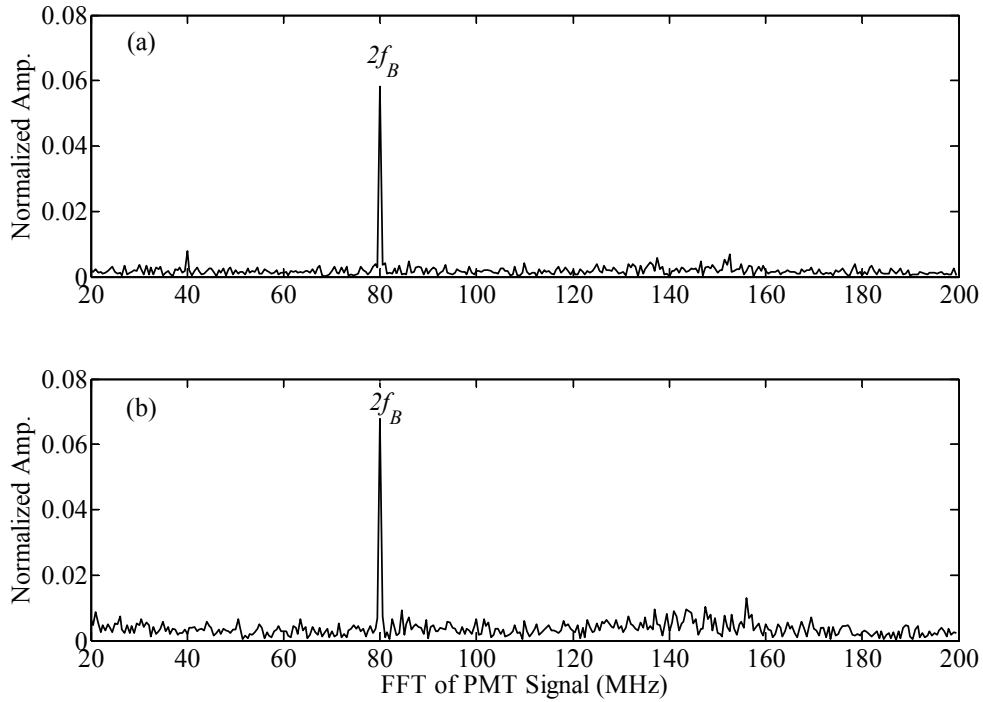
Figure 2.11: Temporal intensity spectra of the Bragg shifted 514.5 nm beam with *2L/Λ* ~ 15 (a) and *2L/Λ* ~ 30 (b). The Bragg angle was optimized for 488 nm. Beam expansion slightly increases the intensity fluctuations for the non-optimized beam.

For the LDV measurements, a spinning sanding disk was placed in the measurement volume and experiments were run once again with both the nominal and 2x expanded laser beam diameters. Though it is difficult to quantitively predict the impact that the intensity fluctuations of the Bragg shifted beam has on the LDV signal, Figure 2.12a shows that the magnitude these optical signals are approximately equivalent for the Bragg optimized color with the nominal laser beam diameter. This false LDV peak will be problematic for high speed flows. For example, a typical LDV system may have a fringe spacing of approximately 3.5 μm, so that the 80 MHz signal corresponds to a 140 m/s velocity. When the beam is expanded, the LDV signal becomes stronger than the 80 MHz peak. Though the LDV burst is not always stronger than the Bragg intensity fluctuation peak, the expanded beam setup makes it plausible to filter out the 80 MHz false peaks by means of an intensity threshold, though the LDV data rate would be correspondingly lower. Also note that the 80 MHz signal is not shifted by the particles moving through the measurement volume.

31

As would be expected, the LDV to 80 MHz peak becomes slightly worse for the non-Bragg angle optimized green beam measurements. As mentioned in Lascos & Cassidy (2009), optical intensity modulation can cause frequency mixing. This intensity fluctuation will mix with the Doppler burst signal according to trigonometric relationship expressed in equation (2.20).

$$\cos(2\pi 2 f_B t)\cos(2\pi f t) = \frac{1}{2}\cos\left[2\pi(2 f_B + f)t\right] + \frac{1}{2}\cos\left[2\pi(2 f_B - f)t\right] \quad (2.20)$$

Both the downmixed (occurring at $2f_B - f$) and upmixed ($2f_B + f$) peaks are evident in Figure 2.13. Since frequency downmixing is symmetric with respect to the LDV peak about 40 MHz, which corresponds to zero velocity, it can be a problem when both positive and negative velocities are to be measured, such as the case with transverse turbulent fluctuations. Because this frequency mixing is an optical phenomenon, electronically filtering out the 80 MHz signal will not eliminate this problem.

In practice, it can be difficult to system optimize the Bragg angle so that both color-shifted beams reduce intensity fluctuations upon laser beam expansion. Thus, it is recommended that the system be optimized for one of the LDV colors, and that this color be used to measure transverse velocities since frequency mixing will be minimized. The non-optimized color should then be used to measure the streamwise direction. However, both the intensity fluctuations occurring at twice the Bragg frequency, as well as the frequency-mixed optical signals, will appear as velocity measurements. Therefore, these signals can only be non-arbitrarily filtered out if they correspond to unphysical velocities for a particular flow situation.
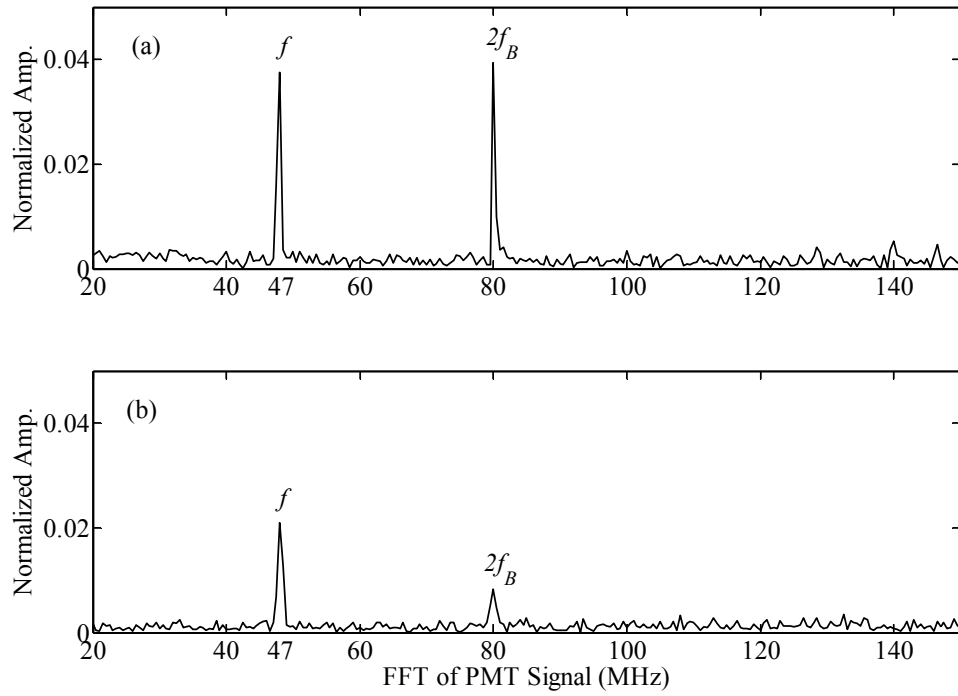
Figure 2.12: Temporal intensity spectra of the 488 nm LDV signal beam with *2L/Λ* ~ 15 (a) and   *2L/Λ* ~ 30 (b). The Bragg angle was optimized for 488 nm. The amplitude of the Bragg Cell induced intensity fluctuation is comparable to the LDV burst signal, and is reduced by laser beam expansion. No frequency mixing peaks are detected.
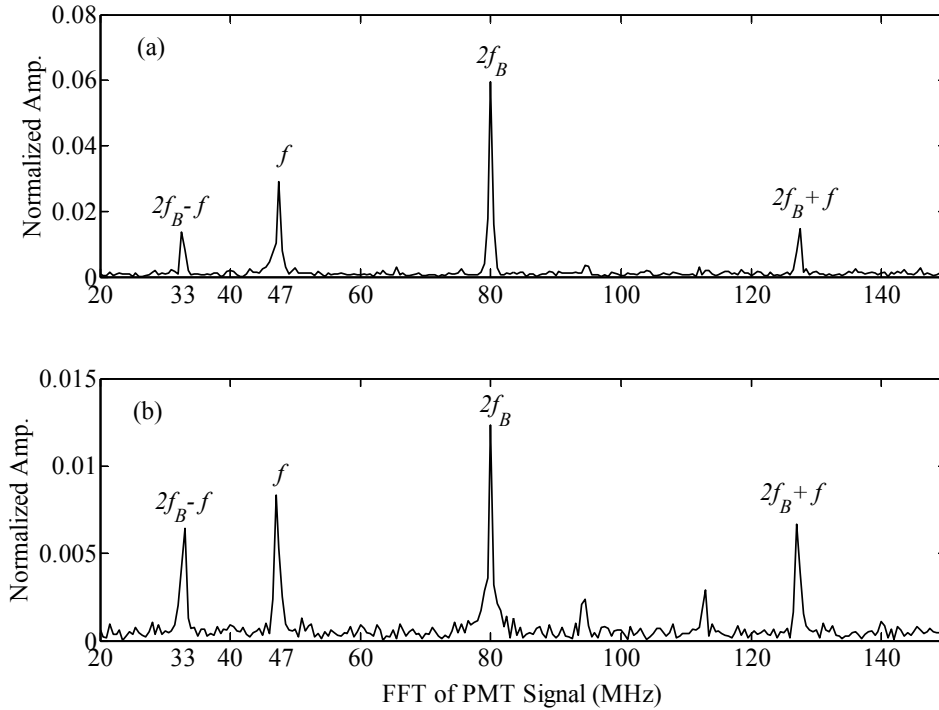
Figure 2.13: Temporal intensity spectra of the 514.5 nm LDV signal with $2L/\Lambda \sim 15$ (a) and $2L/\Lambda \sim 30$ (b). The Bragg angle was optimized for 488 nm. The amplitude of the Bragg shifted beam intensity fluctuation is greater than the LDV burst signal, and is slightly increased by laser beam expansion. Upmixed and downmixed frequency peaks are present.

2.3 Laser Mode Hopping Intensity Modulation

In addition to the Bragg Cell intensity modulation, all beams emerging from ionized gas lasers will experience intensity fluctuations due to mode hopping, which is associated with transitions in the laser resonance and occurs at a frequency of $C/2L_c$, where C is the speed of light and L_c is the cavity length. For a 1.2 m laser, the mode hopping frequency will occur at 125 MHz. When mixed with the Bragg cell intensity fluctuation, this produces a peak at 45 MHz, as shown in Figure 2.14. Note that for this figure the Doppler burst frequency for this setup occurs at 36 MHz and thus a Bragg-Doppler mixed signal occurs at 44 MHz, which is very near the $C/2L_c$-$2f_B$ mixed peak. Also note that the laser used to obtain the data in Figure 2.13 was smaller with a cavity length of approximately 300 cm, and therefore had a mode hopping frequency around 500 MHz.
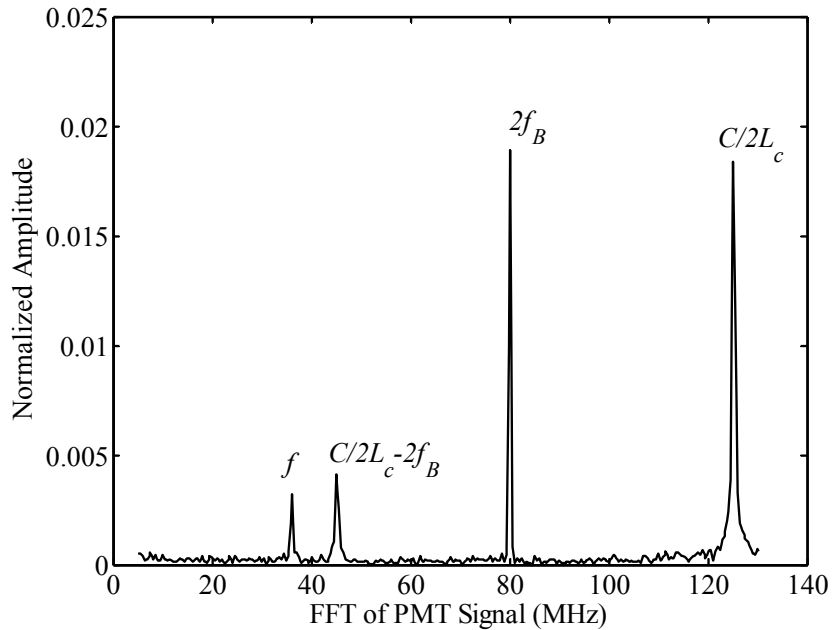
Figure 2.14: Frequency mixing of the laser mode hopping intensity fluctuation with the Bragg shifted beam intensity fluctuation. The amplitude of the frequency downmixed peak is comparable to the LDV burst signal.

2.4 LDV Configuration

The intensity fluctuation frequency mixing described in this chapter is an optical phenomenon and is only noticeable when a significant portion of the Bragg shifted beam is reflected and detected by the LDV photomultiplier, which is the case with measurements of large particles, measurements in optically dense regions, or measurements near reflecting boundaries.

In order to eliminate these spurious optical signals, the 80 MHz intensity fluctuation due to the Bragg cell was minimized by optimizing the laser beam diameter entering the Bragg cell (*via* the laser aperature) as well as the Bragg angle as described in the conclusion of subsection 2.2.3. The smaller 300 cm argon-ion laser was not powerful enough for the fluidized bed experiments, therefore the larger 1.2 m laser was necessary. The residual peak at 45 MHz was avoided by orienting the axial velocity measurement beams (non-Bragg optimized) so that the fringes move in the direction of the jet flow and the band pass filter was set to 5-50 MHz. Any false bursts detected at 45 MHz where subsequently omitted when determining velocity values. No frequency down-mixing was used in the post-processing of either channel to avoid further complications.

2.5 Chapter 2 References

F. Durst, A. Melling, J.H. Whitelaw. Principles and Practice of Laser-Doppler
  Anemometry. Academic Press (1976)

P R Kaczmarek, T Rogowski, A J Antonczak, K M Abramski, "Laser Doppler
  vibrometry with acoustooptic frequency shift," Opt. Appl. 34, 373-384 (2004)

S.J. Lascos & D.T. Cassidy, "Optical phase and intensity modulation from a rotating
  optical flat: effect on noise in degree of polarization measurements," Appl. Opt.
  48 (9), 1697-1704 (2009)

A.G. Mychkovsky, N.A. Chang, S.L. Ceccio, "Bragg cell laser intensity modulation:
  effect on laser Doppler velocimetry measurements," Appl. Opt. 48 (18), 3468-
  3474 (2009)

B.E.A. Saleh & M.C. Teich, "Acousto-Optics," in Fundamentals of Photonics, 2nd Ed,
  pp. 804-833, Wiley (2007)

W.H. Stevenson. "Laser Doppler Velocimetry: A Status Report," IEEE 70 (6), 652-658
  (1982)

CHAPTER 3:

LDV TECHNIQUE TO SIMULTANEOUSLY MEASURE GAS AND PARTICULATE PHASE VELOCITIES

In the previous chapter, challenges regarding Doppler velocimetry measurements in particle laden flows were examined. This knowledge was used to determine an optimal LDV configuration. The current chapter describes the 2D fluidized bed apparatus, the technique used to seed the jet gas with ice crystals, and Doppler burst intensity and coincidence subranging procedure used to differentiate the simultaneous gas and particulate phase velocity measurements. Example gas and particulate phase velocity profiles are presented.

3.1 Experimental Setup

3.1.1 Fluidized Bed

Experiments were conducted in a two-dimensional (2D) bubbling fluidized bed, which was shown in Figure 1.6. The bed dimensions are 457 mm wide by 1 m tall with a 12.7 mm gap. The walls are transparent acrylic with 102 mm by 153 mm by 5 mm thick quartz viewing windows inserted 50 mm above the vertical jet inlet orifice, which is 9.2 mm in diameter. The vertical jet is located midway across the porous polyethylene fluidization distributor.

The particles used in the emulsion are 838 μm Sauter mean diameter high-density polyethylene (HDPE) micropellets, which have a density of 900 kg/m^3. The minimum fluidization velocity for these particles was experimentally determined to be 29 cm/s. The velocity profiles presented in this chapter are obtained with a jet inlet velocity of 92 m/s and a distributor fluidization velocity of 34 cm/s.

3.1.2 LDV Parameters

Bed particle and gas phase velocities were obtained with a two-component LDV system employing an argon-ion laser. The axial velocities were recorded on Channel 1 using the green beam (514.5 nm) and the transverse velocities were recorded on Channel 2 using the blue (488 nm) beam. The LDV parameters and settings are listed in Table 3.1. A detailed justification for this LDV configuration is provided in Chapter 2.

In order to simultaneously measure the gas and particulate phase velocities, high power laser beams are needed to form the LDV measurement volume. It should be noted that increasing the beam power can sacrifice the beam quality for an ionized gas laser (Johston *et al*., 1992). Therefore a compromise must be reached in order to efficiently launch the laser beams into single mode optical fibers, which is necessary in many scanning LDV systems.

	Ch 1	Ch 2
Laser Power per Beam (mW)	90	55
Beam Diameter (microns)	90	85
PMT Gain (mV)	450	450
Burst Threshold (mV)	250	150
Frequency Downmixing (MHz)	0	0
Band Pass Filter (MHz)	5-50	20-65
Bragg Shift Frequency (MHz)	40	40
Fringe Spacing (microns)	3.74	3.55
Velocity Range (m/s)	131 to -37	71 to -89
Coincidence Interval (μs)	10	10

Table 3.1: LDV parameters. The system was optimized for maximum laser beam power and minimal laser beam intensity fluctuation complications. The large dynamic velocity range enables simultaneous gas and particulate phase velocity measurements.

3.1.3 Jet Gas Seeding

The jet gas was seeded with ice crystals, which were formed by rapidly condensing and freezing (T_j = -5$^{\rm o}$C) the moisture in the jet air just prior to injection *via* a dry ice heat exchanger. The heat exchanger consisted of a pressure vessel that was submerged in a tub of dry ice, so that no mass transfer from the CO_2 sublimation

contaminated the jet gas. Subzero inlet temperatures were easily achieved; however the temperature would rise to 0^oC as a thick insulating layer of frost and snow formed on the inner surface of the cooling vessel, which would cause the seeding rate to drop. Various internal flow configurations were implemented before it was discovered that simply attaching a limp hose to the inlet port, which was free to whip about the vessel, prevented the ice crystals from depositing on the inner surface and maintained a consistent seeding rate. In addition, all piping with internal threads was replaced with compression fit tubes to eliminate regions of ice accumulation. External heat guns were used to prevent the formation of frost on the quartz windows.

These ice crystals are on the order of a few microns in size (Sasaki *et al.*, 1980) and therefore reflect much less laser light than the larger bed particles, which are several hundred microns in diameter. Furthermore, due to the small size and low density of the ice crystals, they track the jet gas velocity well, which in the axial direction is significantly higher than the bed particle velocities. Therefore, the gas tracer ice crystals will have low intensity, high axial velocity bursts whereas the larger bed particles will have high intensity, low axial velocity bursts as shown in Figure 3.1.

As a safety precaution, it should be noted that rapid condensation of moisture in air is accompanied by separation of electric charges which can produce large voltage discharges, similar to lightning in atmospheric thunderstorms, if the apparatus is not properly grounded (Grosu *et al.*, 2007)
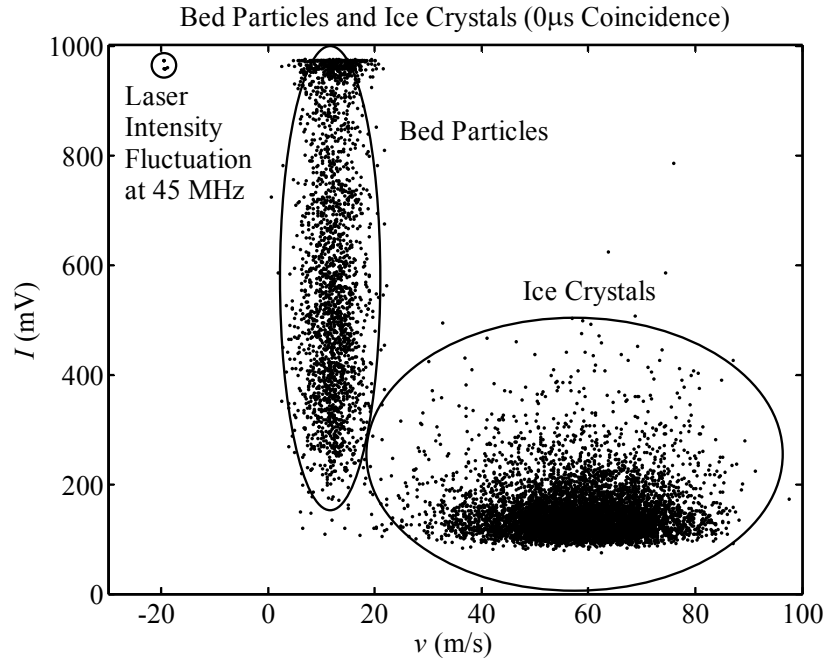
Figure 3.1: Doppler burst intensities and velocities for bed particles and jet gas tracer ice crystals measured in the plume. The small (~1 μm) ice crystals have low intensity, high velocity bursts whereas the larger bed particles (838 μm) have high intensity, low velocity bursts.

3.2 LDV Bursts

Intensity subranging has been done by Lee & Durst (1982) in ducts and by Barlow & Morrison (1990) in open air, particle-laden jets. Large particles span several fringes and reflect a larger fraction of the laser beam light when passing through the LDV measurement volume and therefore have larger burst pedestals than tracer particles whose size is on the order of the fringe spacing (Figure 3.2).

When the burst pedestal is removed with a high pass filter, it is evident that the smaller tracer particles have much cleaner Doppler signals (Figure 3.3). This is because particles that are much larger than the fringe spacing require surface inclusions, which are often erratic, to scatter light. If the entire surface continuously produced a Doppler signal then the burst gate time would be on the order of the particle residence time in the measurement volume, which is approximately d_p/v since $d_p >> D_m$. However, Figure 3.4 shows that this is not the case and that particle burst gate time tends to be limited by the size of the LDV measurement volume, which is indicative of Doppler bursts caused by small surface inclusions.

40

Furthermore, since burst gate time does not necessarily correspond to the residence time, gate time weighting is not an appropriate way to correct for any LDV velocity bias effects that may occur. Therefore, the velocity values reported for both phases are simply based on the arithmetic average of the bursts recorded at a given location. This simple data analysis method has been found to have an insignificant bias effect on LDV measurements (Ahmed *et al.*, 1996).
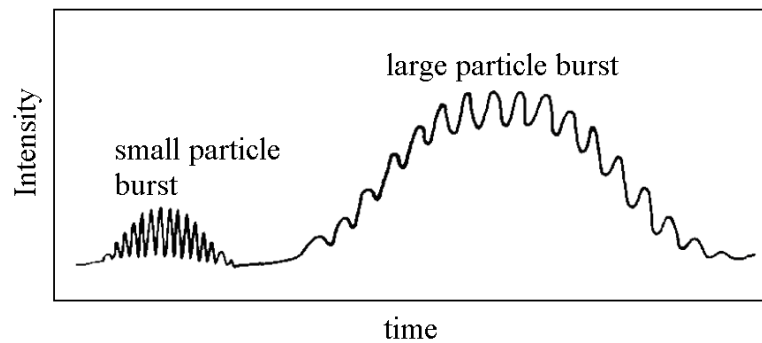
Figure 3.2: LDV burst signals from small and large particles. Modified from Lee & Durst (1982). The high frequency component is the Doppler frequency, which corresponds to the fringe spacing. The low frequency offset is the burst pedestal, which corresponds to the measurement volume dimensions. Small particles (diameter on the order of the LDV fringe spacing) produce lower intensity signals with a strong Doppler component whereas large particles (diameter much greater than the LDV fringe spacing) produce signals with high intensity burst pedestals.
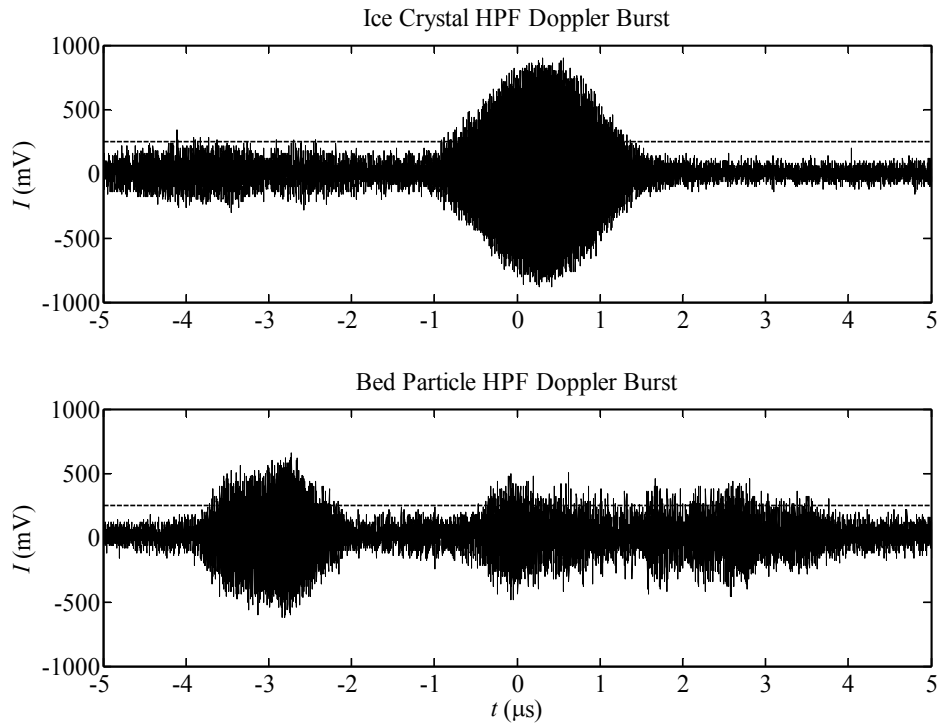
Figure 3.3: Doppler bursts from ice crystals and bed particles with the pedestal removed then amplified. The dashed line indicates the value of the burst threshold. The smaller ice crystals produce cleaner Doppler bursts since the entire surface is used to scatter the fringe light pattern. The larger bed particles produce erratic Doppler bursts since they rely on surface inclusion to scatter the fringe light.
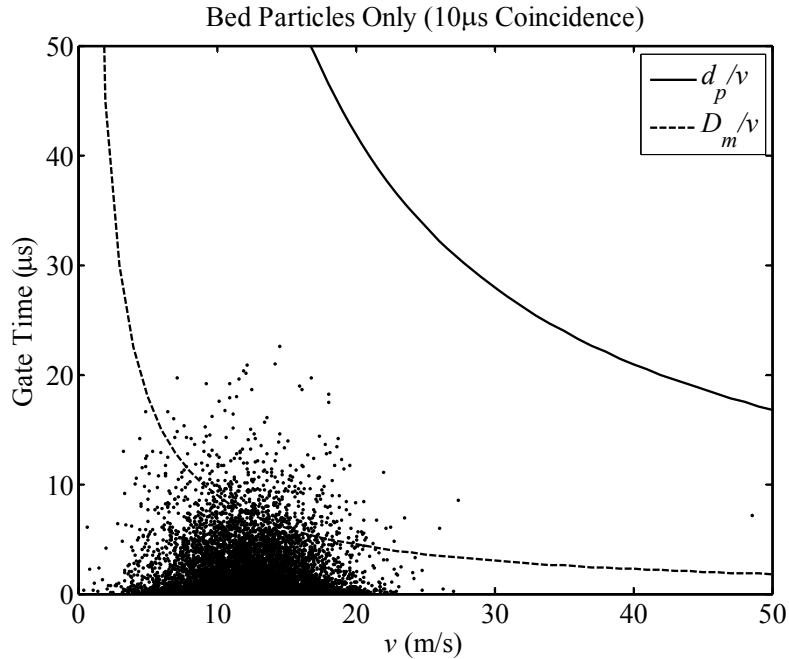
Figure 3.4: Doppler burst gate times for bed particles measured in a jet plume. If the bed particle surface scattered the LDV finge pattern light continuously, then the burst gate time would be related to the large particle diameter. However, the bursts are due to smaller surface inclusions, and therefore the burst time tends to be limited by the smaller measurement volume diameter.

Because large particle bursts are not clean as small tracer bursts, temporal coincidence between the two directional component channels is more difficult to achieve. For example, an elongated fissure may only cause a Doppler burst with one set of fringes depending on its orientation. In this particular experimental setup, bed particles can move with velocities up to about 10 m/s. The measurement volume diameter is approximately 100 μm, therefore a coincidence interval of 10 μs is used for the subranged particle bursts. Strict coincidence criteria (0 μs), which requires that both channels detect a valid Doppler burst simultaneously, is maintained for the gas tracer ice crystals bursts. Note that the 'Burst Threshold' settings listed in Table 3.1 are applied to the high pass filtered Doppler bursts and that the 'Burst Intensity' values (referenced in the graphs) are recorded prior to the pedestal removal.

In order to determine the intensity threshold values for the bed particles and gas tracer ice crystals, the bubbling bed was: 1) run with a room temperature jet so that no ice crystals were present, and then 2) run with a cold, seeded jet in an empty bed so that no bed particles were present. An intensity histogram of the bed particle only run is shown in Figure 3.5. The corresponding probability distribution (Figure 3.6) indicates that over

99% of the bed particle bursts have intensities greater than 200mV. An intensity histogram of the gas tracer ice crystal only run is shown in Figure 3.7. The corresponding probability distribution (Figure 3.8) indicates that over 99% of the ice crystal bursts have intensities less than 500mV. Therefore, in order to eliminate cross-contamination of the data, the LDV bursts are subranged according to the following criteria:

Bed particles: I > 500 mV, 10 μs coincidence
Gas tracer ice crystals: I < 200 mV, 0 μs coincidence
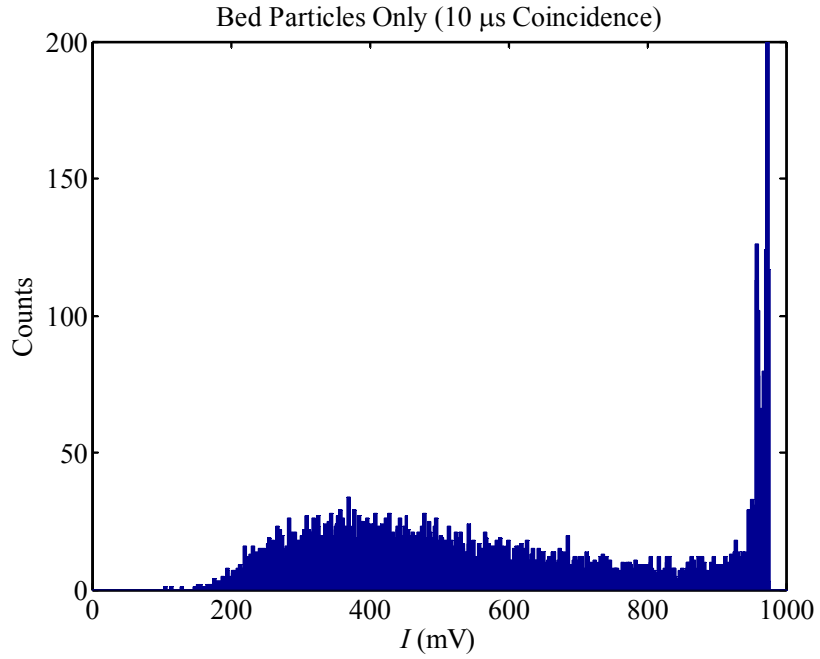
Figure 3.5: Histogram of bed particle Doppler burst intensity.
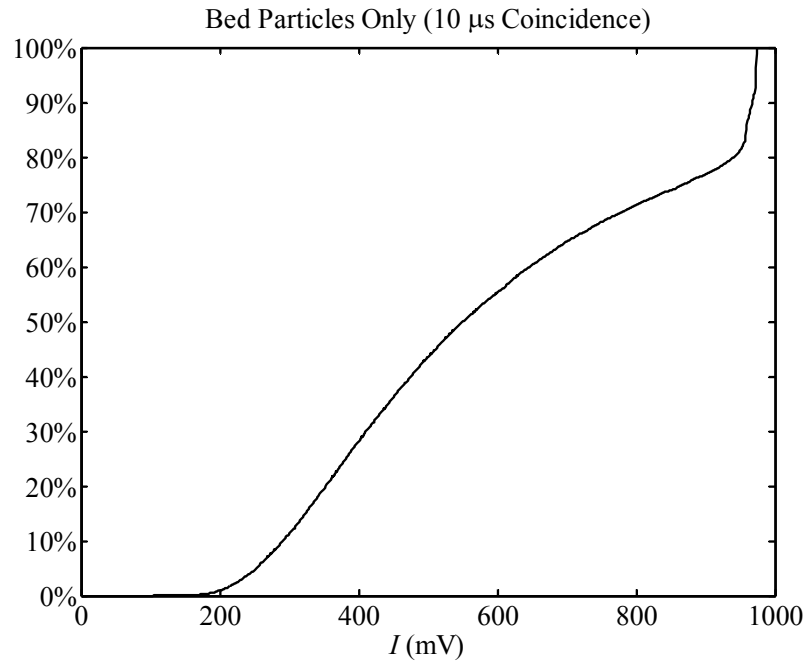
Figure 3.6: Probability distribution of bed particle Doppler burst intensity. 99% of the bed particle bursts have intensities greater than 200 mV.
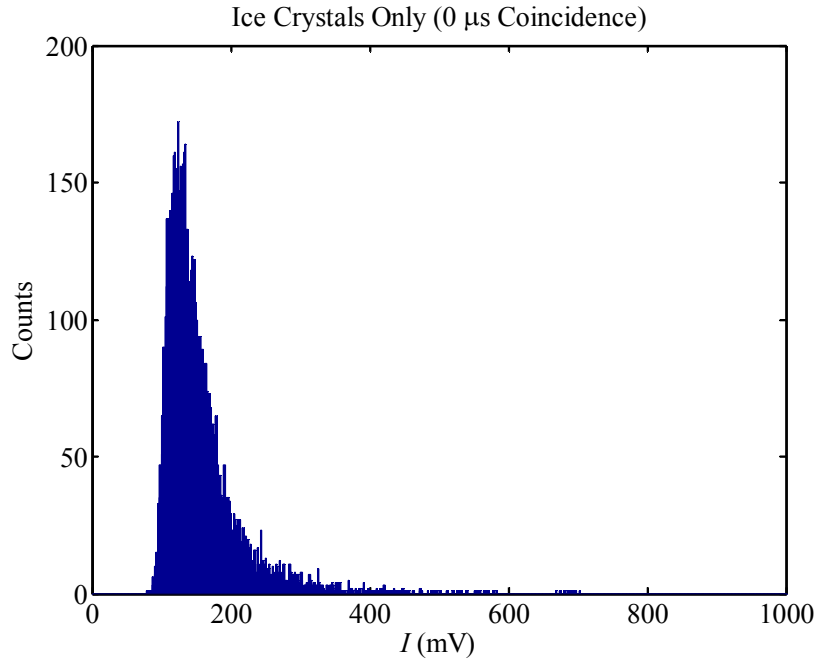
Figure 3.7: Histogram of ice crystal Doppler burst intensity.
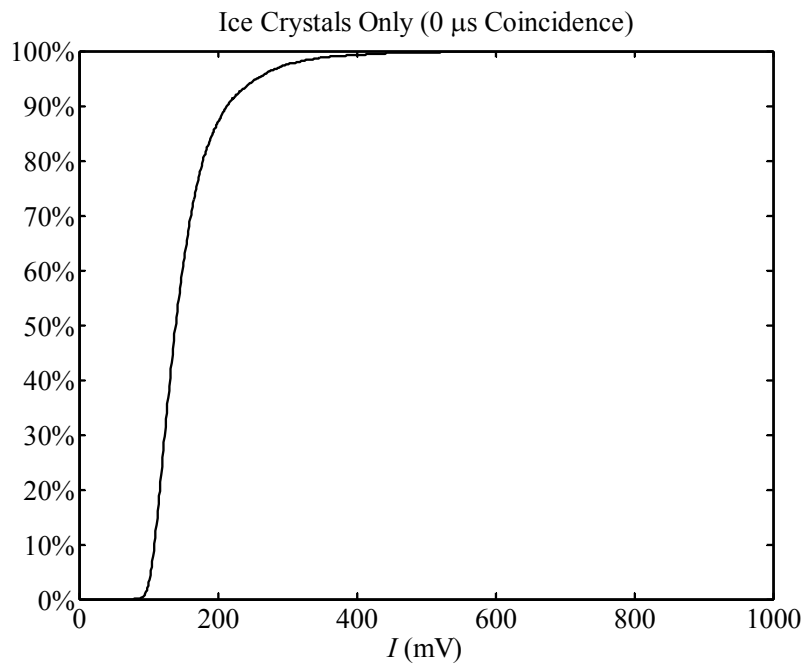
Figure 3.8: Probability distribution of ice crystal Doppler burst intensity. 99% of the ice crystal bursts have intensities less than 500 mV.

The velocity histogram of the two-phase gas-solid flow is shown in Figure 3.9. (This the same LDV data set that is plotted in Figure 3.1.) Using the aforementioned subranging criteria, the particulate and gas phase velocity histograms are presented in

Figure 3.10 and Figure 3.11, respectively. The shapes of the clearly distinguishable velocity profiles in Figure 3.9 are maintained by this subranging process. Furthermore, very few ice crystal bursts are discarded with the intensity thresholding. However, Figure 3.6 indicates that roughly 40% of the bed particle bursts are below 500 mV. This reduction in particle burst count is offset by the weaker coincidence criteria. The effect on measured particle velocity values due to this change in burst processing criteria was determined to be negligible by comparing the bed particle only measurements. This can be physically explained as follows. Since the bed particles are much larger than the LDV measurement volume, low intensity bed particle bursts are caused by particles that graze the measurement volume rather than by smaller, faster moving bed particles, which would be the case if the bed particles were on the order of or smaller than the measurement volume. Figure 3.12 supports the claim that there is no relationship between burst intensity and velocity for the bed particle bursts.

However, if there is significant lateral particle motion detected by Channel 2, increasing the coincidence period will slightly increase the measured mean velocity. This primarily occurs near the jet plume boundary and is further discussed in Chapter 5.
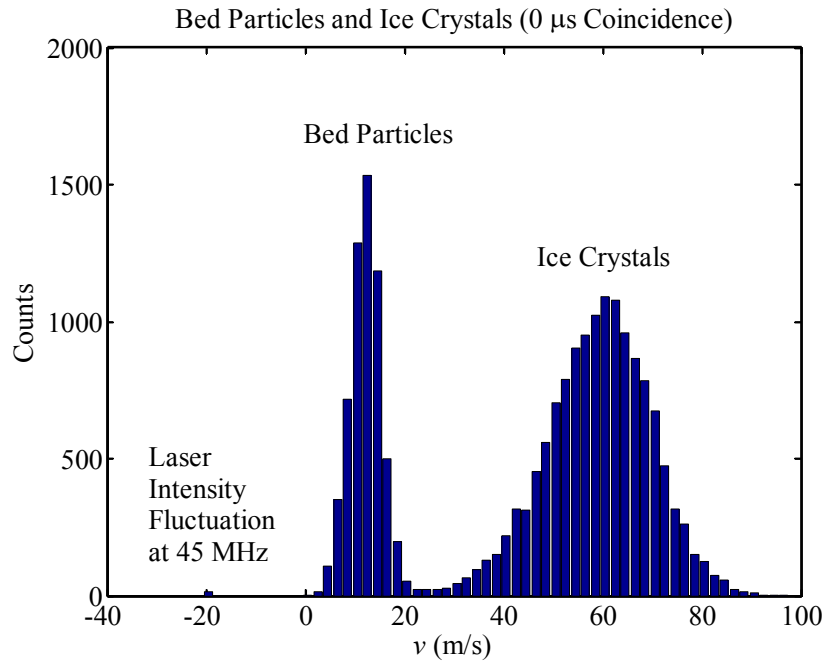
Figure 3.9: Velocity histogram for bed particles and gas tracer ice crystals measured in a jet plume.

Bed Particles Subranged ($I > 500$ mV, 10 µs Coincidence)
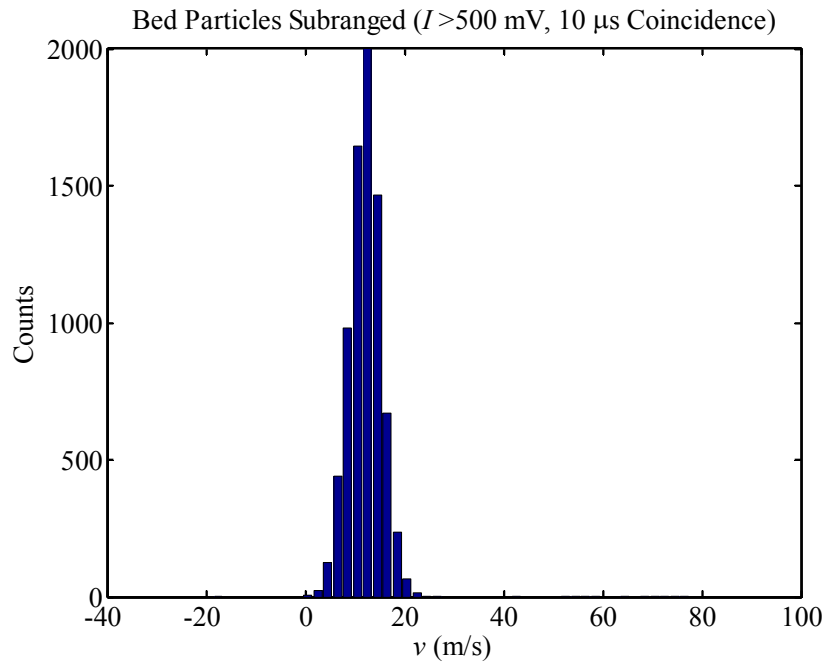
Figure 3.10: Subranged velocity histogram for bed particles measured in a jet plume.

Ice Crystals Subranged ($I < 200$ mV, 0 µs Coincidence)
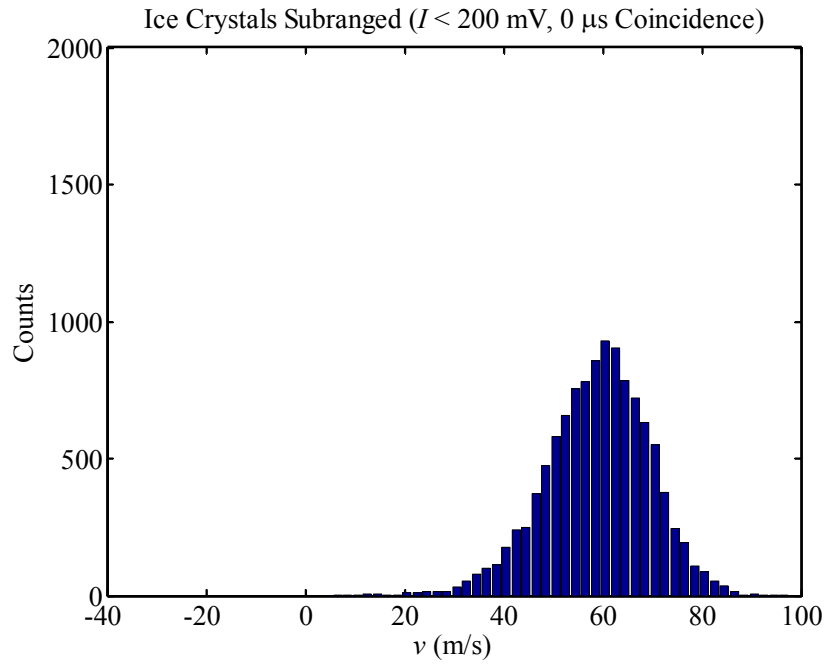
Figure 3.11: Subranged velocity histogram gas tracer ice crystals measured in a jet plume.
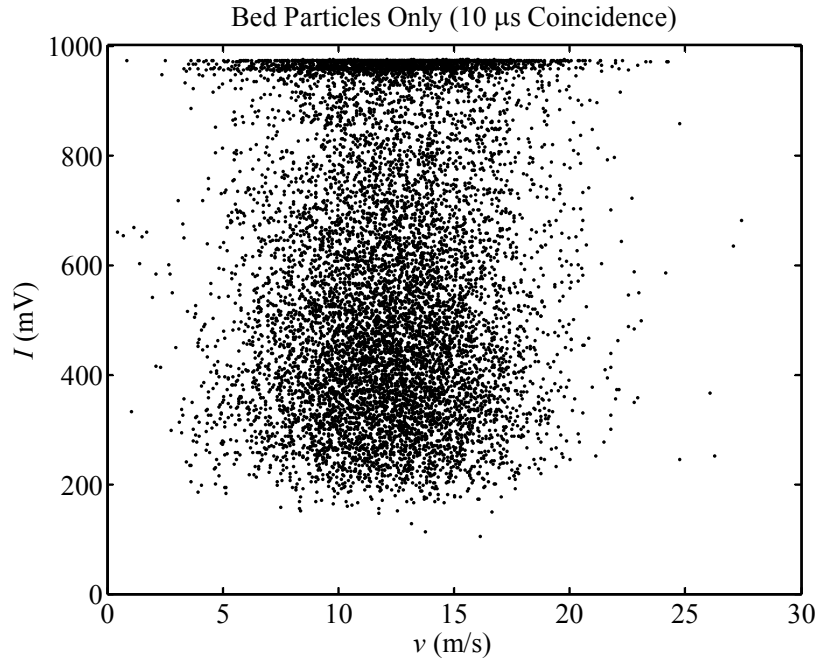
Figure 3.12: Doppler burst intensities and velocities for bed particles measured in a jet plume. There is no clear relationship between burst intensity and particle velocity, therefore intensity subranging does not bias measured mean velocity values.

3.3 Example Velocity Profiles

Gas and particulate phase velocity profiles were simultaneously recorded in a jet plume in a bubbling bed of 838 μm HDPE particles. The inlet jet velocity was 92 m/s and the fluidization velocity was 34 cm/s, which is approximately 15% greater than the minimum fluidization velocity for the emulsion. The velocity profiles for the two phases are juxtaposed at increasing axial distances in Figure 3.13 - Figure 3.16. The scales in these figures are kept constant for the purpose of visual comparison. The uncertainty for these measurements is approximately ±0.5 m/s along the centerline, ±1 m/s within the half-velocity point core region, and ±2 m/s near the edges along the plume boundary. The measurement uncertainty and repeatability is discussed in detail in Chapter 5.

The axial development for the velocity profiles of the gas and particulate phases is shown in Figure 3.17 and Figure 3.18, respectively. As would be expected, the gas phase centerline velocity decays and the profile expands with axial distance. The particulate phase velocity profile also broadens downstream. One would expect the particulate centreline velocity to increase as momentum is transferred from the jet gas to the bed particles *via* drag. However, it is important to realize that the LDV method records the

49

Eularian particulate phase velocity as a function of space and time rather than track the Lagrangian velocity of a single particle as it accelerates in the jet plume. Therefore, the average particulate phase velocity decreases downstream as particles in the emulsion are entrained from rest into the jet plume.
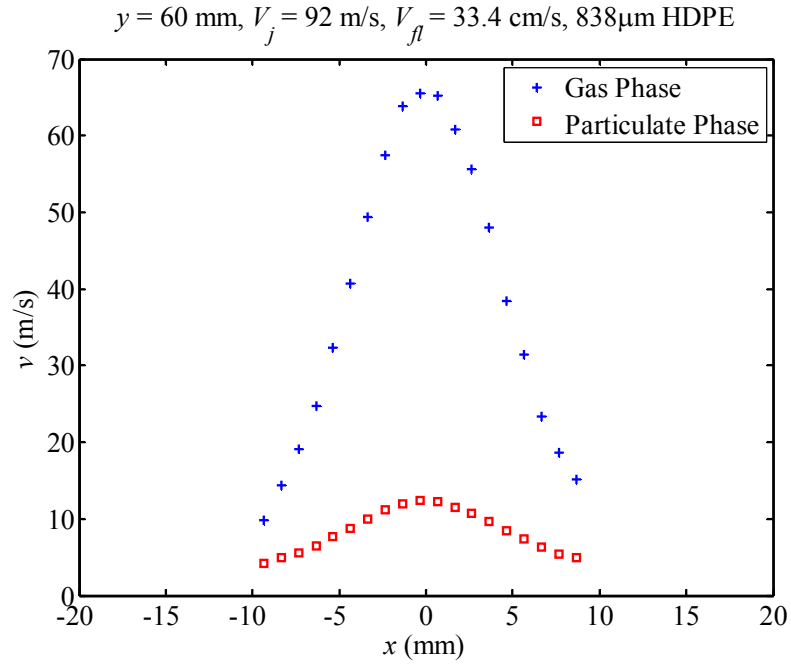
Figure 3.13: Gas and particulate phase velocity profiles at $y = 60$ mm in the vertical jet.
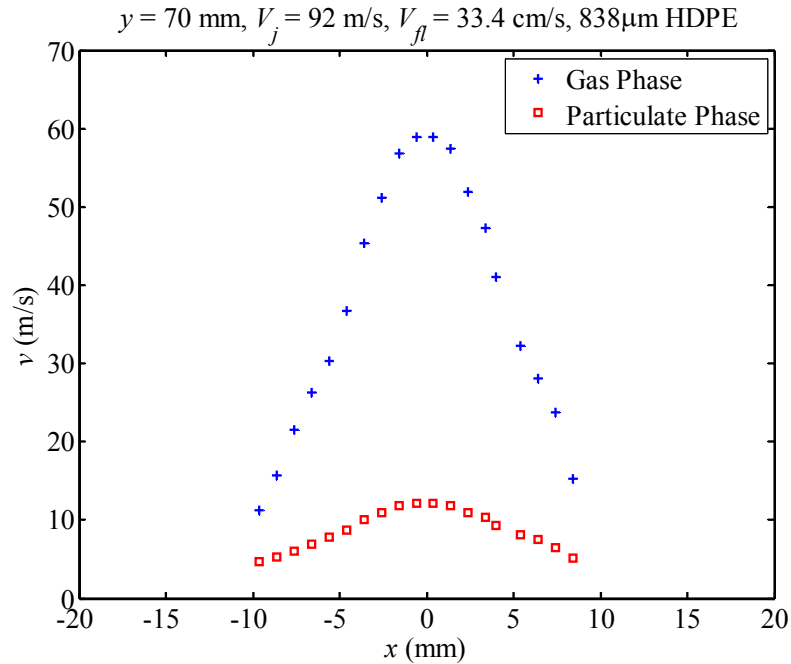
Figure 3.14: Gas and particulate phase velocity profiles at $y = 70$ mm in the vertical jet.
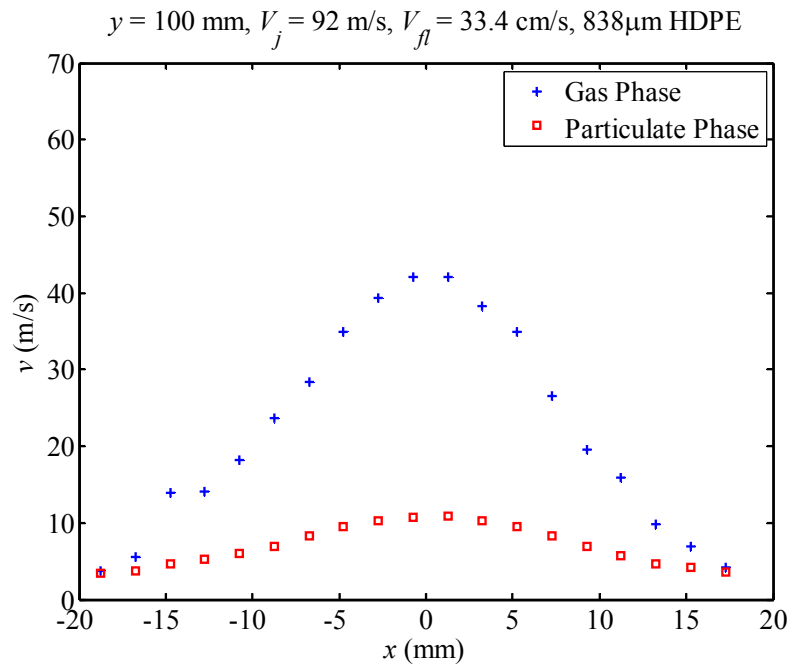
Figure 3.15: Gas and particulate phase velocity profiles at $y = 100$ mm in the vertical jet.
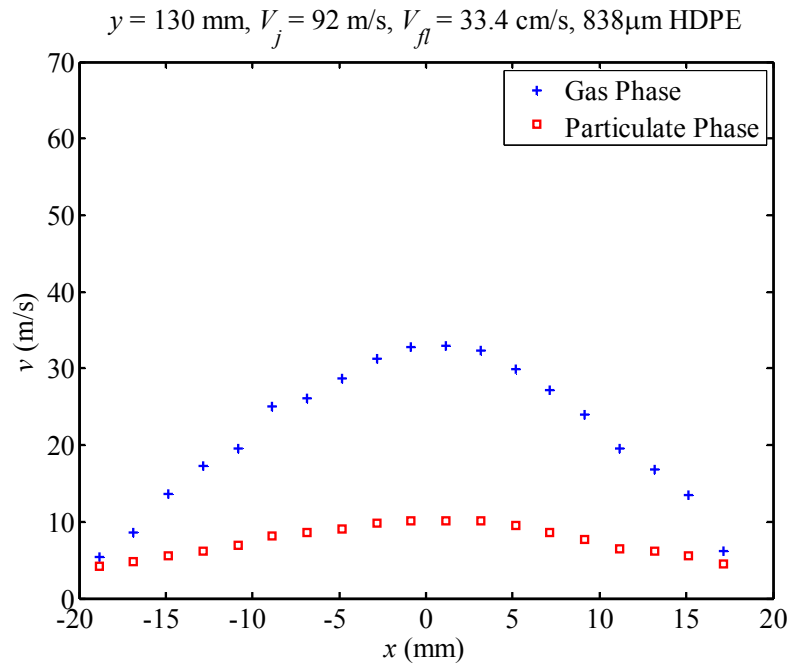
Figure 3.16: Gas and particulate phase velocity profiles at $y = 130$ mm in the vertical jet.
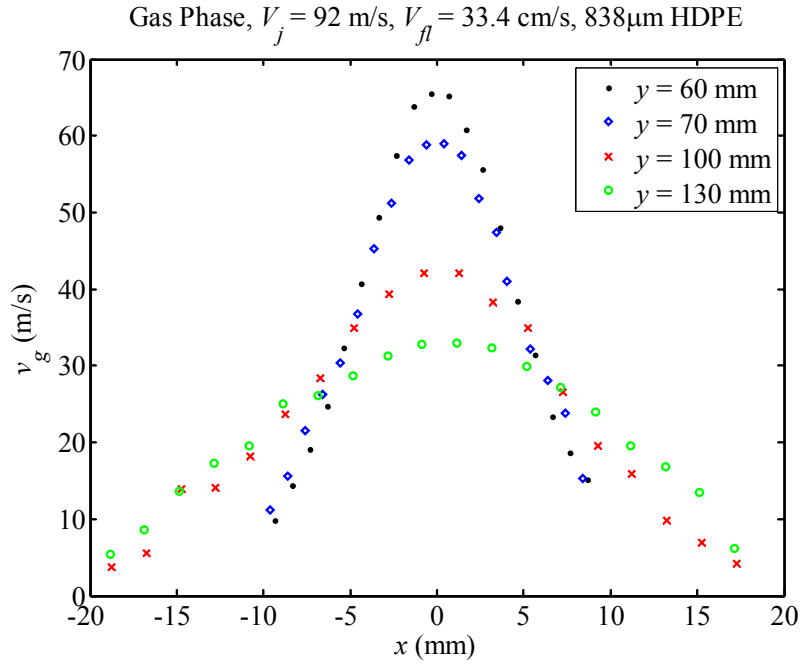
Figure 3.17: Gas phase velocity profiles the vertical jet.
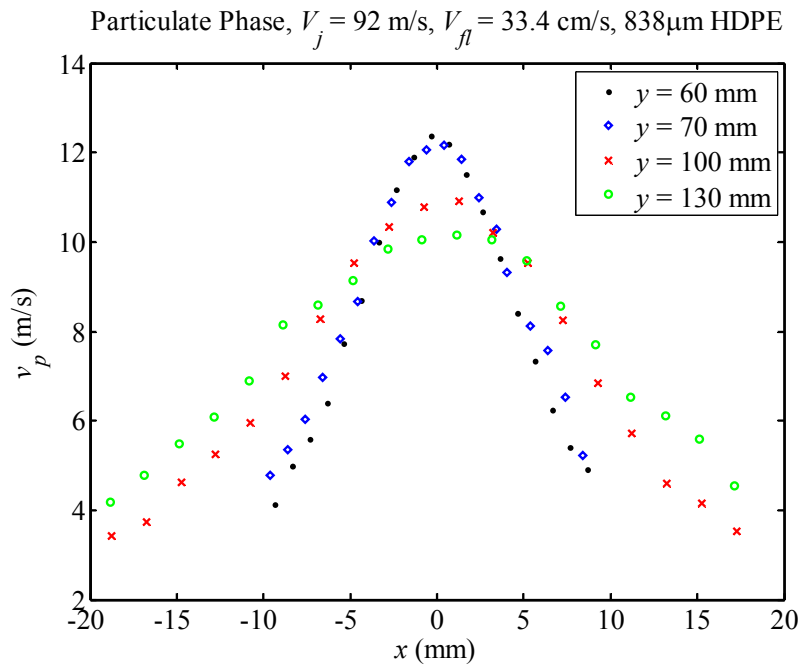
Figure 3.18: Particulate phase velocity profiles the vertical jet.

3.4 Chapter 3 References

S.A. Ahmed, A.S. Nejad , A. Al-Garni. "Near-field Study of a Turbulent Free Jet and Velocity Bias Effects,"   J. Propul. Power, **12** (1), 155-158 (1996).

R.S. Barlow & C.Q. Morrison. "Two-phase velocity measurements in dense particle-laden jets," Exp. Fluids., **9** (1-2), 93–104 (1990).

F.P. Grosu, M.K. Bologa, A.A. Polikarpo, O.V. Motorin. "On modeling of processes of moisture circulation and electric charge separation in the atmosphere," Surf. Eng. Appl. Electrochem., **43** (3), 176-181 (2007).

T. F. Johnston, Jr., M. W. Sasnett, Jean-luc Doumont, A. E. Siegman, "Laser beam quality versus aperture size in a cw argon-ion laser," Opt. Lett. **17** (3), 198-200 (1992).

S.L. Lee. & F. Durst. "On the motion of particles in turbulent duct flows," Int. J. Multiphase Flow, **8** (2), 125-146 (1982).

CHAPTER 4:

EMPTY BED GAS PHASE VELOCITY PROFILES AND ANALYSIS

Before attempting to quantify and analyze two-phase measurements in the bubbling bed jet plume, the behavior of the single-phase gas jet in the empty 2D bed was examined. The jet inlet velocity profile, bed gap velocity profile, fluidization distributor velocity profile, and empty bed single-phase gas jet velocity profiles in the plume are presented and analyzed in this chapter.

4.1 Jet Inlet Velocity Profile

As described in Chapter 3, the jet gas was seeded with ice crystals, which are formed by rapidly cooling air moisture *via* a dry ice heat exchanger to -10$^{\text{o}}$C. (Note that for the two-phase bubbling bed tests, T_j = -5$^{\text{o}}$C. The slightly warmer jet gas temperature is used to minimize the buildup of static charge in the emulsion. The colder jet gas temperature in the empty bed is used to augment the ice crystal seeding, which is needed to obtain velocity measurements at the extents of the jet inlet orifice and bed gap). A smooth tube of 9.2 mm inner diameter and 350 mm long was set flush with the top surface of the fluidization distributor (12.7 mm wide) to produce the jet. A smooth inlet velocity profile obtained with this setup is shown in Figure 4.. Measurements were taken at 0.1 mm increments, which is approximately the spatial resolution in the *x,y* plane of the LDV measurement volume.

The jet was run at a volumetric flow rate of 400 SLPM. Taking into account the increase in air density (ρ_j = 1.342 kg/m^3) *via* equation (4.1), the average inlet velocity is approximately 90 m/s at these conditions. Note that this velocity profile was obtained with a longer focal length LDV lens, which increased the measurement volume fringe spacing so that higher velocities could be recorded with the Doppler burst band pass

filter. The walls of the 2D fluidized bed were removed for these measurements to provide access to the jet orifice. This long focal length configuration is not possible with the walls present, as the elongated LDV measurement volume recorded spurious zero velocity bursts due to stationary blemishes on the viewing windows as well as increased spurious signals due to intensity fluctuations.

$$V_j = \frac{\dot{Q}_j(-10^o C)}{A_j} = \frac{\rho(20^o C)}{\rho(-10^o C)} \frac{\dot{Q}_j(20^o C)}{A_j}$$

(4.1)
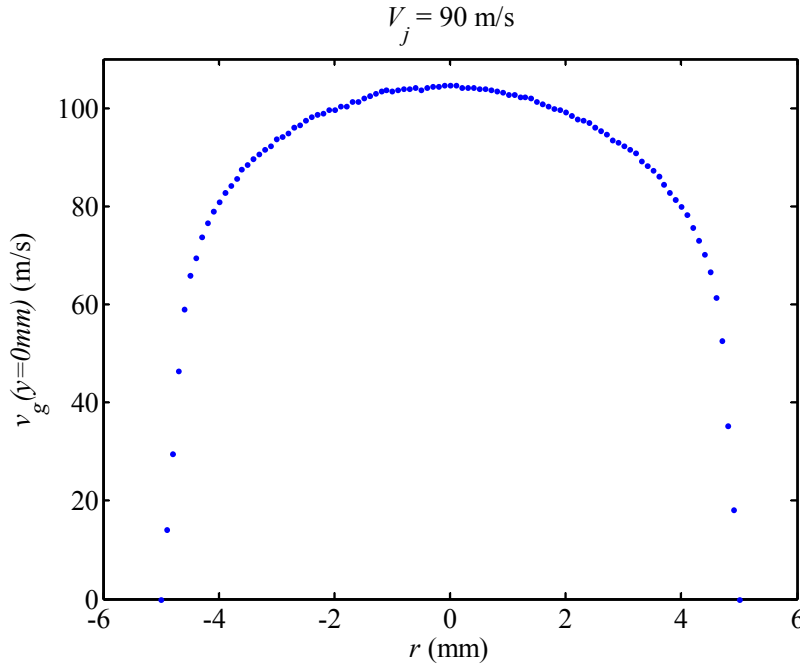
Figure 4.**1**: Jet inlet velocity profile. The inlet momentum based on the average inlet velocity is 0.722 kg.m/s^2 and is measured to be 0.716 kg.m/s^2 based on this velocity profile.

The jet inlet mass flow rate is 8.0 g/s based on the average inlet velocity using equation (4.2). The mass flow rate calculated by integrating this velocity profile with respect to its circular cross sectional area, according to equation (4.3), is 7.9 g/s. Likewise, the jet inlet momentum rate is 0.722 kg.m/s^2 based on the average inlet velocity. The momentum rate calculated by integrating this velocity profile with respect to its circular cross sectional area, according to equation (4.5), is 0.716 kg.m/s^2.

$$\dot{m}_j = \rho_j V_j A_j \qquad\qquad (4.2)$$

$$\dot{m}_g(y=0) = \rho_j \int_0^{D/2} v_g \, 2\pi r dr \qquad\qquad (4.3)$$

$$\dot{J}_j = \rho_j V_j^2 A_j \qquad\qquad (4.4)$$

$$\dot{J}_g(y=0) = \rho_j \int_0^{D_j/2} v_g^2 \, 2\pi r dr \qquad\qquad (4.5)$$

4.2 Bed Gap Velocity Profile

Though the jet can only spread in two dimensions, the bounding walls create a velocity gradient across the bed gap, as is shown in Figure 4.2. (LDV gas velocity measurements near the windows were not possible for reasons discussed prior.) This situation is analogous to a Hele-Shaw flow, where the velocity profile in the *z* direction is parabolic. This permits integration of the velocity profile with regard to *z* and thus consider an effective velocity field in only the two dimensions *x* and *y*. Since the LDV measurement volume is located in the middle of the bed gap, the velocity values reported in the prior velocity profiles correspond to peak values rather than average values across the bed gap. It should be noted that a short measurement volume length is necessary to ensure that in optically dense flows, the measurements are not biased towards the near window region of the measurement volume. Furthermore, the alignment of the 2D fluidized bed with respect to the LDV probe head is critical as they should be orthogonal to ensure that measurements are obtained at the same *z* location for all *x* and *y* positions.

Empty Bed, $V_j = 90$ m/s, $V_{fl} = 0$ cm/s
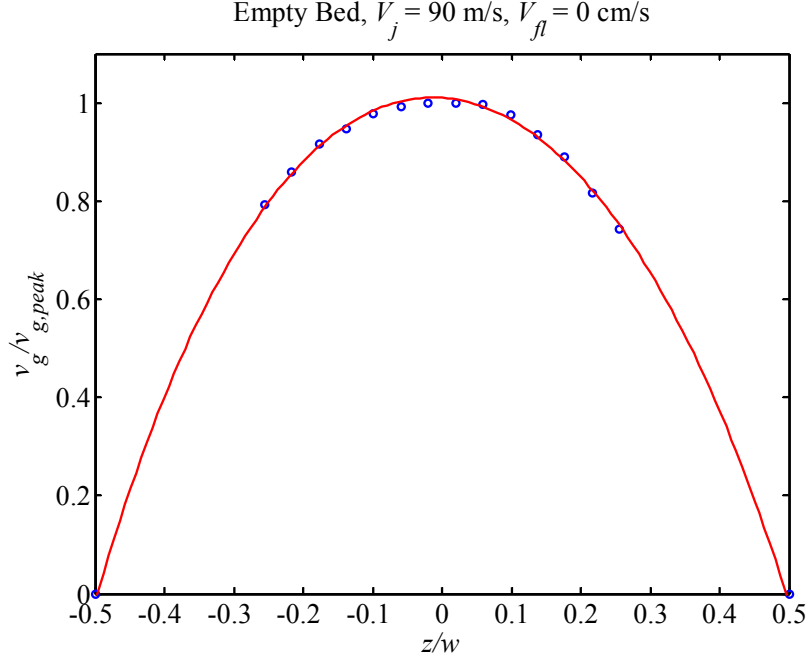
Figure 4.2: Bed gap velocity profile. $v_{g,avg} / v_{g,peak} \sim 0.7$ and $v_{g,avg}^2 / v_{g,peak}^2 \sim 0.55$.

Therefore, in order to use the integrated velocity profiles downstream to calculate the mass flow and momentum rates, relationships between the average value and the peak values across the bed gap must be used to correct for overestimations. (Note that $v_{g,peak}$ is used with respect to the 3rd dimension, whereas $v_{g,m}$ is used with respect to the transverse direction.) The average value of the velocity across the gap is about 70% of the peak value and the average value of the velocity squared is about 55% of the peak value squared, so that

$$v_{g,avg} = \frac{1}{w} \int_w v(z)dz \approx C_1 v_{g,peak} \tag{4.6}$$

$$v_{g,avg}^2 = \frac{1}{w} \int_w [v(z)]^2 \, dz \approx C_2 v_{g,peak}^2 \tag{4.7}$$

where $C_1 = 0.7$ and $C_2 = 0.55$. From this point forward, $v = v_{avg}$ and $v^2 = v_{avg}^2$ as defined by equations (4.6) and (4.7). Rather than overestimate measured values, the jet mass flow rate at any axial location should be calculated as

$$\dot{m}_g = C_1 \rho_g w \int_{-b}^{b} v_g dx \tag{4.8}$$

57

and the jet momentum rate as

$$\dot{J}_g = C_2 \rho_g w \int_{-b}^{b} v_g^2 dx \tag{4.9}$$

This situation has been observed but not properly accounted for in the literature. Xuereb *et al.* (1991) noted that the volumetric flux of air calculated by integrating jet gas velocity profiles obtained *via* pitot tube measurements in their 2D fluidized bed according to

$$\dot{Q}_g = w \int_{-b}^{b} v_g dx \tag{4.10}$$

greatly exceeded the amount of air injected and that entrained air could not account for this excessive gas flux. Most likely, the reason for this overestimation of gas flux is because the three dimensional nature of the gas velocity profile was not taken into account and the measured peak velocity values were used rather than an average value across the bed gap.

In addition to overestimating the jet mass flow rate at various downstream locations, Xuereb also overestimated the momentum rate. In order to compensate for this, the momentum fluxes at the various axial locations were normalized with

$$\rho \int_{-D_j/2}^{D_j/2} V_j^2 dx \tag{4.11}$$

where

$$V_j = \frac{\dot{Q}_j}{A_j} = \frac{\dot{Q}_j}{\frac{\pi}{4} D_j^2} \tag{4.12}$$

which is not the same as normalizing with respect to the jet inlet momentum rate since the orifice has a circular cross-sectional area. Therefore, the combination of the two expressions above essentially neglects a factor of *(π/4)²*. This overestimates the actual inlet momentum rate but was necessary for normalization so that the momentum rates reported downstream did not exceed the inlet value.

4.3 Fluidization Distributor Velocity Profile

The other source of air into the bubbling bed is the fluidization distributor, which is a 12.7 mm thick porous ultra-high molecular weight (UHMW) polyethylene. The velocity profile was measured approximately 20mm above the distributor surface and is shown in Figure 4.3. This was done by placing a small amount of talcum powder on the surface of the distributor to seed the air for LDV measurements. The profile is rather symmetric about $x = 225$ mm, where the tube for the vertical gas jet is located. The velocity peaks near the edges are due to the geometry of the distributor material. The distributor material has a large radius on either end for the purpose of o-ring seals. The bed cross sectional area is rectangular so the constriction of cross sectional area near the end regions produces the high local velocities.
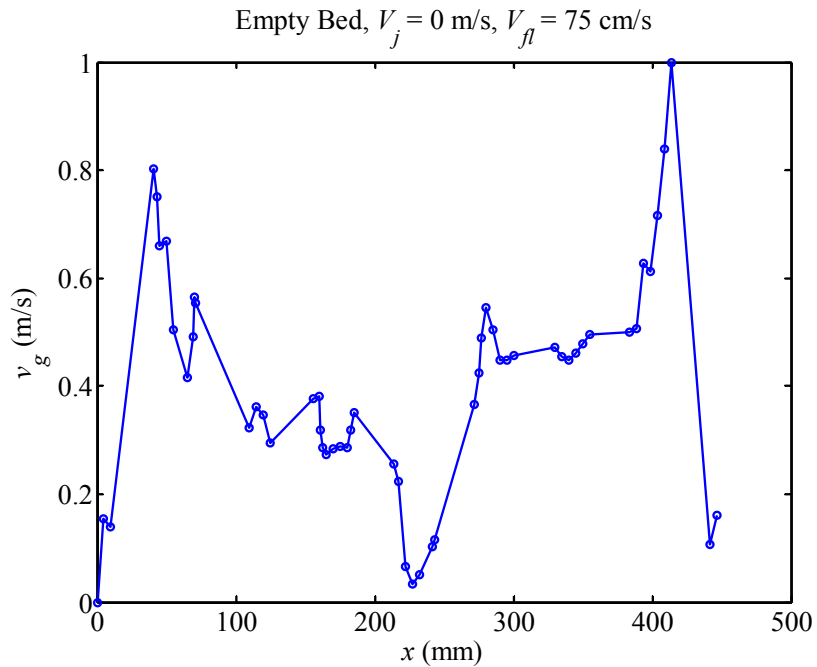
Figure 4.3: Fluidization distributor velocity profile. The profile is symmetric about the jet inlet located at $x = 225$ mm. The velocity peaks at the ends is due to a cross-sectional area constriction of bed riser with respect to the distributor plate necessary for the o-ring seals.

4.4 Gas Phase Velocity Profiles in a Single Phase Plume

4.4.4 Similarity
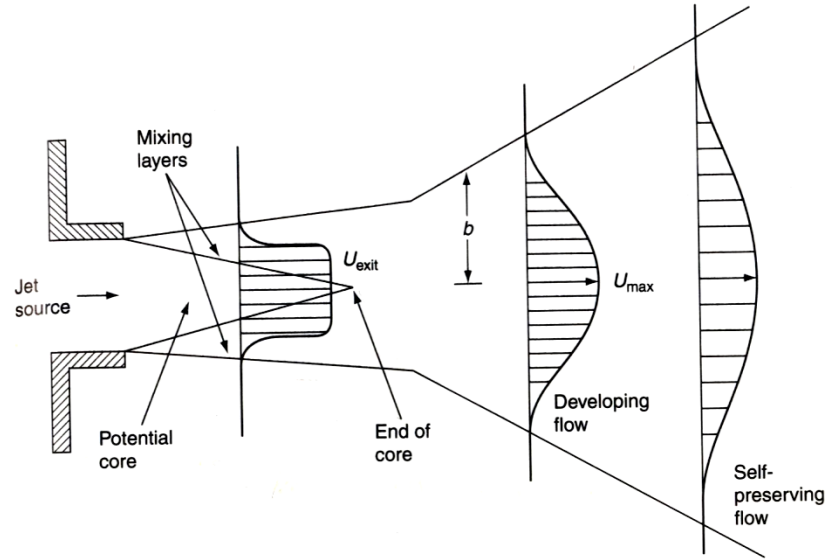
Figure 4.4: Single-phase turbulent jet (White, 2006). The self-similar gas velocity profiles develop with respect to a virtual origin located downstream from the jet inlet.

A schematic of a single-phase turbulent jet is shown in Figure 4.4 (White, 2006). (Note that since this is a horizontal jet, y is the axial coordinate and x is the transverse coordinate.) In the absence of any bounding walls, free turbulent jets are characterized by a single velocity scale and a single length scale which are both functions of the axial coordinate. The characteristic velocity scale is the maximum, centerline axial velocity, $v_m(y)$, and the characteristic length scale is the shear-layer, or jet plume half-width $b(y)$. The absence of multiple velocity and length scales yields a similarity, or self-preserving, velocity profile for the jet of the form

$$v_g = v_{g,m}(y) f\left(\frac{x}{b_g(y)}\right)$$

(4.13)

where $v_{g,m}(y)$ is a stretching factor and $f(x/b_g(y))$ describes the shape of the velocity profile at each axial location. Dimensional analysis shows that the jet plume width varies linearly in the axial direction for both plane and round turbulent jets

$$b_g = (const)y \qquad (4.14)$$

so that equation (4.13) can be written as

$$v_g = v_{g,m}(y)g\left(\frac{x}{y}\right) \qquad (4.15)$$

Applying Newton's 2nd Law to a control volume about the jet plume requires that the centerline velocity decay as

$$v_{g,m}(y) \sim y^P \qquad (4.16)$$

where $P = -1/2$ for an unbounded 2D jet and $P = -1$ for an unbounded 3D jet. It should be noted that a classic 2D jet is formed with a very long, narrow injection slot. However, this configuration is not practical in a fluidized bed, for optical access reasons, as it would require a very large bed gap. Therefore, instead of being infinitely long in the 3rd dimension, 2D fluidized beds simply restrict the bed particle and gas movement to a plane formed by a narrow gap between two bounding walls. Jet cross-sectional velocity profiles were measured at various axial locations at the inlet conditions described in Section 4.1. The jet cross-sectional velocity profiles taken at axial locations of $y = 70$ mm, 100 mm, and 130 mm are shown in Figure 4.5.

  The velocity profiles at each axial location are normalized with respect to the maximum value and plotted versus the similarity variable x/y in Figure 4.6 in order to determine if a self-similar shape exists. Notice in this Figure that the data is plotted with respect to the physical origin of the jet. The illustration in Figure 4.4 indicates that the self-similar behavior of jets occurs with respect to the virtual (or apparent) origin, located at y_o. The apparent origin is a hypothetical point source of momentum, whose location is related to the decay of the potential core, which usually occurs at a distance of a few jet orifice diameters. Unfortunately, there is no explicit relationship between jet inlet conditions and the location of the virtual origin, and the nature of its existence has been studied for years (Kotsovinos, 1976). Therefore, the location is experimentally determined by plotting the normalized velocity profiles with respect to

$$\eta = \frac{x}{y - y_o} \qquad (4.17)$$

and varying the value of y_o so that the curves at the various axial locations collapse to a single, self-similar curve. Figure 4.7 shows the normalized profiles plotted with respect to η with $y_o = 2D_j = 18.4$ mm.

A logarithmic plot of the axial decay of the maximum axial velocity with respect to the virtual origin is shown in Figure 4.8, where the variables are scaled based on a momentum balance with the jet inlet. The maximum velocity decays approximately as $(y-y_o)^{-1/2}$, indicating two-dimensional spreading with negligible momentum lost to wall friction. For the 2D gas jet, the normalized profiles and axial plots can be combined by scaling the velocity by

$$\frac{v_g(y - y_o)^{1/2}}{V_j(D_j^2/w)^{1/2}} \tag{4.18}$$

as shown in Figure 4.9. This is a more comprehensive plot if the nature of the axial decay is known because the similarity profile comparison does not depend on the exact correct measured value of v_m for normalization. However, note that the theoretical axial decay behavior is derived from the conservation of momentum and therefore this type of scaling is not necessarily applicable to a two phase jet.
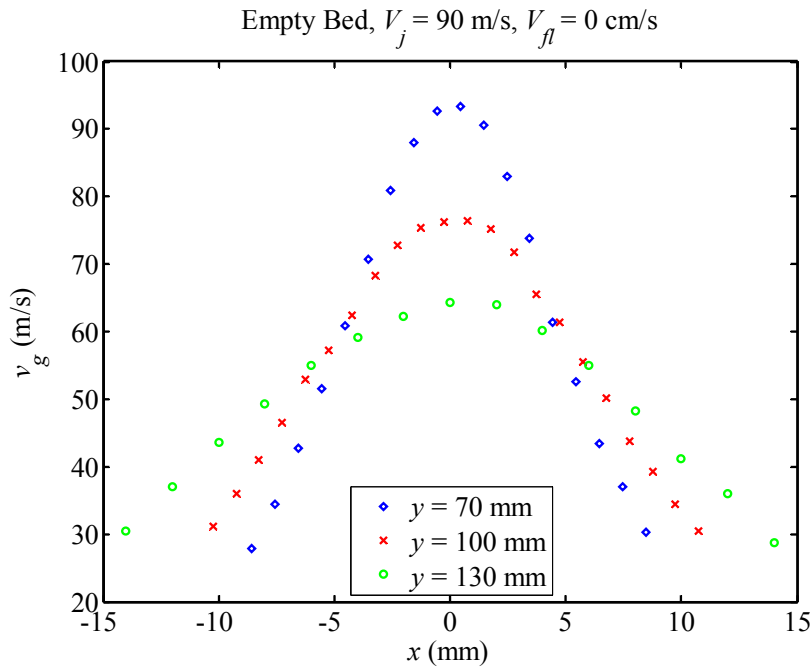
Figure 4.5: Gas phase velocity profiles.
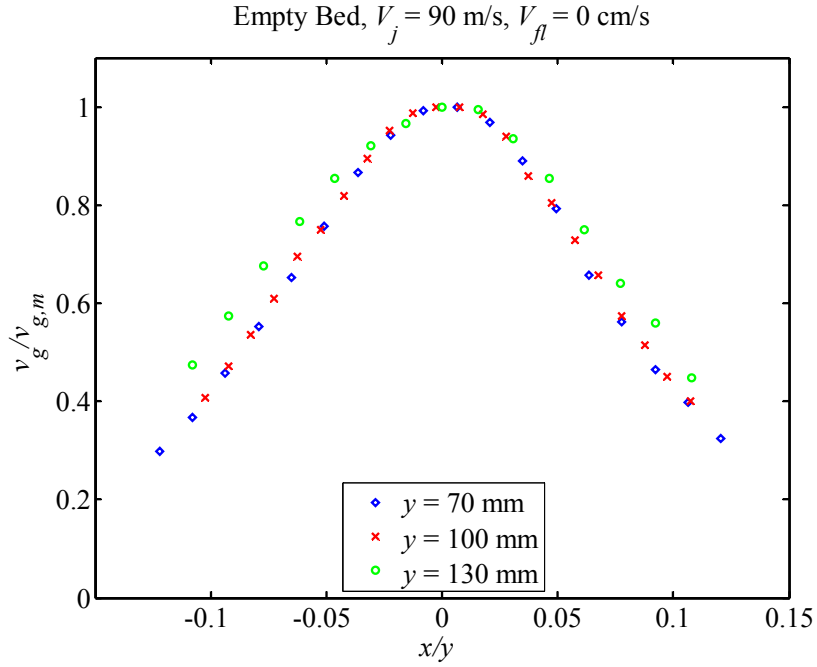
Figure 4.6: Normalized gas phase velocity profiles scaled with respect to the physical origin.
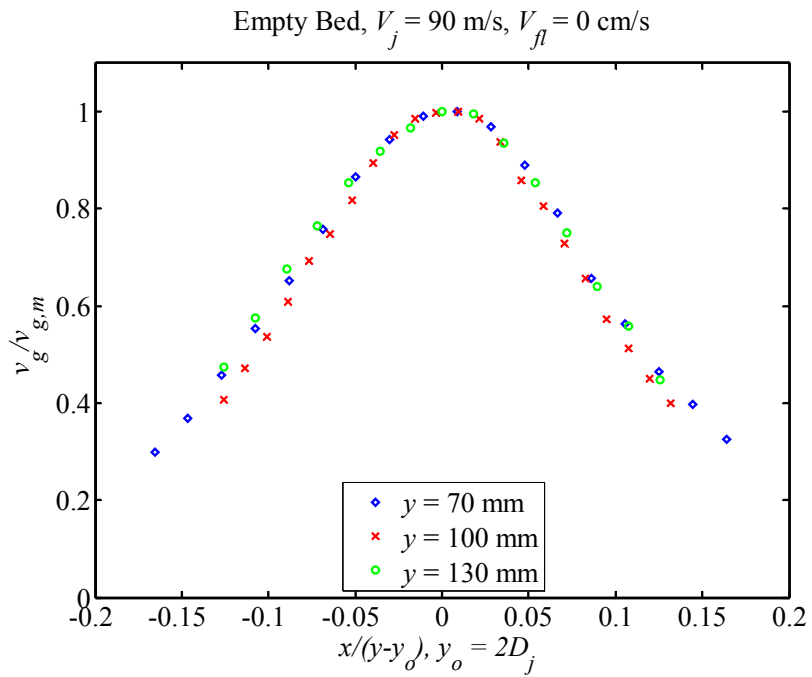
Figure 4.7: Normalized gas phase velocity profiles scaled with respect to the virtual origin, located two jet inlet diameters downstream from the jet inlet. The velocity profiles appear self-similar.

Empty Bed, $V_j = 90$ m/s, $V_{fl} = 0$ cm/s

$$v_{g,m}/V_j \sim (D_j^2/w)^{1/2}(y-y_o)^{-1/2}$$
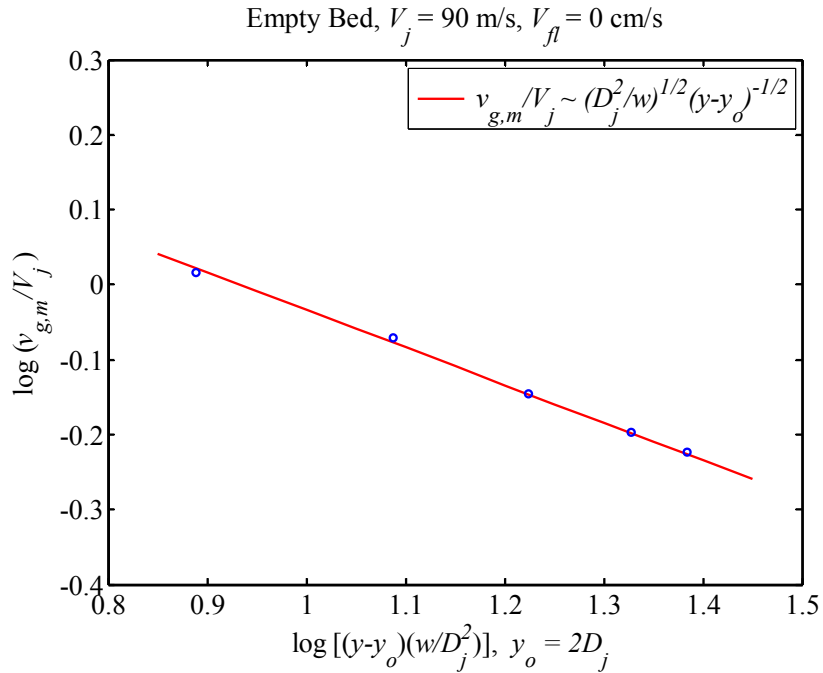
Figure 4.8: Axial decay of maximum gas phase velocity. The experimental data agrees well with the theoretical decay.

Empty Bed, $V_j = 90$ m/s, $V_{fl} = 0$ cm/s

$y = 70$ mm
$y = 100$ mm
$y = 130$ mm
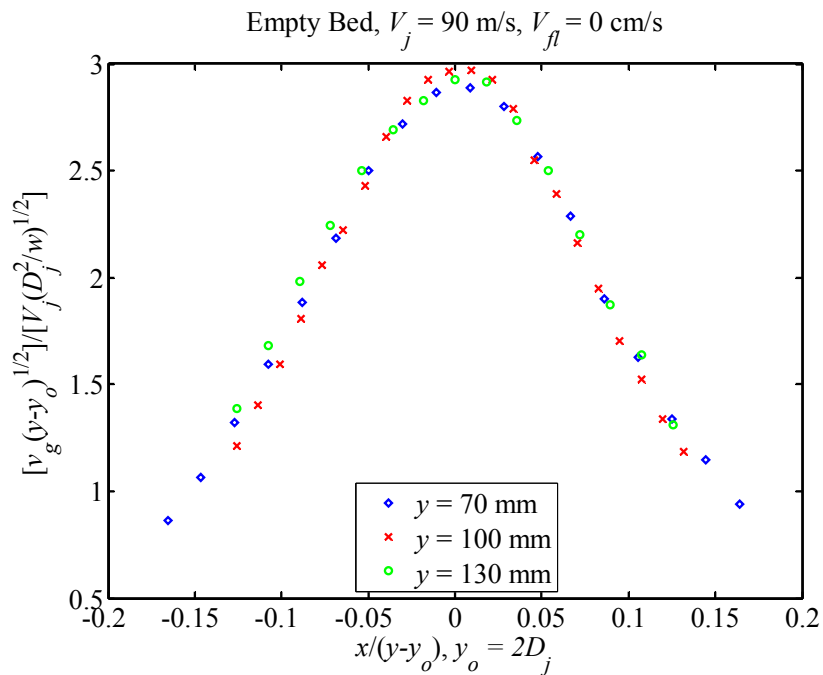
Figure 4.9: Normalized gas phase velocity profiles scaled with respect to the theoretical axial decay.

It has been shown that the gas jet in the empty bed behaves as a self-similar 2D turbulent jet. However, there are several ways to describe the bell-curve like shape of the velocity profile at a given axial location. The most common profile referenced for the jet

plume velocity distribution in a fluidized bed is the Schlichting profile (Merry, 1971; Shakhova & Minaev, 1970). This Schlichting model is based on Prandtl's old mixing length theory, which states that the turbulent mixing length is only a function of the streamwise direction and thus a constant value at a given axial location. The self-similar profile, based on this model, has the shape

$$\frac{v_g}{v_{g,m}} = \left(1 - \zeta_g^{1.5}\right)^2$$

(4.19)

where the similarity variable is normalized by the plume half-width

$$\zeta_g = \frac{x}{b_g}$$

(4.20)

which is defined as

$$v_g(x = b_g) = 0$$

(4.21)

and can be related to the half-velocity location by solving equation (4.19) for $v_g/v_{g,m} = \frac{1}{2}$.

$$b_g = \frac{x_{g,1/2}}{0.441}$$

(4.22)

However, it should be noted that this self-similar profile was developed for a 2D wake rather than for a 2D jet (Abramovich & Schindel, 1963; Schlichting, 1979). Though the centerline velocity for both a 2D turbulent jet and wake decay as $y^{-1/2}$, the plume growth differs. For a 2D plane turbulent wake, the plume spreads as $y^{1/2}$ rather than y. Therefore, equations (4.14) and (4.15) do not hold for wake models since there is not a linear relationship between the plume width and the axial distance. Thus, equation (4.20) is used for the similarity length scaling rather than equation (4.17).

A theoretical velocity profile for a 2D plane jet was developed by Grotler (White, 2006) and is based on on Prandtl's new theory of free turbulence, based on Clauser's outer wake model, which assumes that the coefficient of turbulent viscosity, rather than the mixing length, is constant over a cross section of the jet. This results in a self-similar profile

$$\frac{v_g}{v_{g,m}} = \operatorname{sech}^2(C\eta)$$

(4.23)

65

where the similarity variable is defined by equation (4.17) and the constant $C = 7.67$ for a 2D free turbulent jet. The half-maximum velocity transverse location is defined at

$$v_g(x = x_{g,1/2}) = \tfrac{1}{2}v_{g,m} \tag{4.24}$$

and is found by solving for equation (4.23):

$$x_{g,1/2} = 0.1147(y - y_o) \tag{4.25}$$

Note that the definition of the jet plume half-width is given by twice the half-velocity point

$$b_g = 2x_{g,1/2} = 0.229(y - y_o) \tag{4.26}$$

since $sech^2$ has an asymptotic behavior, which corresponds to a jet plume half-angle of 13°. Finally, for the sake of computational ease, a Gaussian profile is often used (Ounnar, 2009). This profile is intended for 2D wakes however its shape is also based on the Clauser eddy-viscosity model (White, 2006).

$$\frac{v_g}{v_{g,m}} = \exp\left[-\ln(2)\,\xi_g^2\right] \tag{4.27}$$

where the similarity variable is scaled with the half-velocity point

$$\xi_g = \frac{x}{x_{g,1/2}} \tag{4.28}$$

Using the Gaussian profile, the half-velocity point of the data can be determined rearranging equations (4.27) and (4.28) into equation (4.29), as shown in Figure 4.10. Note that the measured values of v_g slightly deviate from the Gaussian shape near the plume boundaries. This is most likely due to sparser ice crystal seeding and thus lower Doppler burst data rate in the jet boundary region. Therefore, only data in the jet core within the half-velocity point ($v/v_{g,m} > \tfrac{1}{2}$ so that $[-ln(v/v_m)/ln(2)]^{1/2} < 1$) was considered when determining the value of the half velocity point, since this is where the majority of the mass and momentum flux occurs.

$$x_{g,1/2} = \frac{x}{\sqrt{\dfrac{\ln\left(\dfrac{v}{v_{g,m}}\right)}{-\ln(2)}}}$$

(4.29)

The half-velocity point values determined from the measured velocity profiles are in good agreement with equation (4.25), as is shown in Figure 4.11. The linear expansion of the plume is confirmed in Figure 4.12, therefore $\eta = x/(y-y_o)$ is a valid similarity scaling for the single phase gas jet velocity profiles. However, it should be noted that measured half-angles of spread for free jets have varied in the literature and can depend on the consideration of the virtual origin (Horn & Thring, 1956).

In order to compare the shapes of the various velocity profiles described by equations (4.19), (4.23), and (4.27), the linear jet plume spreading given by equation (4.25) is used for all three theoretical profiles, which are juxtaposed with the data in Figure 4.13.
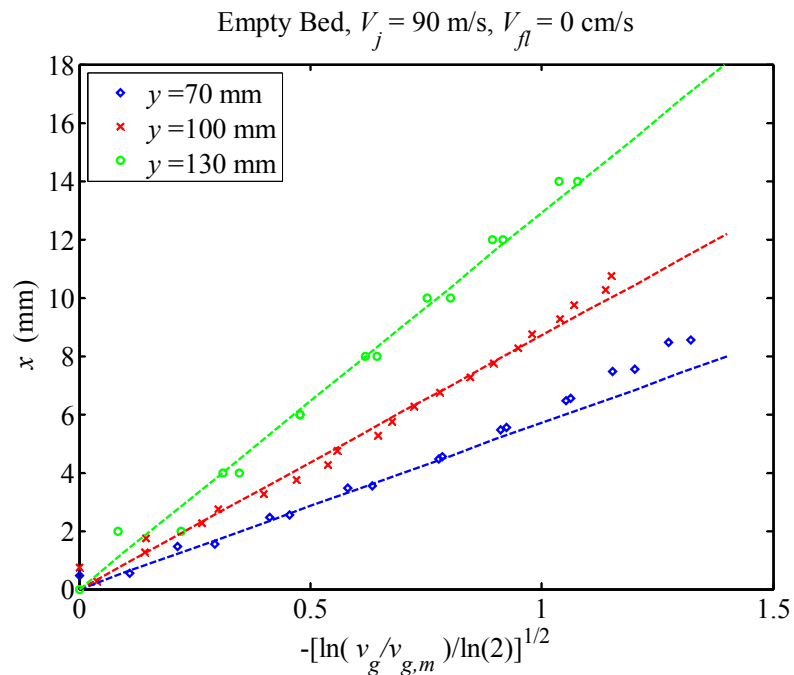
Figure 4.10: Half-velocity point values for Gaussian profiles are determined from the slope of the core data.
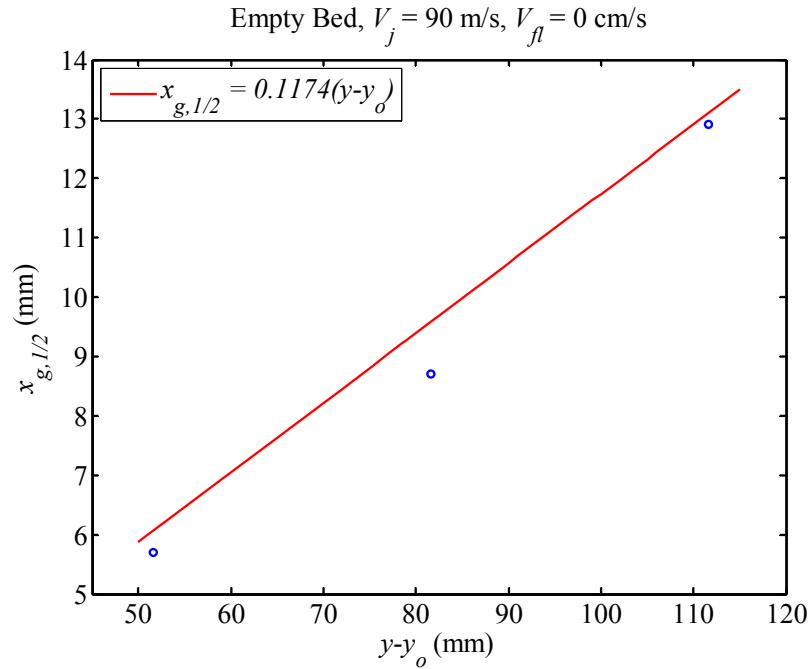
Figure 4.11: Half-velocity point values compared with the theoretical single phase 2D jet expansion.
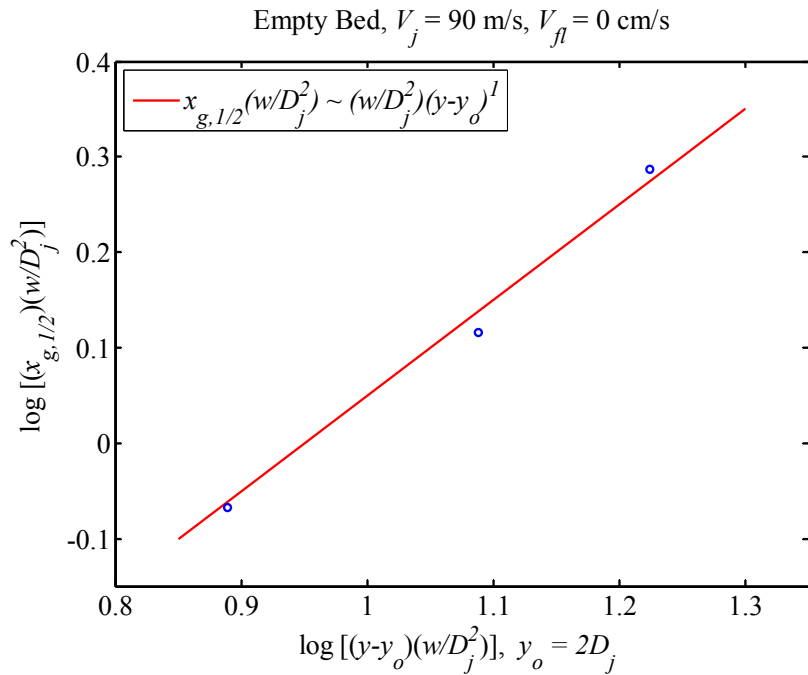
Figure 4.12: Axial spreading of the jet plume. The experimental data agrees well with the theoretical expansion.
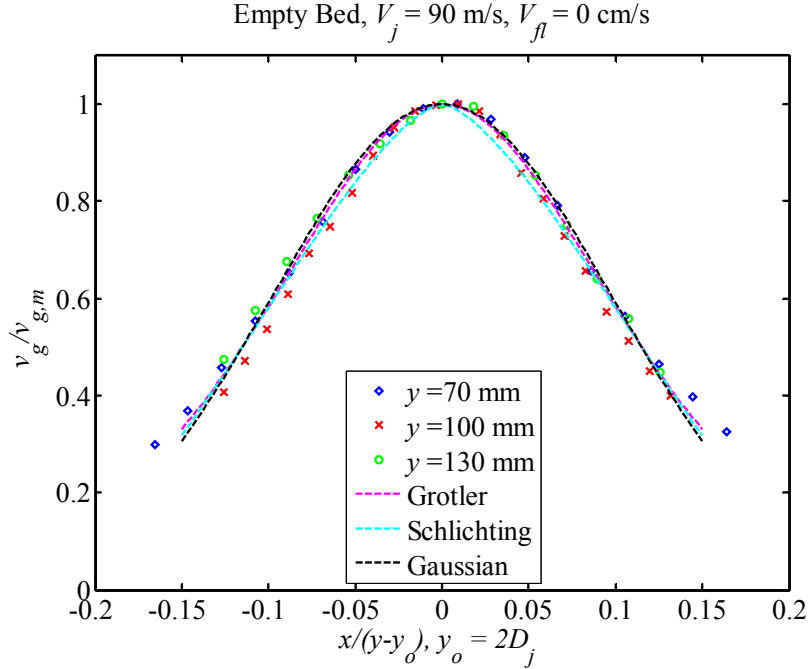
Figure 4.13: Normalized gas phase velocity profiles scaled with respect to the virtual origin compared to theoretical similarity profile shapes.

4.4.4.3 Mass Flow and Momentum Rates

One of the defining characteristics of a free jet is that its axial momentum is conserved. The vertical jet gas momentum flux can be measured at an axial location by integrating measured velocity profiles according to equation (4.9). Momentum rates calculated by numerically integrating the LDV data points are reported in Table 4.1.

Physical Location, y (mm)	J_g (kg.m/s^2)
0	0.722
70	0.723
100	0.679
130	0.697

Table 4.1: Momentum rates in the jet plume determined from numerical integration of the LDV data points.

The momentum rates calculated for the downstream locations of 70 mm, 100 mm, and 130 mm are all consistent, indicating that the jet does not lose significant momentum to friction with the bounding walls. Note that had the 3D correction constants discussed

in Section 4.2 not been used, the momentum rates calculated downstream would actually exceed the inlet momentum rate by nearly a factor of two.

It is not always possible to obtain LDV measurements across the entire jet plume width, as only the gas that originates from the orifice is seeded and therefore the data rate diminishes towards the plume boundaries. Therefore, it may be necessary to use one of the velocity profile curves that fit the data in order to carry out the integration. Written in terms of a similarity velocity profile, the jet momentum rate is

$$\dot{J}_g = C_2 \rho_g w \int_{-b}^{b} v_{g,m}^2 \left[f\left(\frac{x}{x_{g,1/2}}\right) \right]^2 dx \tag{4.30}$$

Changing the variable of integration to $\xi = x/x_{g,1/2}$ yields

$$\dot{J}_g = C_2 \rho_g w \left(v_{g,m}^2 x_{g,1/2} \right) \int_{-2}^{2} [f(\xi)]^2 d\xi \tag{4.31}$$

Only the maximum velocity and half-velocity width are functions of axial distance and all the other terms are constant. The finite integral can be evaluated for a given similarity velocity profile shape. For the sake of computational ease, the Gaussian profile is used. This can be analytically integrated with the error function so that

$$\int_{-2}^{2} [f(\xi)]^2 d\xi = \int_{-2}^{2} \exp\left[-2\ln(2)\xi^2 \right] d\xi = \sqrt{\pi} \left[2\ln(2) \right]^{-1/2} erf\left\{ 2[2\ln(2)]^{1/2} \right\} = 1.50 \tag{4.32}$$

Therefore, the momentum rate can be simply calculated as

$$\dot{J}_g = 1.5 \, C_2 \rho_g w \left(v_{g,m}^2 x_{g,1/2} \right) \tag{4.33}$$

Using experimental values for $v_{g,m}$ and $x_{g,1/2}$ at the various axial locations the calculated momentum rates based on the integration of the Gaussian similarity velocity profile are reported in Table 4.2. The Gaussian velocity profile, normalized with respect to the experimental values for $v_{g,m}$ and $x_{g,1/2}$, is shown with the experimental data in Figure 4.14.

Empty Bed, $V_j = 90$ m/s, $V_{fl} = 0$ cm/s
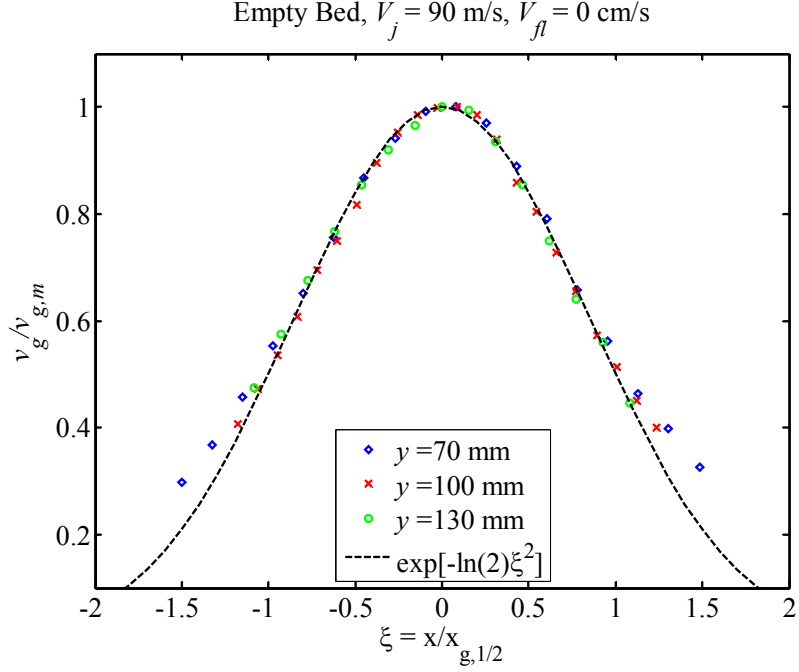
Figure 4.14: Normalized gas phase velocity profiles scaled with respect to the half-velocity points and compared to the Gaussian profile.

Physical Location, y (mm)	J_g (kg.m/s^2)
0	0.722
70	0.701
100	0.715
130	0.754

Table 4.2: Momentum rates in the jet plume determined from the Gaussian profiles.

The mass flow rate, expressed in terms of the similarity velocity profile is

$$\dot{m}_g = C_1 \rho_g w \left(v_{g,m} x_{g,1/2} \right) \int_{-2}^{2} f(\xi) \, d\xi \tag{4.34}$$

Again, using the Gaussian profile, the value of the finite integral is

$$\int_{-2}^{2} [f(\xi)] d\xi = \int_{-2}^{2} \exp\left[- \ln(2)\xi^2\right] d\xi = \sqrt{\pi} \left[\ln(2)\right]^{-1/2} erf\left\{2[\ln(2)]^{1/2}\right\} = 2.09 \tag{4.35}$$

So that the mass flow rate can be simply calculated as

$$\dot{m}_g = 2.09 \, C_1 \rho_g w \left(v_{g,m} x_{g,1/2} \right) \tag{4.36}$$

71

The jet mass flow rate calculated at the three downstream axial locations using experimental values for $v_{g,m}$ and $x_{g,1/2}$ are reported in Table 4.3 and plotted in Figure 4.15. It is evident that the mass flow of the jet increases with axial location, as is expected with entrainment of the surrounding air. For a 2D turbulent jet, $v_{g,m} \sim (y\text{-}y_o)^{-1/2}$ and $x_{g,1/2} \sim (y\text{-}y_o)^1$, therefore, according to equation (4.36), $m_g \sim (y\text{-}y_o)^{1/2}$.

Note that since the self-similar streamwise behavior of the single phase gas jet parameters are described with respect to the virtual origin, data in the figures will be plotted against $(y\text{-}y_o)$ to illustrate this. Therefore, a shift in the location of the virtual origin would not change the values of the reported data, only its functional relationship with the chosen axial reference coordinate. However, the data in the tables will be reported with respect to the physical location within the jet plume, y, since the inlet values are also considered.

Physical Location, y (mm)	m_g (g/s)
0	8.0
70	13.3
100	16.6
130	20.7

Table 4.3: Mass flow rates in the jet plume determined from the Gaussian profiles.
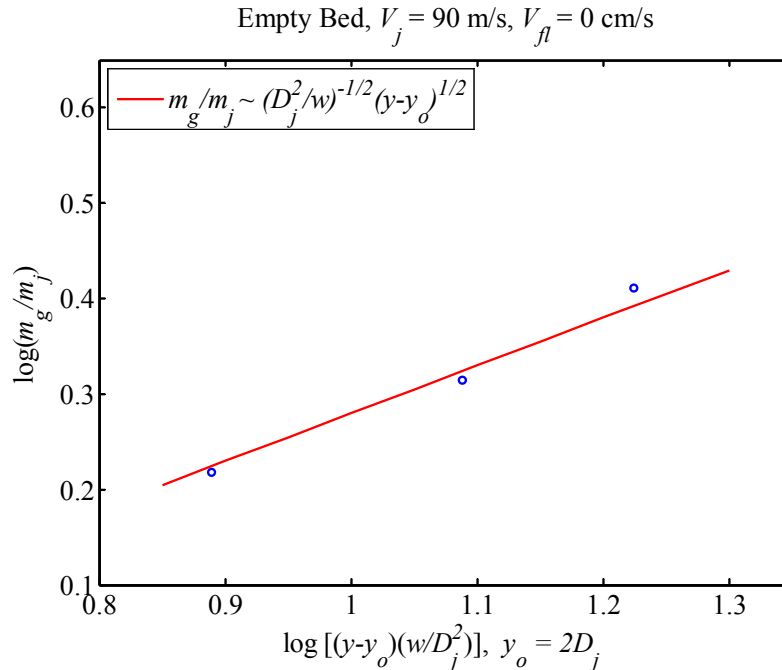
Figure 4.15: Mass flow rate in the jet plume. The experimental data agrees well with the theoretical entrainment.
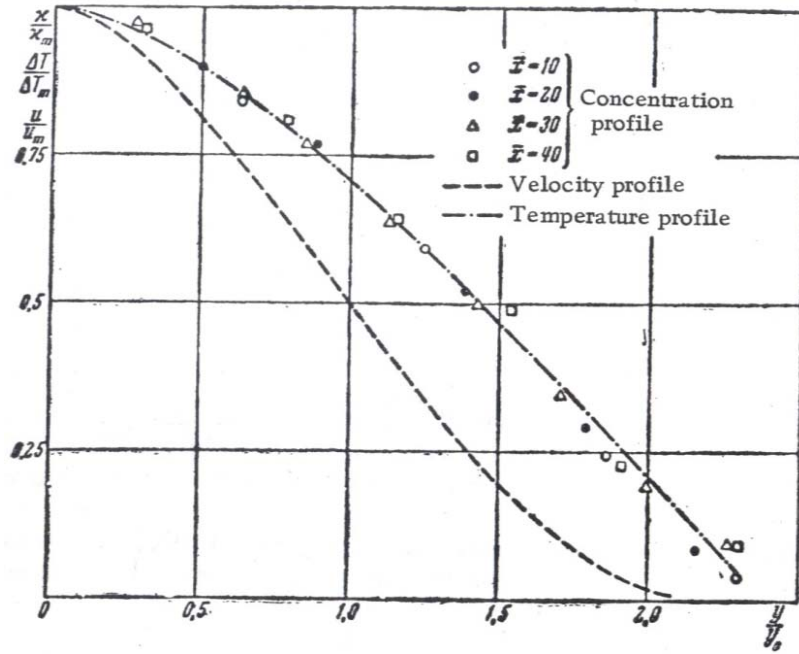
Figure 4.16: Self-similar scalar concentration profiles in a jet plume (Abramovich & Schindel, 1963).

Finally, the mass flow rate of air that originated from the jet nozzle, m_o, was also calculated at each axial location. Since the amount of any passive scalar that originates from the jet inlet is conserved as it is advected downstream by the self-similar gas velocity profile, the nature of the distribution of passive scalars such as concentration are also self-similar and are related to the velocity distribution by the turbulent Schmidt number (Antoine *et al.*, 2001). Figure 4.16 (Abramovich & Schindel, 1963) shows the non-dimensional concentration and velocity profiles, plotted with respect to the half-velocity point. As a result, the dimensionless concentration and velocity are equivalent when they are averaged with respect to mass flow (Abramovich & Schindel, 1963).

$$\frac{C_M}{C_j} = \frac{V_M}{V_j} \tag{4.37}$$

Where the mass averaged concentrations are velocities are

$$C_M = \frac{\int_{-b}^{b} c\rho v \, dx}{\int_{-b}^{b} \rho v \, dx} \tag{4.38}$$

73

$$V_M = \frac{\int_{-b}^{b} \rho_g v_g^2 dx}{\int_{-b}^{b} \rho_g v_g dx} = \frac{J_g}{\dot{m}_g} \qquad (4.39)$$

and C_j and V_j are the average concentration and velocity at the jet inlet. Equation (4.38) refers to the inlet gas concentration ($C_j = 1$) which is being advected at the gas velocity, so that $\rho = \rho_j$ and $v = v_g$. Once again considering the 3D correction factors from Section 4.2, the mass flow rate of gas that originated from the jet inlet (*i.e.* not entrained) is

$$\dot{m}_o = C_1 w \int_{-b}^{b} c \rho_j v_g dx \qquad (4.40)$$

Which by using the definition of the mass averaged concentration can be written as

$$\dot{m}_o = C_1 w C_m \int_{-b}^{b} \rho_j v_g dx \qquad (4.41)$$

and considering $\rho_j = \rho_g$ to be constant yields

$$\dot{m}_o = C_m \left[C_1 \rho_g w \int_{-b}^{b} v_g dx \right] \qquad (4.42)$$

Substituting equations (4.37) and (4.8) for the mass averaged concentration and the mass flow rate

$$\dot{m}_o = \frac{V_m}{V_j} \dot{m}_g \qquad (4.43)$$

and noting that the mass averaged velocity can be written as the ratio of the momentum to mass flow rate, the expression simply reduces to

$$\dot{m}_o = \frac{J_g}{V_j} \qquad (4.44)$$

Therefore, the mass flow rate of the gas that originates from the inlet is directly proportional to the jet momentum, which for the empty bed is constant. The calculated experimental values at the three axial locations are reported in Table 4.4 and agree well with the jet inlet mass flow rate. It should be noted that as the cold jet air entrains the ambient room temperature air, the average density will slightly decrease. This

phenomenon is not accounted for in the integral mass and momentum equations, and could explain the small overestimation of J_g and thus m_o at further downstream.

Physical Location, y (mm)	m_o (g/s)
0	8.0
70	7.8
100	7.9
130	8.4

Table 4.4: Mass flow rates of gas which originates at the jet orifice determined from the Gaussian profiles.

4.4.5 Concluding Remarks

In this chapter, the empty 2D bed has been fully characterized, which in necessary to provide quantitative interpretations of any experimental results. It should be noted that the 3D correction coefficients in Section 4.2 are not universal but rather specific to the geometry of the fluidized bed.   In addition to the overestimation mass flow and momentum rates, it is worth noting that Xuereb (1991) claimed that their 2D jet (case1: D_j = 8 mm, w = 15 cm; case 2: 3 mm x 16.8 mm slot oriented parallel to the bed walls for better entrainment, w = 15 cm) experienced centerline velocity behavior similar to that of a 3D jet, decaying as the inverse of axial distance. Figure 6 of their work is reproduced here as Figure 4.17.   The data fit to the $U_m/U_0 \sim 1/x$ curve is not convincing further downstream. Plotting this data on a log-log plot reveals that their jet expands as the axial distance to the -0.70 power for case 1 and the -0.75 power for case 2, indicating that their jet expansion is initially 3D then confined to two dimensions downstream due to the bed geometry.
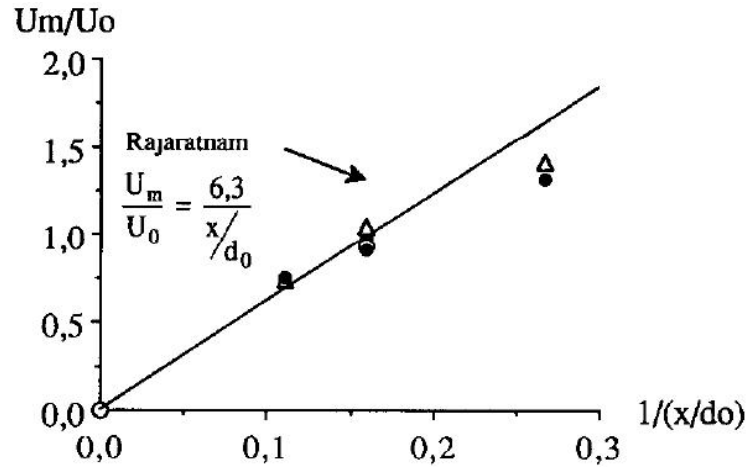
Fig. 6. Décroissance axiale de la vitesse du gaz dans le jet. Cas de la colonne vide.

Figure 4.17: Xuereb (1991) Fig. 6, the axial decay of the centerline velocity of the gas jet in an empty bed. The solid line corresponds to linear velocity decay, which is characteristic of a 3D single-phase jet. The data plotted indicates that for this particular configuration, the jet plume initially experiences 3D growth until it is bounded downstream by the walls where it continues to develop as a 2D jet.

4.5 Chapter 4 References

G. N. Abramovich & L. Schindel. <u>The Theory of Turbulent Jets</u>. The MIT Press (1963).

Y. Antoine, F. Lemoine, M. Lebouche. "Turbulent transport of a passive scalar in a round jet discharging into a co-flowing stream," Eur. J. Mech. B. Fluids. **20** (2), 275-301 (2001)

N. E. Kotsovinos "A note on the spreading rate and virtual origin of a plane turbulent jet," J. Fluid Mech. **77** (2), 305-311 (1976).

G. Horn & M.W. Thring. "Angle of spread of free jets" Nature 1956.

J.M.D. Merry. "Penetration of a horizontal gas jet into a fluidized bed," Trans. Instn. Chem. Engrs. (49) 189-195 (1971).

A. Ounnar, J. Arrar, F. Bentahar. "Hydrodynamic behaviour of upflowing jet in fluidized bed: velocity profiles of sand particles," Chem. Eng. Process. **48** (2), 617-622 (2009)

H. Schlichting. <u>Boundary-Layer Theory, 7th Ed</u>. Translated by J. Kestin. McGraw-Hill (1979)

N.A. Shakhova & G.A. Minaev. "An engineering method of calculating a jet in a fluidized bed," Inzhenerno-Fizicheskii Zhurnal. **19** (6), 1002-1011 (1970).

F.M. White. <u>Viscous Fluid Flow</u>. McGraw-Hill, (2006).

C. Xuereb, C. Laguerie, T. Baron. "Etude du comportement de jets continues horizontaux ou inclines introduits dans un lit fluidise par un gaz Deuxieme partie: profiles de vitesse du gaz dans les jets horizontaux," Powder Tech .**64**, 271-283 (1991)

CHAPTER 5:

BUBBLING BED GAS AND PARTICULATE PHASE VELOCITY PROFILES AND ANALYSIS

Once the vertical jet in the empty bed had been fully characterized, the bed was filled with high density polyethylene (HDPE) microspheres. These particles are considered Geldart Group B particles, which bubble immediately beyond minimum fluidization. In this chapter, gas and particulate phase velocity profiles are presented and analyzed. This includes similarity profile scaling as well as void fraction, mass flow and momentum rate calculations, and particle drag and uncertainty analysis.

As with the empty bed, the jet in the bubbling was run at a volumetric flow rate of 400 SLPM, so that the inlet mass flow rate was maintained at 8.0 g/s. However, the temperature of the jet was maintained slightly warmer (T_j = -5°C) with an air density of 1.317 kg/m^3, resulting in a slightly higher inlet velocity of 92 m/s and inlet momentum of 0.735 kg.m/s^2. The gas and particulate phase velocities were simultaneously recorded according to the jet gas ice crystal seeding and intensity thresholding procedures described in Chapter 3. For this experiment, the emulsion of 838 μm HDPE particles was fluidized at a velocity of 33.4 cm/s. Sequential images (30 FPS) of this jet are shown in Figure 5.1.

Frame 1	Frame 2

Frame 3	Frame 4
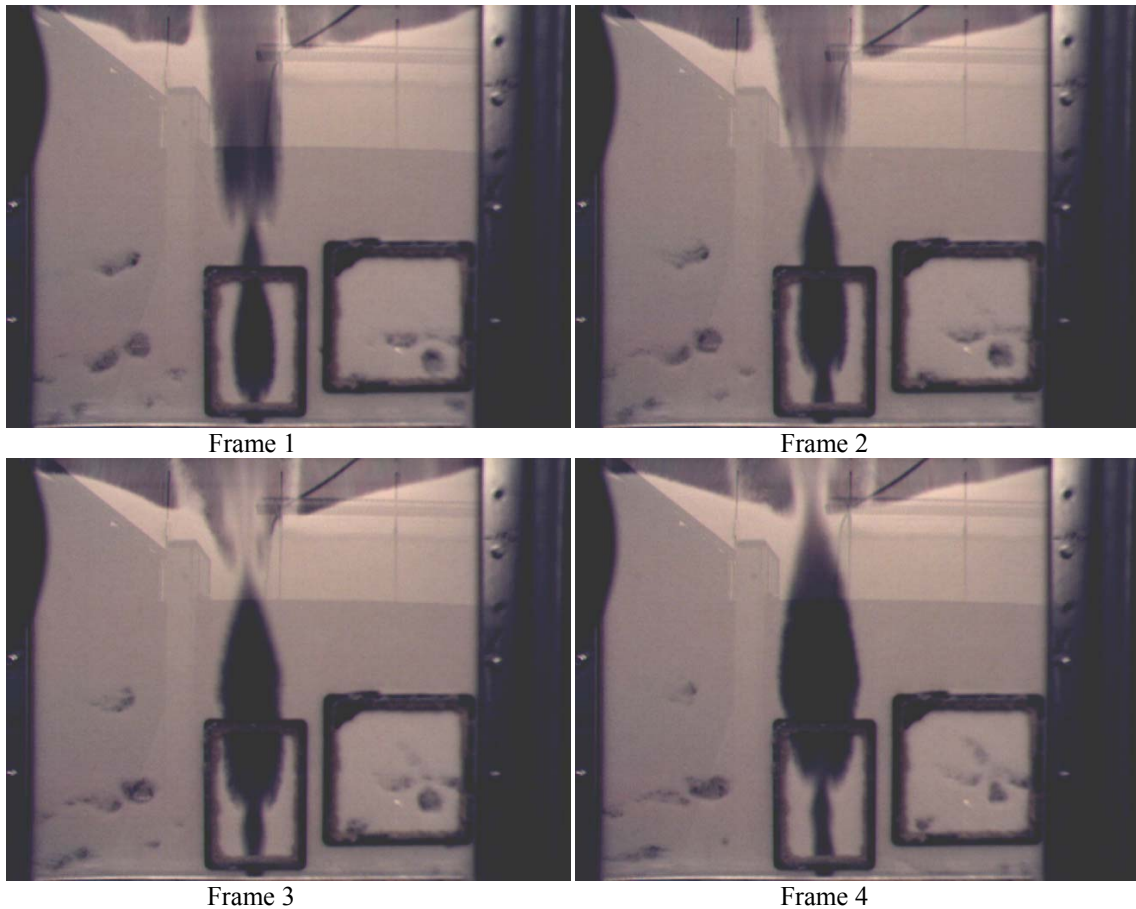
Figure 5.1: Vertical gas jet in the 2D bubbling fluidized bed. The jet inlet velocity is 92 m/s and inlet momentum is 0.735 kg.m/s^2. The emulsion of 838 μm HDPE particles was fluidized at a velocity of 33.4 cm/s, about 15% beyond minimum fluidization. Sequential images captured at 30 FPS.

5.1 HDPE Bed Particle Properties

The solid phase emulsion consisted of HDPE micropellets, which have a density of 900 kg/m^3. These micropellets are slightly cylindrical in shape as they are manufactured *via* an extrusion process. (HDPE microspheres, which are fabricated *via* a polymerization process, are much softer and quickly break down in the bubbling bed.) The particle size distribution, obtained by a laser diffraction technique, is presented in Figure 5.2. The micropellets have a 838 μm Sauter mean diameter (SMD) and 910 μm volume mean diameter (VMD). The VMD is defined as the diameter of a sphere that has the same volume as a particle of interest and SMD is defined as the diameter of a sphere that has the same volume/surface area ratio as a particle of interest.

$$VMD = \left(\frac{6V_p}{\pi}\right)^{1/3} \tag{5.1}$$

$$SMD = 6\left(\frac{V_p}{A_S}\right) \tag{5.2}$$

Here, V_p is the particle volume and A_S is the surface area of the particle. Since the fluidization process involves both the particle effective weight (which acts on the particle volume) and the particle drag (which acts on the particle surface area), the SMD value is used for particle analysis.

The size and density of the HDPE micropellets place them in the Geldart B group, near the D border, so that the emulsion bubbles almost immediately beyond minimum fluidization. Using the dimensionless form of the Ergun equation (1.3) with the coarse particle coefficients, the minimum fluidization velocity of the 838 μm HDPE emulsion is calculated to be 29.6 cm/s, which is very near the experimentally determined value of 29 cm/s. The fluidization and defluidization curves for this emulsion are plotted in Figure 5.3. In order to minimize static charge effects, a pinch of Larostat powder was added to the emulsion and the fluidization air was humidified with a room temperature bubbler.
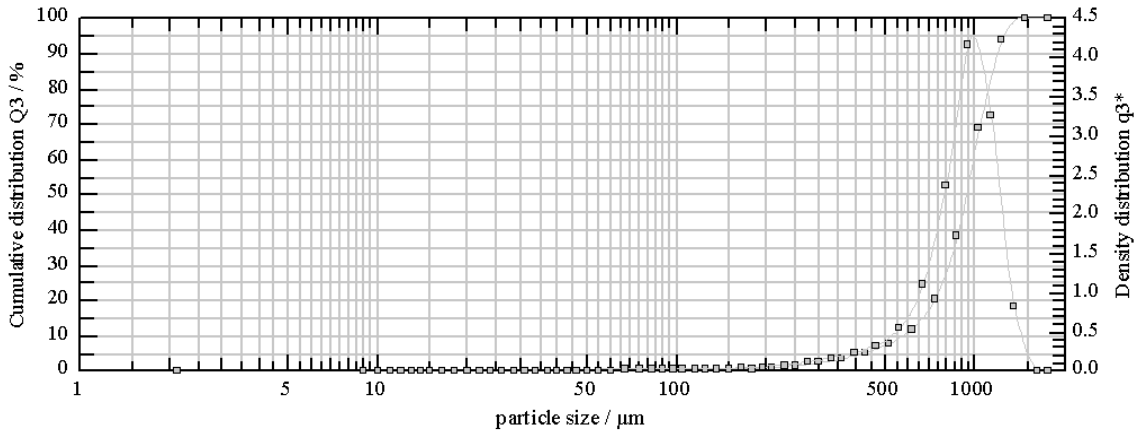
Figure 5.2: Particle size distribution for the HDPE microspheres. Data acquired *via* laser diffraction techniques. SMD = 838 μm, VMD = 910 μm.

80
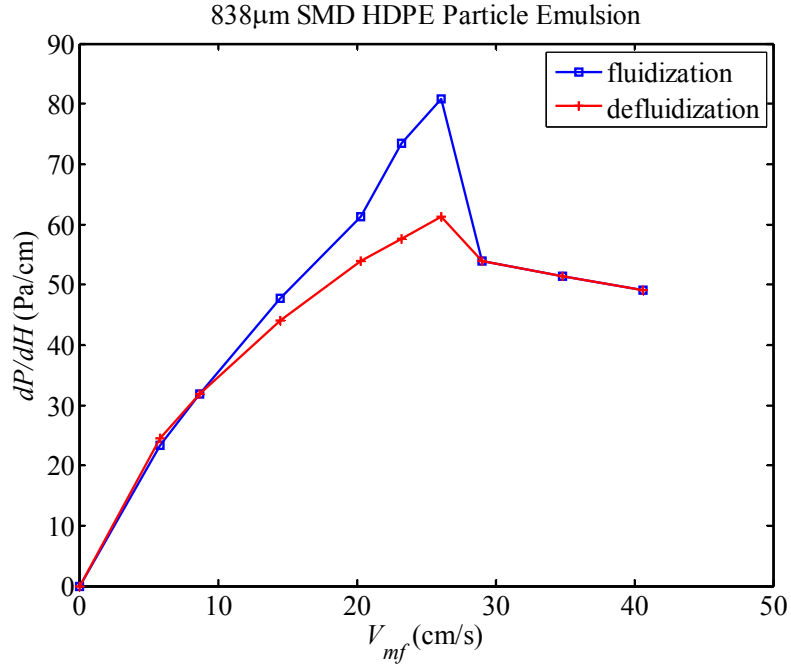
Figure 5.3: Fluidization and defluidization curves for the 838 µm HDPE micropellets. The minimum fluidization velocity was experimentally determined to be 29 cm/s.

5.2 Gas and Particulate Phase Velocity Profiles

The velocity profiles of both the gas and particulate phases taken at axial locations of y = 60 mm, 70 mm, 100 mm, and 130 mm are shown in Figure 5.4 and Figure 5.5. The slip velocity, defined as

$$v_s = v_g - v_p$$

(5.3)

is plotted in Figure 5.6. Next, the particle Reynolds number in the jet plume, defined as

$$\mathrm{Re}_p = \frac{\rho_g \left(v_g - v_p\right)d_p}{\mu_g}$$

(5.4)

is plotted in Figure 5.7.

838 μm HDPE, V_j = 92 m/s, V_{fl} = 33.4 cm/s
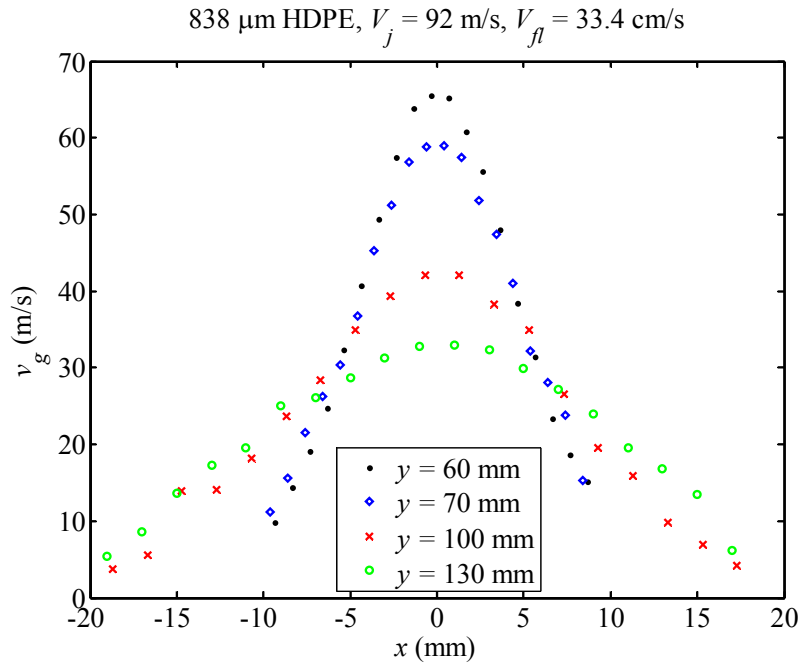
Figure 5.4: Gas phase velocity profiles.

838 μm HDPE, V_j = 92 m/s, V_{fl} = 33.4 cm/s
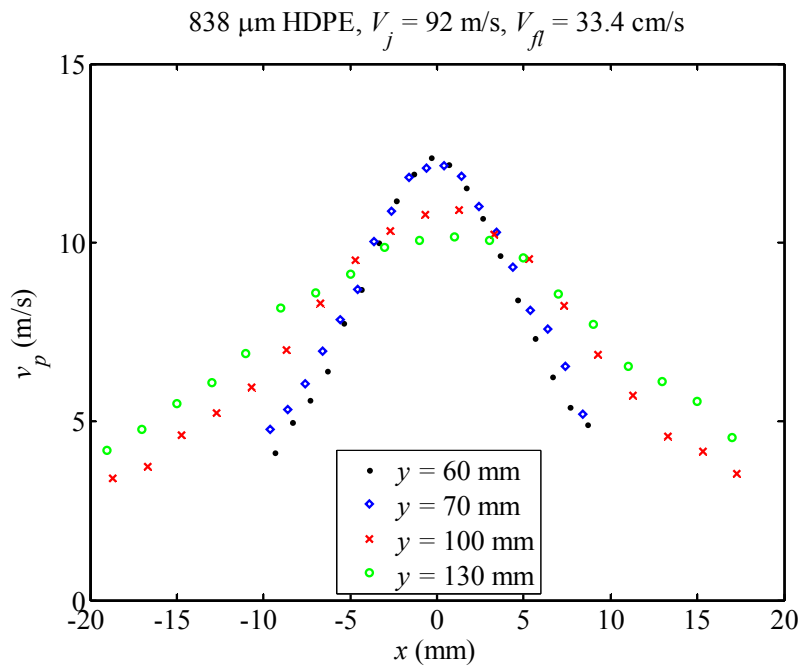
Figure 5.5: Particulate phase velocity profiles.

Figure 5.6: Slip velocity profiles.

Figure 5.7: Particle Reynolds number profiles.
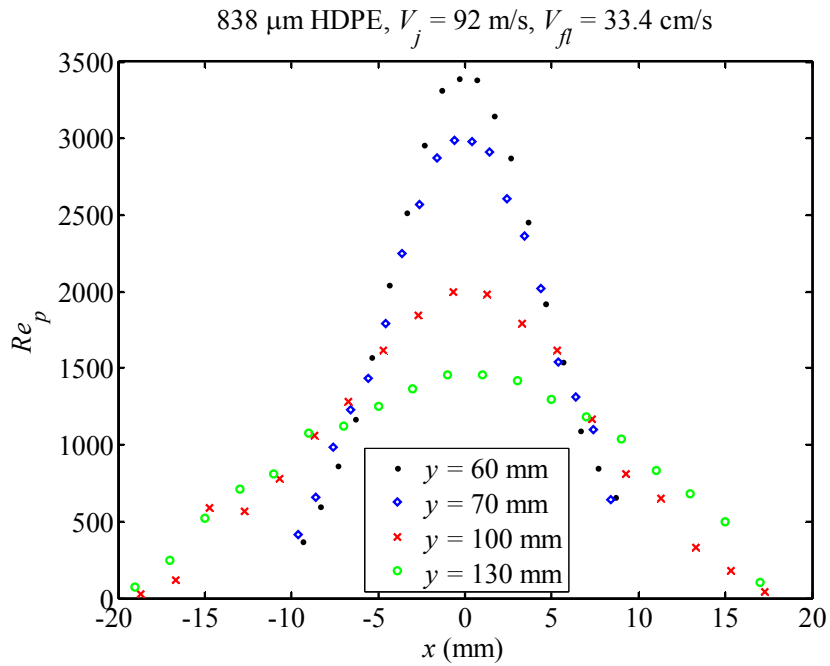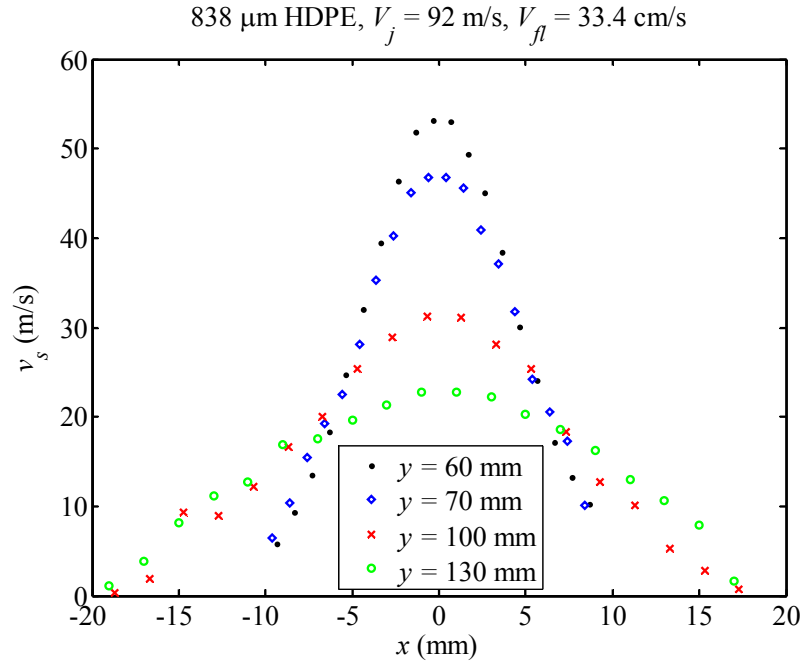
The normalized velocity profiles are then scaled with respect to the empty bed virtual origin (Figure 5.8 and Figure 5.9) and physical origin (Figure 5.10 and Figure 5.11). The data for the two phases does not collapse as well as it did for the single phase gas jet. This is most likely due to the fact that the two-phase jet experiences an unsteady,

non-stationary plume, and the addition of particles may shift the virtual origin and/or each phase may have a unique virtual origin.

In order to circumvent the issue of self-similar virtual origins, the normalized velocity profiles will be scaled with their respective half-velocity points and compared with the Gaussian profile. The gas, particulate, and slip velocity profiles appear to be self-similar when scaled in this manner (Figure 5.13, Figure 5.15, and Figure 5.17). The values of the half velocity points are determined by the slope of the core data when plotted on a semi-log plot, as described in Chapter 4, Section 4.1 (Figure 5.12, Figure 5.14, and Figure 5.16).

The nature of the jet plume spreading and centerline velocity decay is shown in Figure 5.18 through Figure 5.21. The values are juxtaposed with the gas phase of the empty bed at the $y = 70$, 100, and 130 mm axial locations. Since the location of a virtual origin is unresolved for the two-phase jet, no linear curve fits are attempted for the logarithmic plots. However, comparisons can still be made. Figure 5.18 indicates that particulate phase velocity profile is slightly wider that the gas phase velocity profile. This is reasonable since all of the particles in the jet plume are entrained from rest along the emulsion boundary whereas the majority of the gas in the plume originates from the jet orifice. However, the half-velocity point growth for the gas phase in the bubbling and empty bed is remarkably similar. As expected, the presence of particles significantly contributes to the decay of the gas phase velocity, as shown in Figure 5.20 and Figure 5.21. As mentioned in Chapter 3, Section 3, the decline in the measured particulate phase Eulerian velocity is due to the entrainment of relatively stationary particles.

Note that the appearance of self-similarity for the two-phase jet is purely mathematical at this point, as described by equation (4.11), which occurs when profiles assume the same shape when scaled by unique velocity and length factors. Here, the similarity scaling variables are v_m and $x_{1/2}$ for the respective phases. A more physical definition of similarity is discussed by George (1989). Self-preservation implies an equilibrium fluid flow state where all of the dynamical influences evolve at the same rate, *i.e.* it is an asymptotic flow condition achieved once all internal adjustments are complete. Since various length and velocity scales exist for the two phases, the mathematical definition of similarity with respect to the profile half-velocity point is used

84

here for the purpose of comparing profile evolution as well as mass and momentum fluxes. The dependence of v_m and $x_{1/2}$ on the jet and emulsion conditions are investigated in Chapter 6.
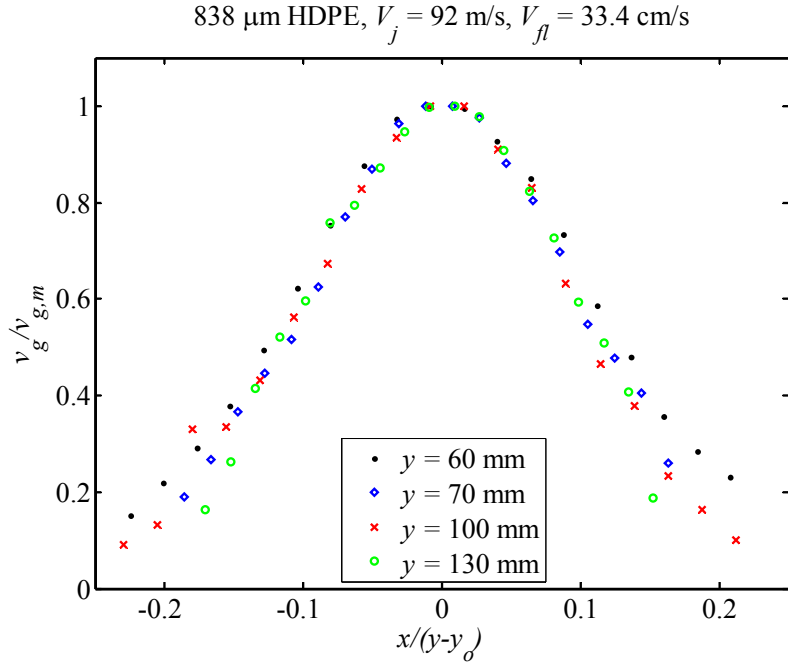
Figure 5.8: Normalized gas phase velocity profiles scaled with respect to the empty bed virtual origin.
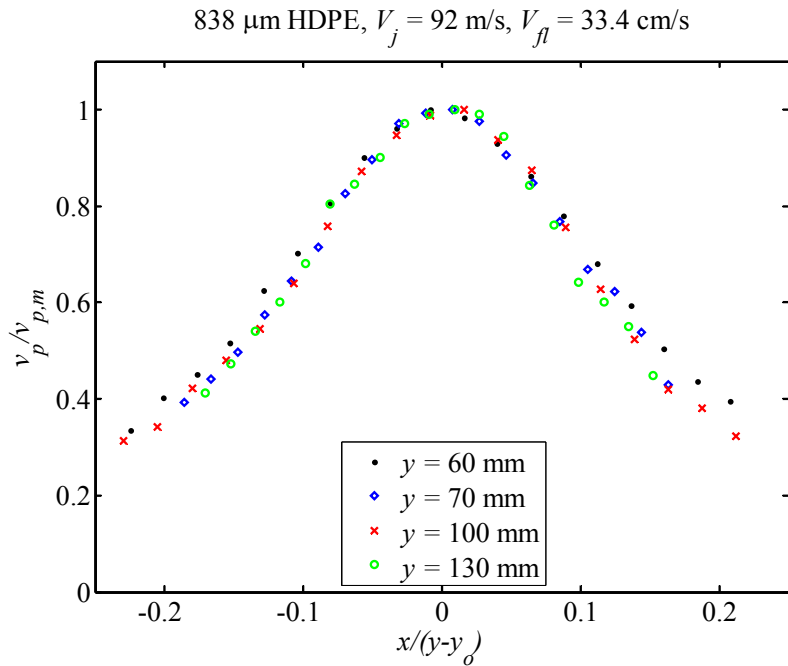
Figure 5.9: Normalized particulate phase velocity profiles scaled with respect to the empty bed virtual origin.

838 μm HDPE, V_j = 92 m/s, V_{fl} = 33.4 cm/s
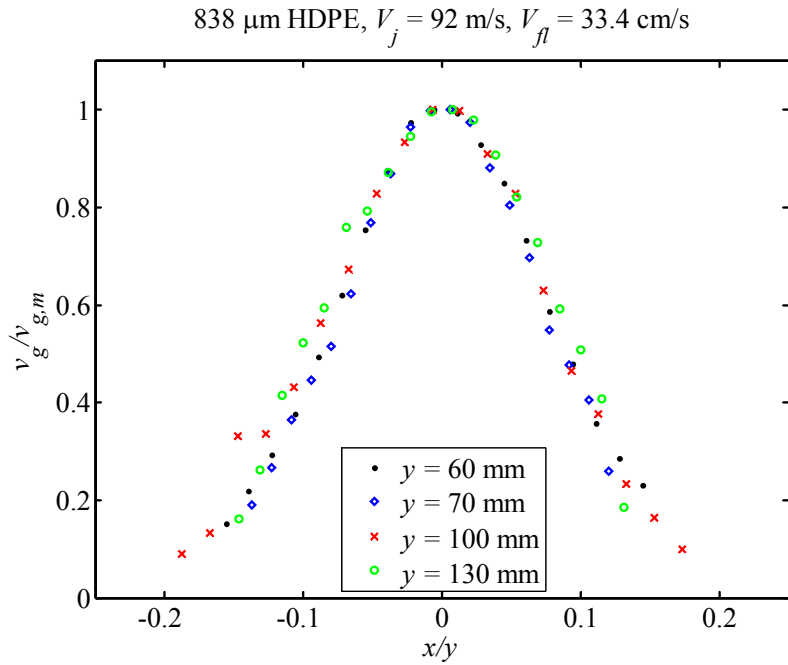
Figure 5.10: Normalized gas phase velocity profiles scaled with respect to the physical origin.

838 μm HDPE, V_j = 92 m/s, V_{fl} = 33.4 cm/s
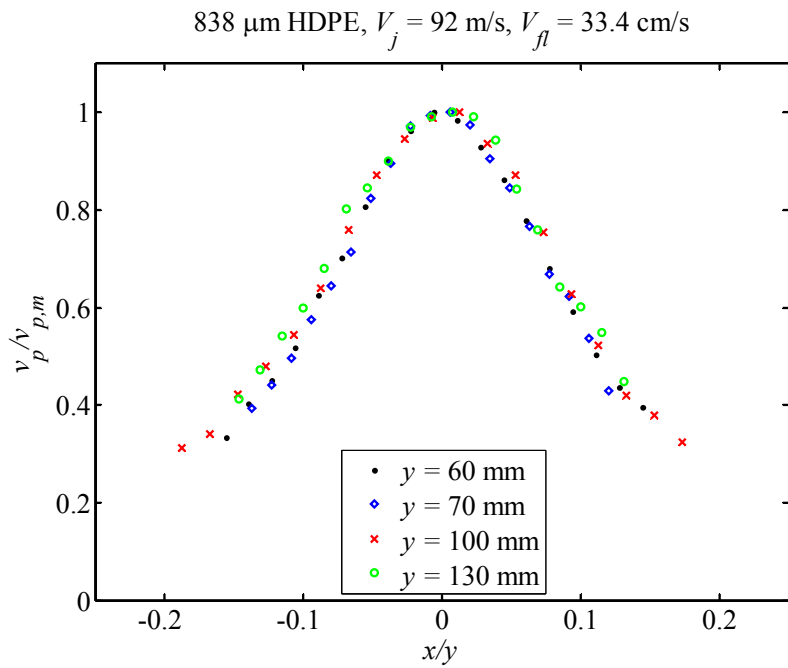
Figure 5.11: Normalized particulate phase velocity profiles scaled with respect to the physical origin.

838 μm HDPE, V_j = 92 m/s, V_{fl} = 33.4 cm/s
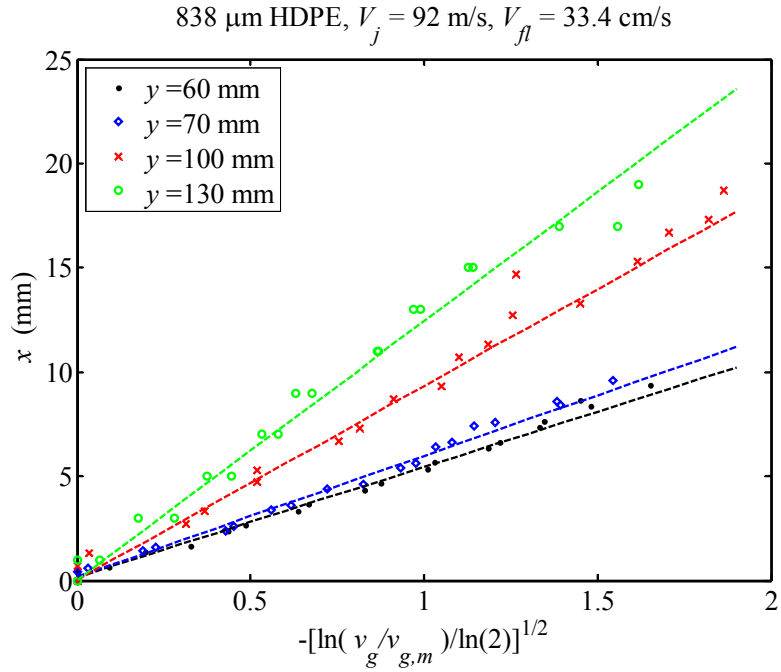
Figure 5.12: Half-velocity point values for gas phase velocity Gaussian profiles are determined from the slope of the core data.

838 μm HDPE, V_j = 92 m/s, V_{fl} = 33.4 cm/s
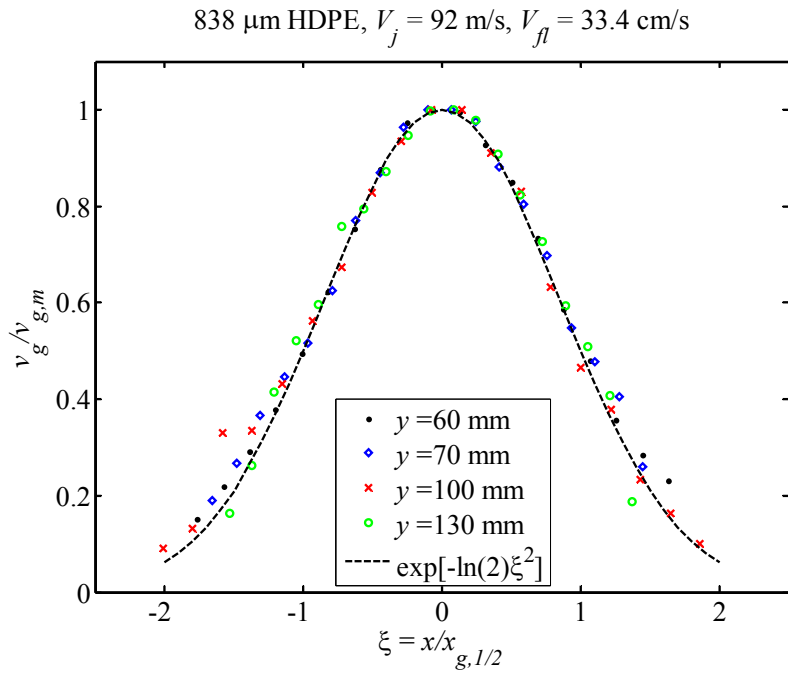
Figure 5.13: Normalized gas phase velocity profiles scaled with respect to the half velocity point.

838 μm HDPE, V_j = 92 m/s, V_{fl} = 33.4 cm/s
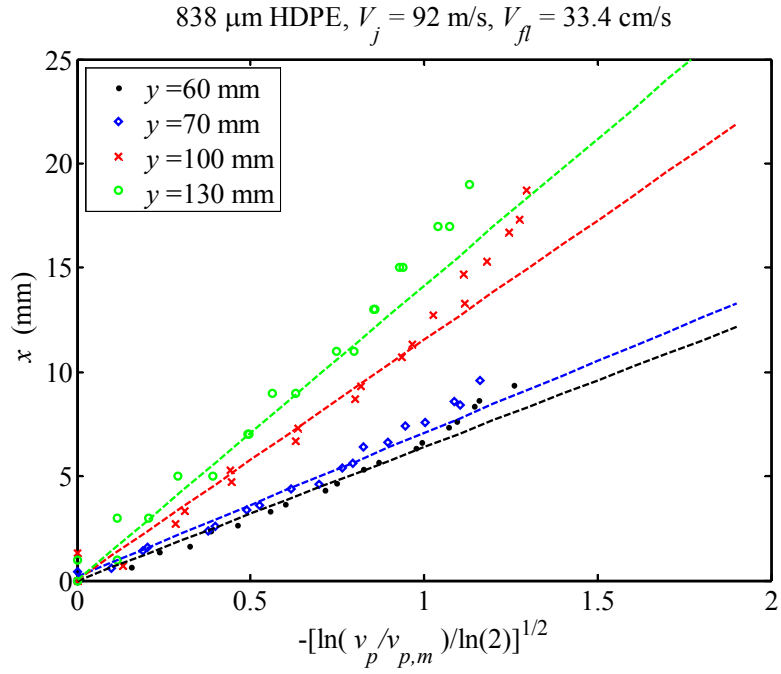
Figure 5.14: Half-velocity point values for particulate phase velocity Gaussian profiles are determined from the slope of the core data.

838 μm HDPE, V_j = 92 m/s, V_{fl} = 33.4 cm/s
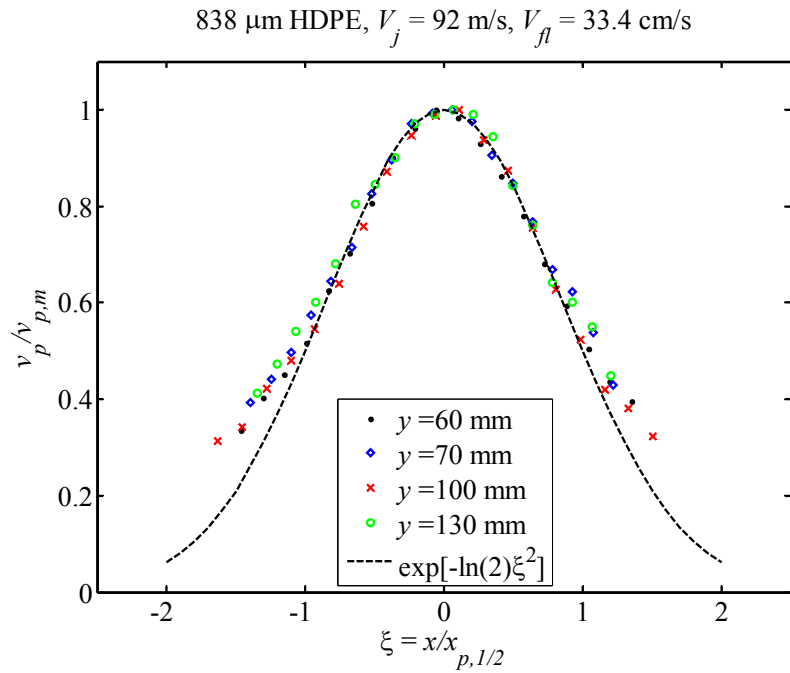
Figure 5.15: Normalized particulate phase velocity profiles scaled with respect to the half velocity point.
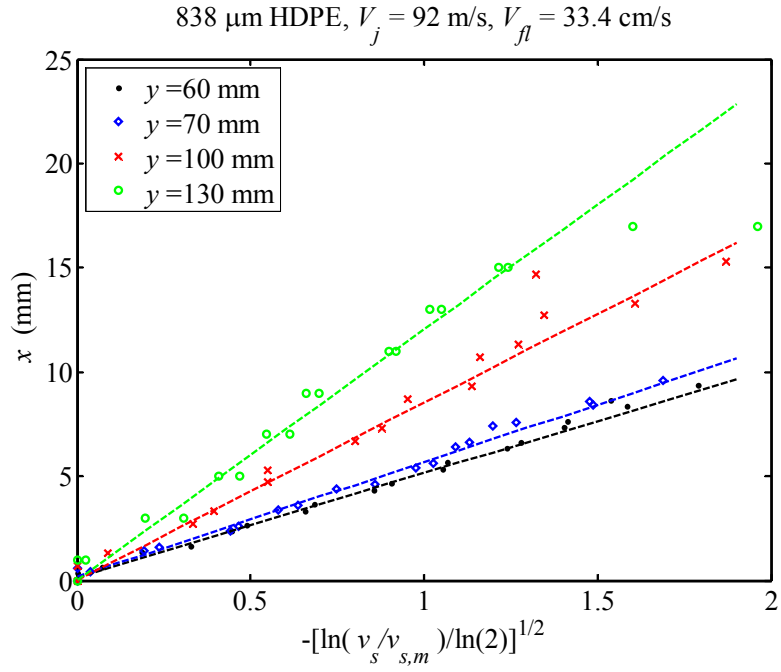
Figure 5.16: Half-velocity point values for slip velocity Gaussian profiles are determined from the slope of the core data.
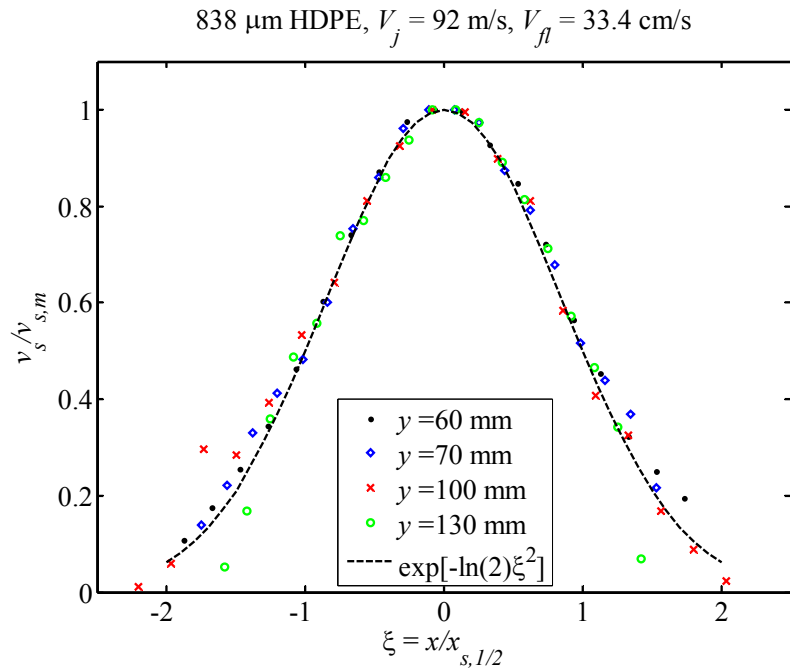
Figure 5.17: Normalized slip velocity profiles scaled with respect to the half velocity point.
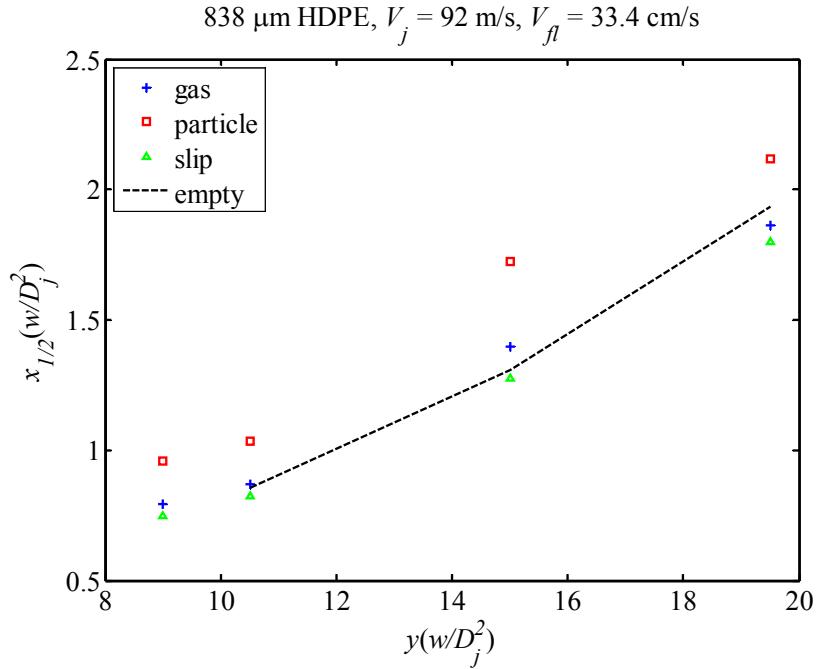
Figure 5.18: Half-velocity point values for the gas, particulate, and slip velocity profiles compared to the empty bed gas phase data.
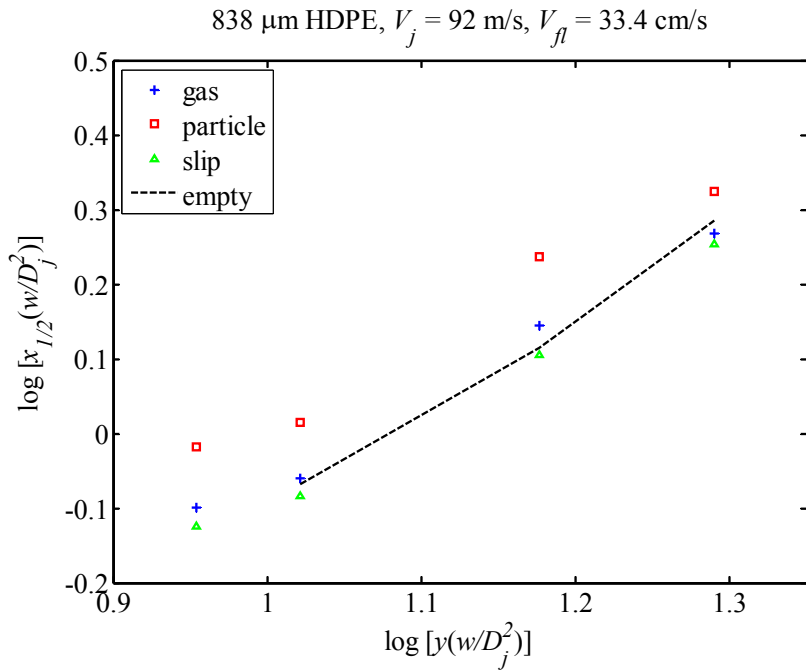
Figure 5.19: Axial spreading of the gas, particulate, and slip velocity profiles compared to the empty bed gas phase data.

838 μm HDPE, V_j = 92 m/s, V_{fl} = 33.4 cm/s
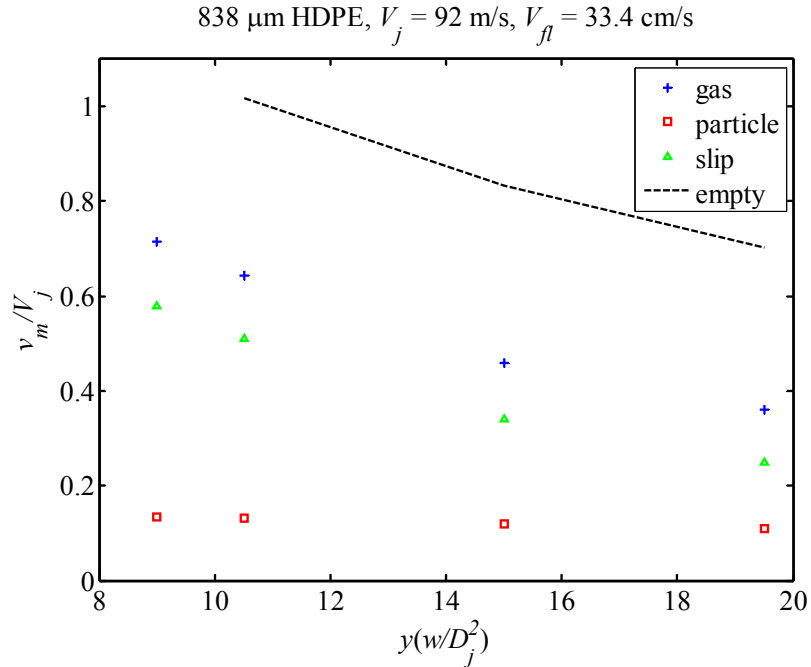
Figure 5.20: Maximum velocity values for the gas, particulate, and slip velocity profiles compared to the empty bed gas phase data.

838 μm HDPE, V_j = 92 m/s, V_{fl} = 33.4 cm/s
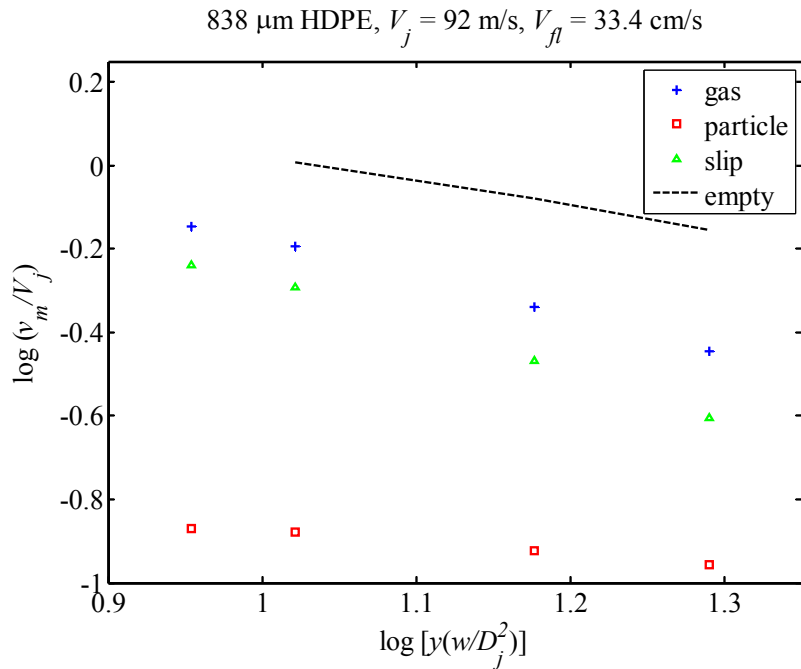
Figure 5.21: Axial decay of the centerline velocities for the gas, particulate, and slip velocity profiles compared to the empty bed gas phase data.

The vertical jet in the emulsion of particles has a tendency to slightly sway back and forth over a period of a few seconds. This periodic swaying has a greater effect on the downstream measurement locations, as it tends to broaden the recorded velocity

profiles (overestimates $x_{1/2}$ and underestimates v_m). Figure 5.22 indicates that the period of the plume sway is approximately 5 to 10 seconds, which is in agreement with the video images. (Note that the velocity time traces presented in Figure 5.22 are exemplary of the temporal coincidence of the simultaneous gas and particulate phase velocity measurements). The sampling period of 120 seconds at each location is long enough to ensure that the reported velocity profiles are adequately temporally averaged, and can thus be used for mass and momentum calculations. The frequency of this swaying motion seems to be dictated by the particle dynamics in the freeboard region as particles descend along the edges back onto the upper surface of the emulsion, causing particle avalanches to occur once the angle of repose is exceeded. A particle cyclone and feedback system would help minimize this phenomenon.

In addition to swaying, the jet plume also pulsates as waves of particles propagate along the plume boundaries, as seen in the jet images. This fluctuation will broaden out the measured particle velocity profiles by overestimating average values in the wavy region. When a dense structure of slower moving particles propagates upwards along the boundary, one or more of the LDV beams is blocked and therefore no velocity is recorded. Hence, only higher particle velocities are recorded when the region is temporarily dilute and thus the average recorded velocity is slightly overestimated near the plume boundary. However, this deviation is not critical since the majority of the jet mass and momentum are transported in the core region of the plume. This effect as not as noticeable for the gas phase because the void fraction is low when the LDV beams are blocked by a passing wave of particles. This explains why the normalized velocity profiles show that the gas phase data agrees well with the Gaussian profile across the span of the plume whereas the particulate data exhibits a stronger deviation beyond the half-velocity point.
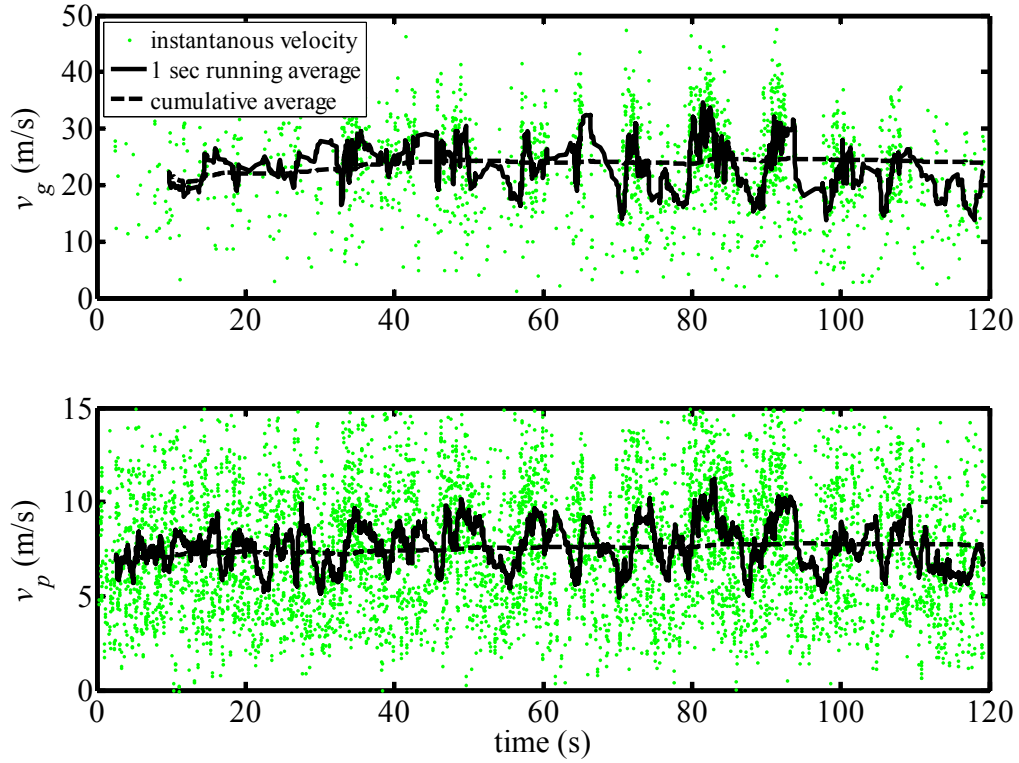
Figure 5.22: Time trace of simultaneous LDV gas and particulate phase velocity measurements at $y = 130$ mm, $x = 10$ mm. 1,938 bursts were recorded for the gas phase and 6,231 bursts for the particulate phase over the recording period of 120 s.

5.3 Void Fraction

An average void fraction at various axial locations can be determined by a momentum balance with the jet inlet momentum. Since momentum is transferred from the jet gas to the entrained particles downstream

$$\dot{J}_j = \dot{J}_g + \dot{J}_p$$

(5.5)

Writing the momentum fluxes in terms of the velocity profiles and volumetric void fraction, ε

$$\dot{J}_j = wC_2\left[\int_{-b}^{b} \varepsilon \rho_g v_g^2 dx + \int_{-b}^{b}(1-\varepsilon)\rho_p v_p^2 dx\right]$$

(5.6)

The densities of the gas and particulate phases are considered to be constant. The phase concentration is considered to be uniform across the jet so that $\varepsilon = \varepsilon(y)$ as particles are

93

entrained and the jet expands. This is consistent with the hydrodynamic model of Massimilla in Davidson *et al*. (1985).

$$\varepsilon = \frac{\dot{J}_j - wC_2 \int\limits_{-b}^{b} \rho_p v_p^2 dx}{wC_2 \left[\int\limits_{-b}^{b} \rho_g v_g^2 dx - \int\limits_{-b}^{b} \rho_p v_p^2 dx \right]} \tag{5.7}$$

Using equation (4.32) to carry out the integration of the self-similar velocity profiles, the momentum averaged volumetric void fraction at each axial location is shown in Figure 5.23. As expected, the jet plume is very dilute with an average gas volume fraction of only about 95 to 96%. Since the average value of the void fraction is high and experiences only a small change, ε could be considered constant for gas phase mass and momentum calculations in this particular case.

On the other hand, the volumetric solids fraction (*1-ε*) cannot be considered constant for the particulate mass and momentum calculations. This is because the value of *1-ε* is very small, and therefore even the small change in solids fraction in the streamwise direction is significant. Furthermore, the density of the particles is about three orders of magnitude greater than the gas. The calculated values suggest that, perhaps contrary to intuition, the solids fraction actually decreases in the streamwise direction shortly beyond the jet orifice. However, this is consistent with the work of Merry (1971) and Xuereb *et al.* (1991), who defined an initial entrainment zone followed by a linear expansion region where the particle entrainment rate gradually decreases.
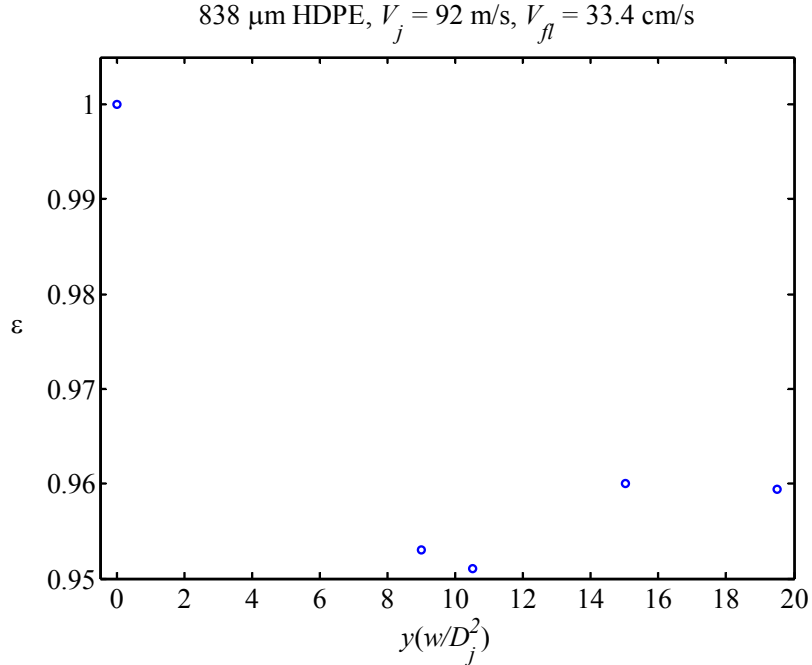
Figure 5.23: Void fraction values determined from a momentum balance at each axial location with the jet inlet using equation (5.7).

5.4 Mass Flow and Momentum Rates

The mass flow and momentum rates for the two phases can be calculated at each downstream location assuming that the densities and void fraction are constant across the profile according to

$$\dot{m}_g = \varepsilon\, C_1 \rho_g w \int_{-b}^{b} v_g\, dx$$

(5.8)

$$\dot{m}_p = (1-\varepsilon)\, C_1 \rho_p w \int_{-b}^{b} v_p\, dx$$

(5.9)

$$\dot{J}_g = \varepsilon\, C_2 \rho_g w \int_{-b}^{b} v_g^2\, dx$$

(5.10)

$$\dot{J}_p = (1-\varepsilon)\, C_2 \rho_p w \int_{-b}^{b} v_p^2\, dx$$

(5.11)

Once again, using equation (4.32) and (4.35) to carry out the integrations of the self-similar velocity profiles, the mass flow and momentum rates can be obtained with knowledge of the respective maximum velocity, half-velocity point, and volumetric void and solids fractions as a function of axial location, so that

95

$$\dot{m}_g = 2.09\, C_1 \varepsilon \rho_g\, w\!\left(v_{g,m} x_{g,1/2}\right)$$

(5.12)

$$\dot{m}_p = 2.09\, C_1 (1-\varepsilon) \rho_p\, w\!\left(v_{p,m} x_{p,1/2}\right)$$

(5.13)

$$\dot{J}_g = 1.5\, C_2 \varepsilon \rho_g\, w\!\left(v_{g,m}^2 x_{g,1/2}\right)$$

(5.14)

$$\dot{J}_p = 1.5\, C_2 (1-\varepsilon) \rho_p\, w\!\left(v_{p,m}^2 x_{p,1/2}\right)$$

(5.15)

Using experimental values for these variables, the calculated mass flow and momentum rates for both phases are plotted with respect to the physical origin in Figure 5.24 and Figure 5.26. Logarithmic plots of the downstream values (Figure 5.25 and Figure 5.27) reveal how the gas and particulate phase mass and momentum vary in the streamwise direction with respect to the physical origin. The mass flow rates are juxtaposed with the empty bed gas phase data. Recall that the momentum rate for the gas phase in the empty bed remains constant at the inlet value, and is therefore not shown in the figures.

The mass flow data indicates that particle entrainment near the jet inlet is significant and that the rate of entrainment into the jet plume decreases with streamwise distance. Once again, this is consistent with an initial entrainment zone followed by a linear expansion region where the particle entrainment rate gradually decreases. On the other hand, the gas phase mass flow in the jet plume remains nearly constant at the inlet value. The momentum data indicates that more than half of the initial jet gas momentum is already transferred to the particulate phase at first axial measurement location. Significant initial momentum transfer is to be expected due to high particle entrainment and large relative slip velocity values near the jet inlet.

Note that the 3D correction coefficients calculated for the empty bed are used to calculate the mass and momentum flow rates for both phases. If the 3D correction factor is neglected in equation (5.7), the volumetric void fraction becomes overestimated and therefore the amount of momentum transfer from the gas to the particulate phase in the jet plume would be underestimated. Likewise, the calculated gas phase mass fluxes would be unrealistically large, as noted by Xuereb *et al.* (1991).
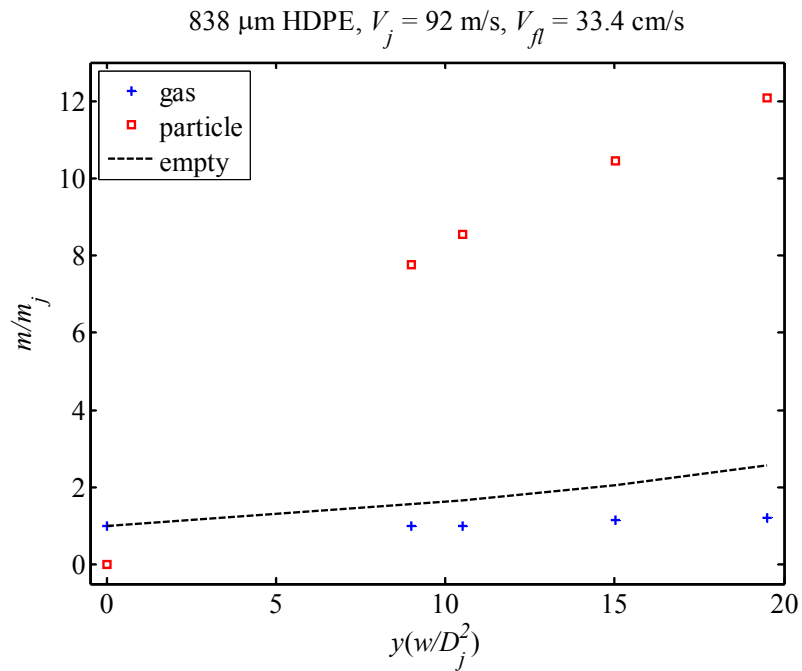
Figure 5.24: Gas and particulate phase mass flow rates in the jet plume determined from the Gaussian profiles and calculated void fractions. The two-phase data is compared to the empty bed gas phase data.
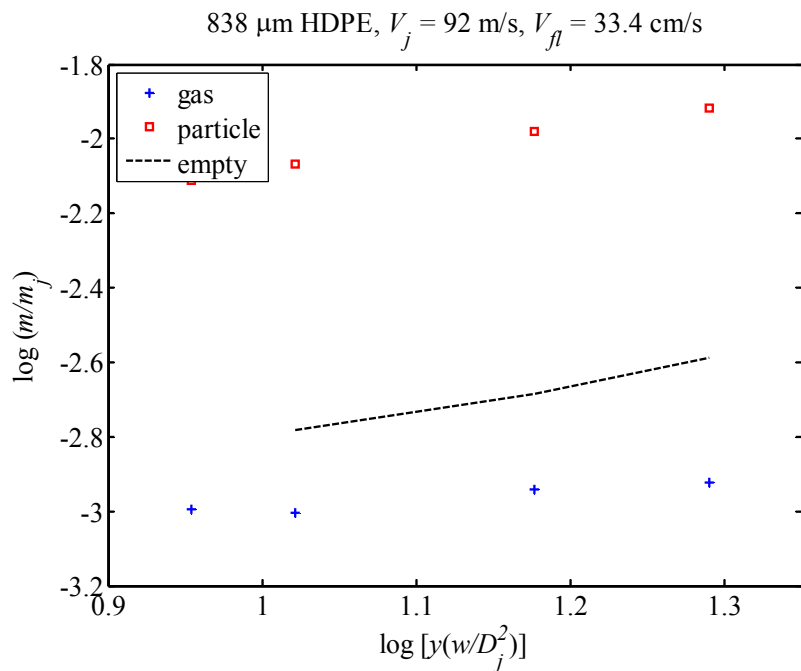
Figure 5.25: Axial growth of the gas and particulate phase mass flow rates. The two-phase data is compared to the empty bed gas phase data.
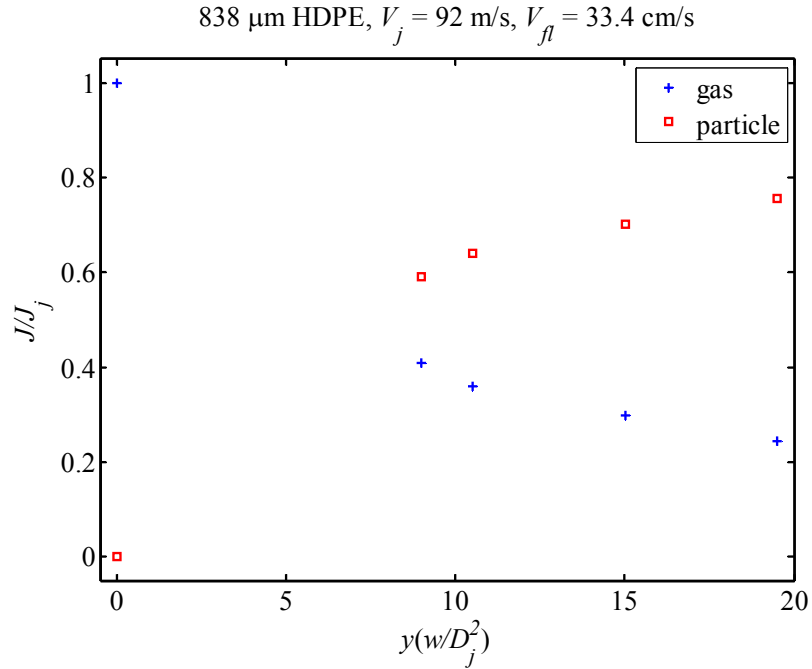
Figure 5.26: Gas and particulate phase momentum rates in the jet plume determined from the Gaussian profiles and calculated void fractions. The empty bed gas phase momentum rate remains constant at the inlet value.
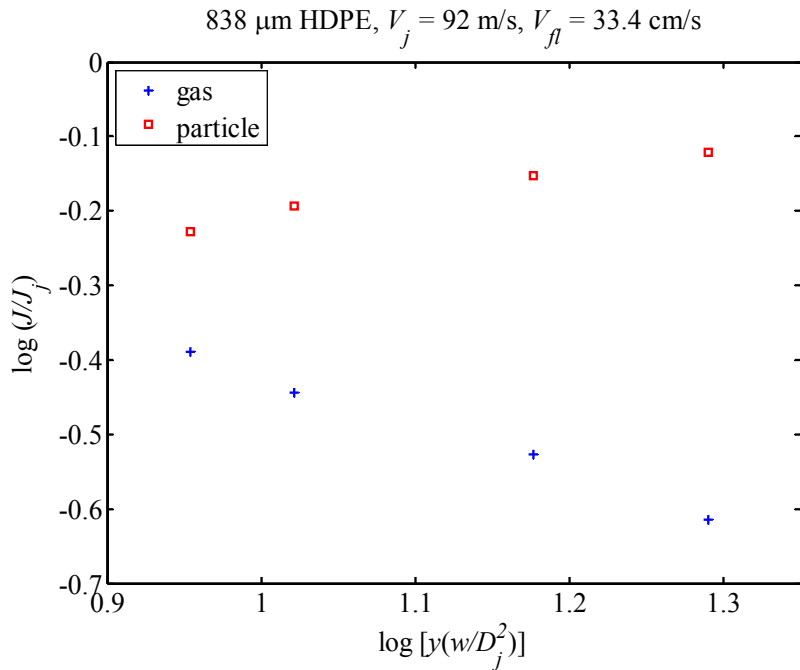
Figure 5.27: Axial development of the gas and particulate phase momentum rates. The empty bed gas phase momentum rate remains constant at the inlet value.

5.5 Bed Particle Coefficient of Drag

Momentum is transferred from the jet gas to the entrained particles *via* drag force. The drag force on a particle in a gas flow is

$$F_D = \frac{1}{2} C_D A_p \rho_g \left(v_g - v_p \right)^2$$

(5.16)

which is positive in the upwards vertical direction since the coefficient of drag (C_D) is a positive value and $v_g > v_p$ everywhere in the jet plume. Note that A_P is the projected area (circular cross-section) of the particle, as opposed to the surface area of the particle. The equation of motion for an individual particle is

$$F_D - W_p = m_P \frac{dv_p}{dt}$$

(5.17)

Since $\rho_p >> \rho_g$, acceleration terms (added mass and Basset force) have been neglected. Applying the chain rule to express acceleration in terms of the spatial derivative,

$$F_D - W_p = m_P v_p \frac{dv_p}{dy}$$

(5.18)

Equation (5.18) indicates that as long as $F_D > W_p$, an individual particle's velocity will increase in the streamwise direction. Figure 5.7 indicates that the particle Reynolds number in the plume is greater than 1,000 for all locations near the jet centerline. Figure 5.28 shows that at these high Reynolds numbers, the coefficient of drag on a sphere has a nearly constant value of 0.4. Therefore, the drag force on an individual 838 μm HDPE particle in the jet core is about 50,000 times greater than the weight force due to gravity. However, Figure 5.21 indicates that v_p decreases in the streamwise direction. As briefly discussed in Chapter 3, Section 3, the reason for this inconsistency is due to the different frames of reference.

The particle velocity in the equation of motion for an individual particle is taken in the Lagrangian frame of reference. On the other hand, the LDV system records the velocity of particles passing though a specified location, rather than tracking the velocity of a specific particle. These velocity measurement values are with respect to the Eulerian frame of reference, which treats the particulate phase as a continuum. To clarify, the velocity of an individual particle does increase as it is accelerated downstream by the vertical drag force of the jet gas (Lagrangian frame). However, the average particle

velocity decreases with downstream distance since several slow moving particles are entrained along the jet boundaries (Eulerian frame).
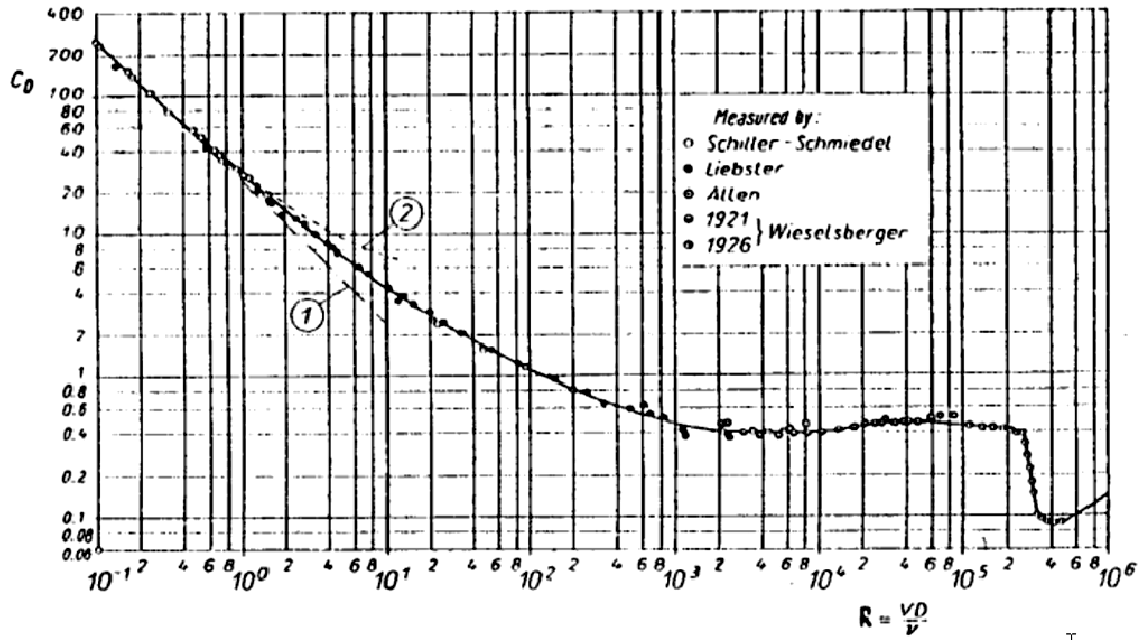
Figure 5.28: Drag coefficient for a sphere as a function of the Reynolds number (Schlichting, 1979). From Figure 5.7, the particle Reynolds number in the jet core is greater than 1,000, predicting a nearly constant drag coefficient of 0.4.

Considering the jet to be steady state, the Eulerian equation of motion per unit bed width for a differential area (Δx by Δy) of the particulate phase is

$$\left. \dot{J}_p \right|_y - \left. \dot{J}_p \right|_{y+\Delta y} + f_D - w_p = 0$$

(5.19)

where the drag and weight forces are

$$f_D = N_p F_D = (1-\varepsilon)\frac{\Delta x \Delta y}{V_p} F_D$$

(5.20)

$$w_p = (1-\varepsilon)\rho_p g \Delta x \Delta y$$

(5.21)

where V_p is the volume of an individual particle. The momentum flux is

$$\dot{J}_p = (1-\varepsilon)\rho_p v_p^2 \Delta x$$

(5.22)

Substituting equations (5.20) - (5.22), (5.16), and (5.3) into (5.19) and taking the limit as Δx and Δy go to zero

100

$$(1-\varepsilon)\left(\frac{C_D A_p \rho_g}{2V_p}\right)v_s^2 dx - (1-\varepsilon)\rho_p g dx = \rho_p \frac{d}{dy}\left[(1-\varepsilon)v_p^2\right]dx \tag{5.23}$$

Multiplying through by dy and integrating dx from $-b$ to b and dy from y_1 to y_2 and considering $(1-\varepsilon)$ to be a function of y only yields

$$\left(\frac{C_D A_p \rho_g}{2V_p}\right)\int_{y_1}^{y_2}\left[(1-\varepsilon)\int_{-b}^{b}v_s^2 dx\right]dy - 2\rho_p g\int_{y_1}^{y_2}(1-\varepsilon)b dy$$

$$= \rho_p \int_{-b}^{b}\left\{\left[(1-\varepsilon)v_p^2\right]_{y_2} - \left[(1-\varepsilon)v_p^2\right]_{y_1}\right\}dx \tag{5.24}$$

Expressing the velocity profiles in the similarity form of $v(x,y) = v_m(y)f(\xi)$, where $\xi = x/x_{1/2}$,

$$\left(\frac{C_D A_p \rho_g}{2V_p \rho_p}\right)\int_{y_1}^{y_2}\left[(1-\varepsilon)v_{s,m}^2\int_{-b}^{b}f_s^2(\xi)dx\right]dy - 2g\int_{y_1}^{y_2}(1-\varepsilon)b dy$$

$$= \left[(1-\varepsilon)v_{p,m}^2\right]_{y_2}\int_{-b}^{b}\left[f_p^2(\xi)\right]_{y_2}dx - \left[(1-\varepsilon)v_{p,m}^2\right]_{y_1}\int_{-b}^{b}\left[f_p^2(\xi)\right]_{y_1}dx \tag{5.25}$$

Changing variables in order to carry out the velocity profile integrations

$$\int_{-b}^{b}f^2(\xi)dx = x_{1/2}\int_{-2}^{2}f^2(\xi)d\xi \tag{5.26}$$

When the Gaussian velocity profile is used, equation (4.32) can be used to carry out the integration

$$\int_{-b}^{b}f^2(\xi)dx = 1.5\,x_{1/2} \tag{5.27}$$

If the weight of the particle is negligible, knowledge of the shape of the self-similar profile is not necessary, only the fact that

$$\int_{-b}^{b}f^2(\xi)dx = x_{1/2}\int_{-2}^{2}f^2(\xi)d\xi = (const)x_{1/2} \tag{5.28}$$

is needed as the constant would cancel from both sides of equation (5.25) if gravity is neglected. However, the particle weight is considered in this general formulation. Also expressing $b = 2x_{1/2}$, the coefficient of drag can be solved by re-arranging equation (5.25)

$$C_D = \left(\frac{2V_p\rho_p}{A_p\rho_g}\right)\frac{4g\int_{y1}^{y2}(1-\varepsilon)x_{p,1/2}dy + 1.5\left\{\left[(1-\varepsilon)v_{p,m}^2 x_{p,1/2}\right]_{y2} - \left[(1-\varepsilon)v_{p,m}^2 x_{p,1/2}\right]_{y1}\right\}}{1.5\int_{y1}^{y2}(1-\varepsilon)v_{s,m}^2 x_{s,1/2}dy}$$ (5.29)

The integrals in equation (5.29) can either be carried out numerically with experimental values of v_m^2 and $x_{1/2}$ for the particulate and slip velocity profiles at the various axial locations or by analytically integrating the expressions for v_m^2 and $x_{1/2}$ as a function of y if they are known. The former was chosen and the results are shown in Table 5.1. The reasonable agreement between these values and Figure 5.28 indicates that gas-particle drag is the dominant mechanism of momentum transfer and that particle-particle collisions are not significant in the plume. The discrepancy between the values in Table 5.1 is primarily due to the uncertainty in (1-ε). Furthermore, the bed particle microspheres are slightly cylindrical in shape, and therefore this analysis can only serve as a first order approximation.

Physical Distance, y_2-y_1 (mm)	C_D
60-70	0.47
70-100	0.29
100-130	0.40

Table 5.1: Particle drag coefficients calculated from equation (5.29). The established empirical value is approximately 0.4. The HDPE micropellets are treated as spheres and the particulate phase and slip velocity Gaussian profiles as well as the calculated solids fraction values are used. The major source of error is the uncertainty of the solids volume fraction at each axial location.

5.6 Uncertainty and Repeatability

The jet in the bubbling bed was run twice more at the same conditions as in the prior section. In addition, an experiment was carried out with a non-seeded jet ($T_j = 15^{\circ}C$) at the same inlet momentum ($J_j = 0.735$ kg.m/s^2) in order to determine if there are any unforeseen effects of the colder ice crystal seeded jet gas. Furthermore, the bed particle Doppler bursts from this run were processed with and without the subranging procedure described in Chapter 3, to examine the effects of this data subranging technique.

In a single-phase free turbulent jet, the only inlet parameter that matters is the initial jet momentum (White, 2006) so that

$$v_{g,m} = (const)\left(\frac{J_j}{\rho_g}\right)^{1/2}(y - y_o)^{-1/2}$$

(5.30)

Considering the gas-particle interaction in the jet plume, the drag force on the entrained particles near the jet inlet can be approximated as

$$F_D = \frac{1}{2}C_D A_p \rho_j V_j^2$$

(5.31)

Written in terms of the jet inlet momentum

$$F_D = \frac{1}{2}C_D \frac{A_p}{A_j}J_j$$

(5.32)

Therefore, at high particle Reynolds numbers, where C_D is nearly constant, the mechanism of momentum exchange between the jet gas and the entrained particles scales with the initial jet momentum.

The particulate phase velocity profiles at the various axial locations for the three seeded jet runs as well as the subranged and non-subranged, non-seeded jet run is shown in Figure 5.29 through Figure 5.32. These profiles are very similar at the $y = 60$ mm and 70 mm locations and tend to deviate more at the downstream locations. The same trend is seen in the gas phase velocity profiles (Figure 5.33 through Figure 5.36). This is due to 1) the swaying and pulsating nature of the jet, as discussed prior, and 2) the decreased burst data count outside the jet core.

As discussed in section 5.2 in order to obtain stable mean statistics in the jet core, LDV data was acquired at each location for a duration of 120 seconds. Yanta & Smith (1973), suggest that "an ensemble of 1,000 points at 95% confidence will have 0.3% and 4.4% random error in the mean and fluctuating velocity measurements, respectively". Typical data counts in for both the gas and particulate phases in the core region is approximately 5,000 to 10,000 bursts. Towards the jet plume boundary, the particulate phase counts drop to about 2,000 bursts and gas phase counts to only about 200 bursts. The lower gas phase data count in the boundary region occurs because the interstitial fluidization gas is not seeded with ice crystals. Near the jet plume boundary, the data sample size for neither phase is adequate to obtain statically stable mean values. As

shown in Figure 5.37, approximately 400 gas phase bursts and 4,500 particulate phase bursts are needed to asymptotically reach reasonably stable mean velocity values. Beyond this point longer time scale variations, such as bed turnover, are responsible for slight mean velocity value fluctuations. The particulate phase requires more burst counts due to particle entrainment and variation in particle shape, size, and surface characteristics.

The non-seeded runs indicate that subranging has no noticeable effect on the particulate phase velocity values in the jet core. However, the subranged bed particle data velocity values are typically slightly higher than the raw values near the plume boundaries. This is because the particulate phase subranged data has looser coincidence criteria (10 μs) than the raw data, which requires strict coincidence. Figure 5.38 indicates that near the jet boundaries, particles have more lateral motion and the strict coincidence requirement of the particle raw data will omit these faster moving particles due to the erratic nature of the bed particle Doppler bursts discussed in Chapter 3, Section 2. Once again, the deviation outside the core region is not critical when calculating integral flow values.

In order to determine the repeatability of the experimental data and analysis procedure, the mass flow and momentum rates at each axial location were determined by 1) numerically integrating the LDV data points and by 2) using Gaussian velocity profiles for the respective phases as described in Section 5.2 Section 5.4. The resulting values are reported in Table 5.2. As expected, the data shows little deviation at the $y = 60$ and 70 mm locations but increases downstream due to the jet fluctuations. The void fractions and momentum rates calculated using the two techniques are nearly identical. The mass flow rates calculated using the Gaussian profile technique are slightly higher. This is because the momentum, and thus void fraction, calculations involve the square of the velocity profile, which is steeper than the velocity profile used for the mass flow calculations. Therefore, nearly all of the jet momentum is captured by the LDV data points whereas some of the jet mass flow lies beyond these measurements.

In such a complex system, it is difficult to identify all of the sources of uncertainty and error. The air flow rates are controlled by volumetric flow meters, which have an uncertainty of $\pm$ 7.5 SLPM, which translates into $\pm$ 1.72 m/s for the jet velocity

and ± 2.18 cm/s for the fluidization velocity. The temperature of the jet gas was maintained within ± 2°C. The largest sources of uncertainty are most likely due to particle size and shape variation. This is not only due to particle fabrication, but also to particle attrition and abrasion due the harsh flow conditions inside the bubbling bed. The bulk consistency of the particles was verified by repeating the fluidization curve tests before and after every experiment. Static levels were controlled as mentioned before but could become problematic as the amount of Larostat in the emulsion decreased over the duration of an experiment. Finally, optical alignment is critical due to the strong velocity gradients in the jet plume. Care was taken to ensure that the LDV probe head was oriented perpendicular to the 2D bed so that the LDV measurement volume was located in the center of the bed gap at all x and y locations.
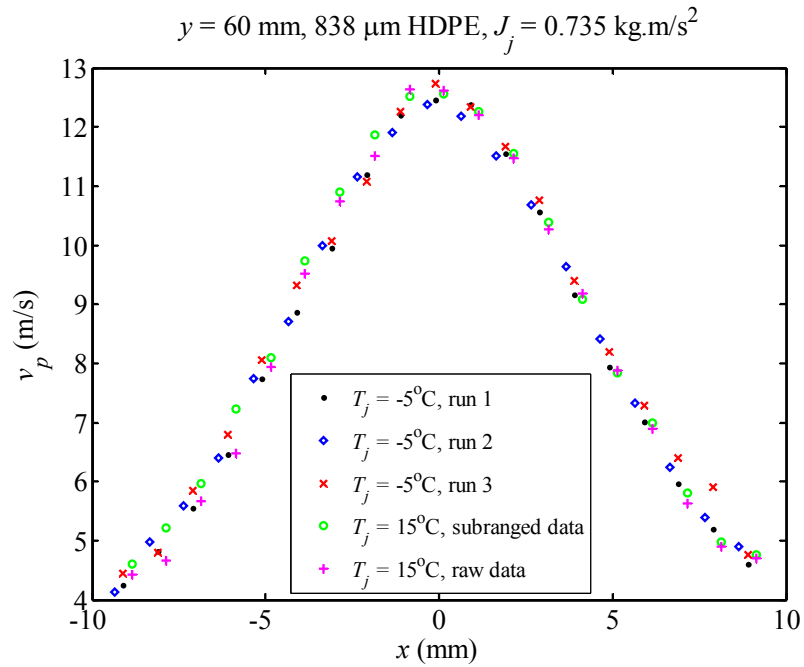
Figure 5.29: Particulate phase velocity profiles at $y = 60$ mm.
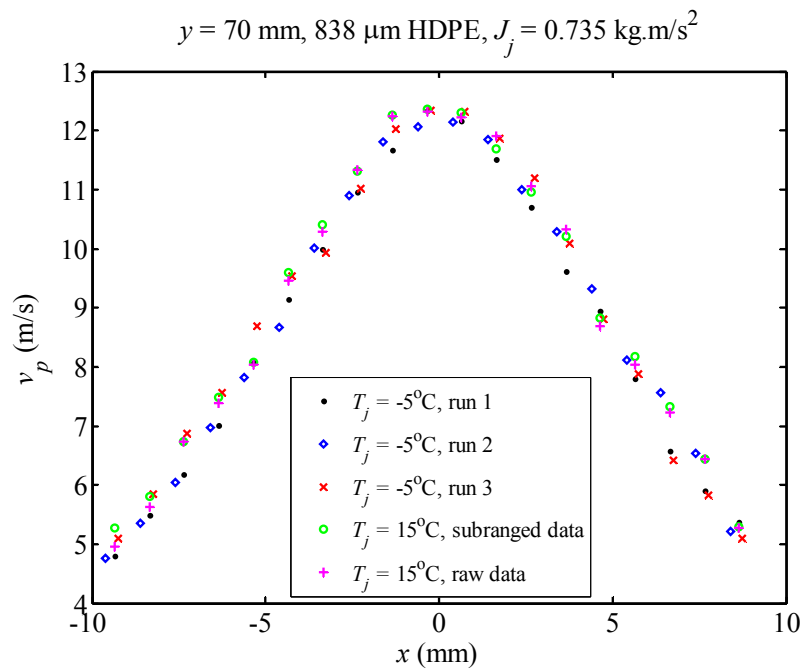
Figure 5.30: Particulate phase velocity profiles at $y = 70$ mm.
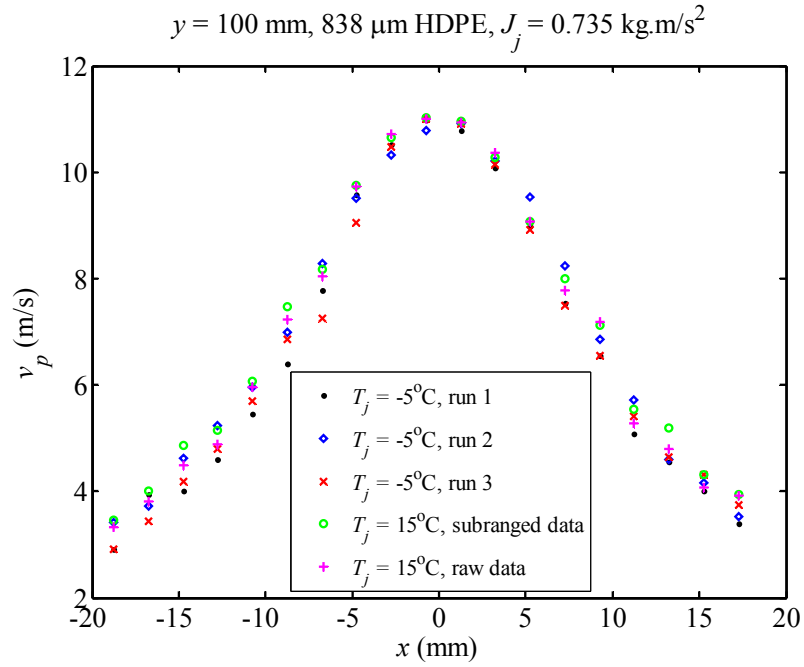
Figure 5.31: Particulate phase velocity profiles at y = 100 mm.
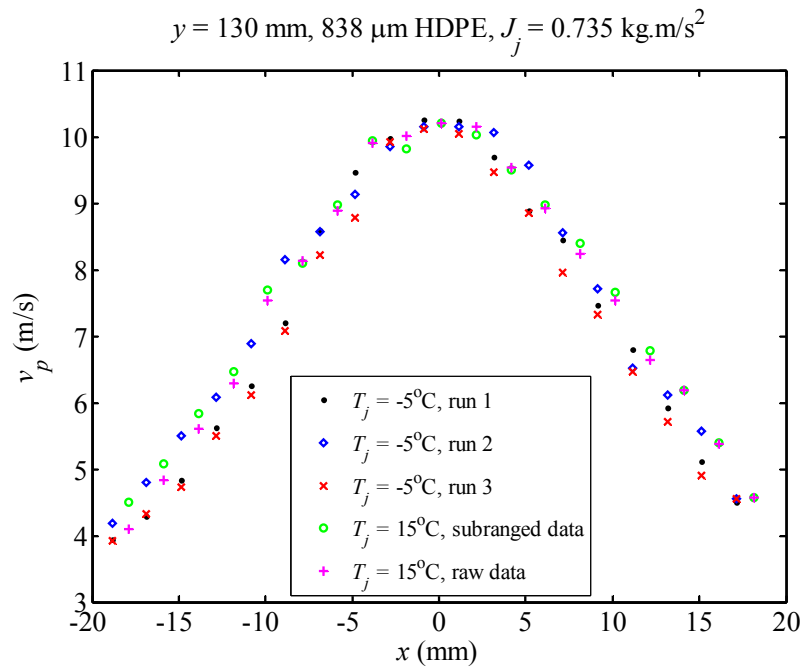
Figure 5.32: Particulate phase velocity profiles at y = 130 mm.
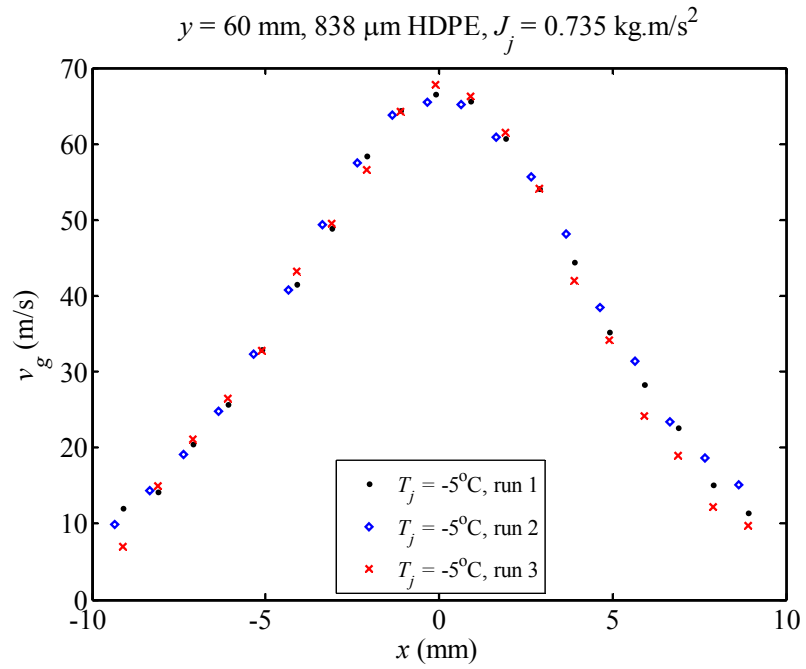
Figure 5.33: Gas phase velocity profiles at y = 60 mm.
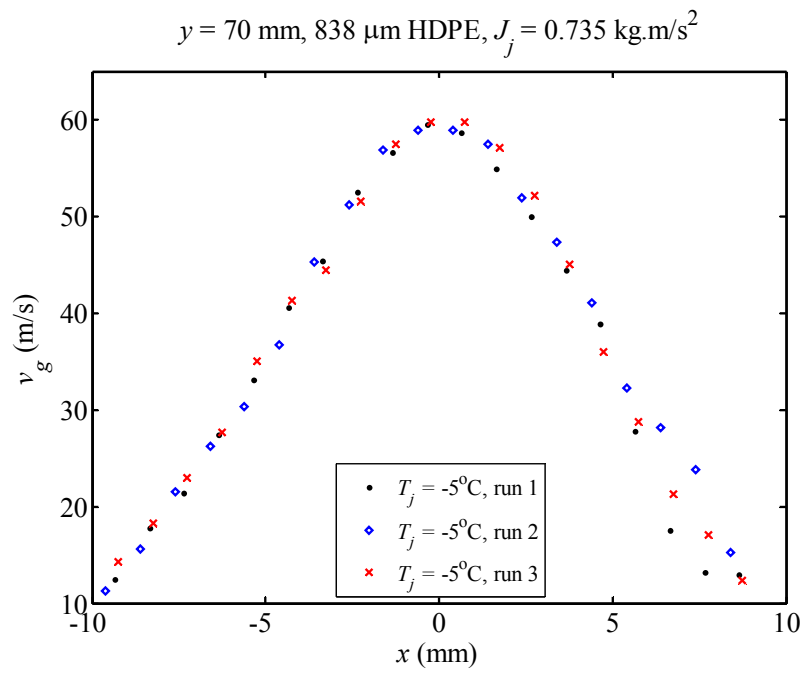
Figure 5.34: Gas phase velocity profiles at y = 70 mm.
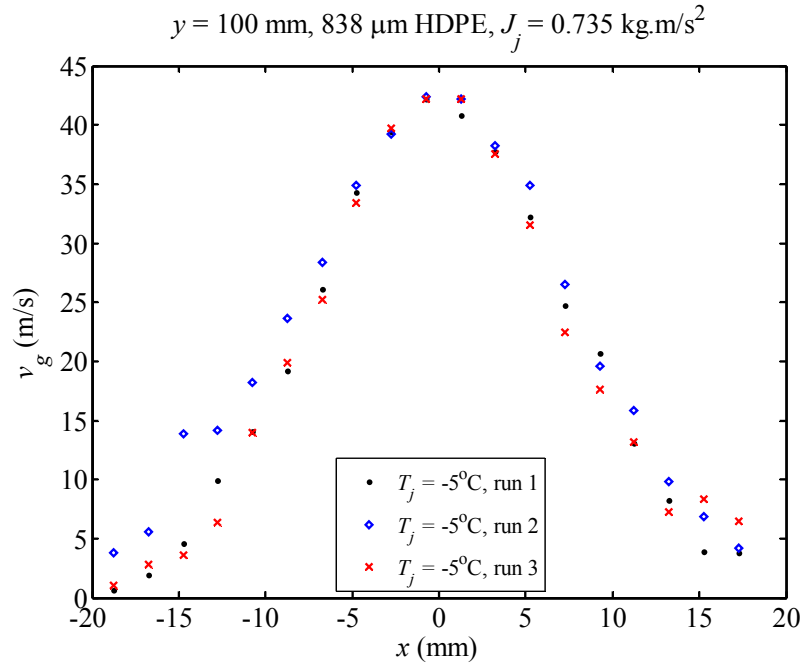
Figure 5.35: Gas phase velocity profiles at *y* = 100 mm.
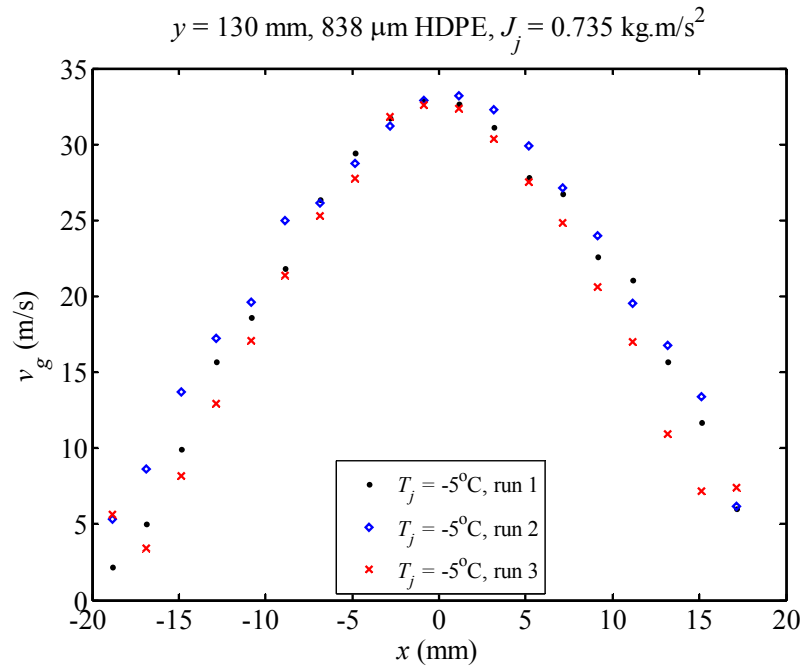
Figure 5.36: Gas phase velocity profiles at *y* = 130 mm.
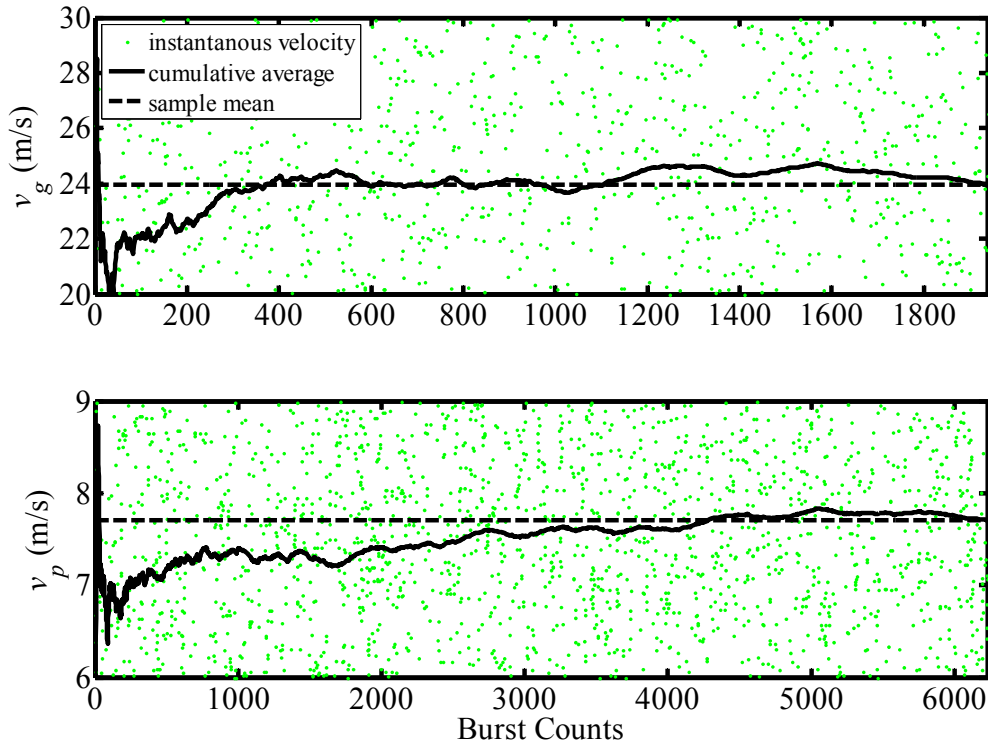
Figure 5.37: LDV gas and particulate phase velocity measurements at
y = 130 mm, x = 10 mm. 1,938 bursts were recorded for the gas phase and 6,231 bursts for the particulate
phase over the recording period of 120 seconds.

y = 60 mm, 838 μm HDPE, J_j = 0.735 kg.m/s^2
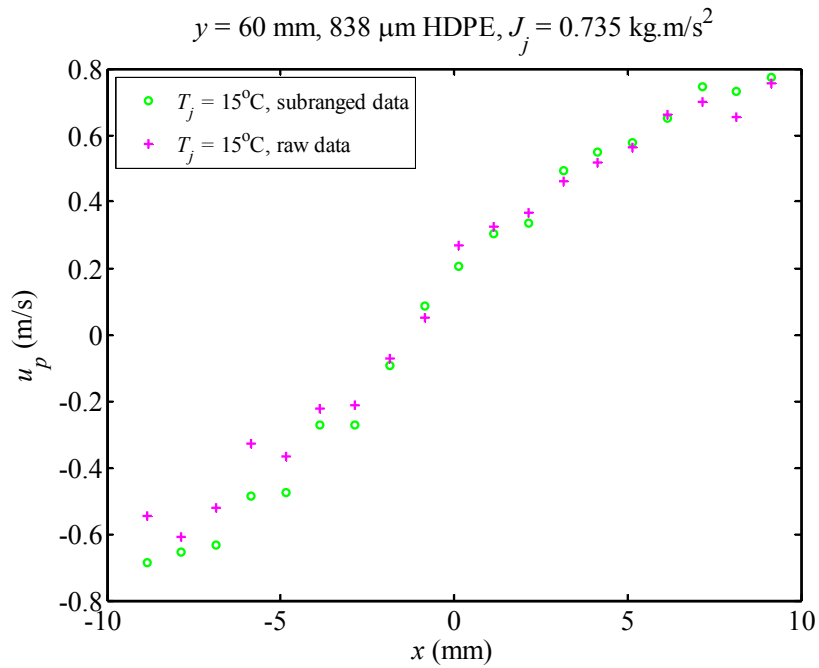
Figure 5.38: Particulate phase lateral velocity profiles at y = 60 mm.

	Numerical LDV Data Points					Gaussian Curve Fit				
y = 60 mm	**VF**	**m_g (kg/s)**	**J_g (kg.m/s^2)**	**m_p (kg/s)**	**J_p (kg.m/s^2)**	**VF**	**m_g (kg/s)**	**J_g (kg.m/s^2)**	**m_p (kg/s)**	**J_p (kg.m/s^2)**
T=-5C, run 1	0.9522	7.95E-03	3.01E-01	5.89E-02	4.35E-01	0.9525	8.06E-03	3.03E-01	6.14E-02	4.33E-01
T=-5C, run 2	0.9529	8.05E-03	3.06E-01	5.83E-02	4.30E-01	0.9530	8.10E-03	3.00E-01	6.22E-02	4.36E-01
T=-5C, run 3	0.9540	7.84E-03	2.99E-01	5.82E-02	4.37E-01	0.9551	8.07E-03	3.09E-01	5.92E-02	4.27E-01
average	0.9530	7.95E-03	3.02E-01	5.85E-02	4.34E-01	0.9535	8.08E-03	3.04E-01	6.09E-02	4.32E-01
std dev	0.0009	1.07E-04	3.61E-03	3.52E-04	3.61E-03	0.0014	1.95E-05	4.57E-03	1.54E-03	4.57E-03
STD/avg	0.09%	1.35%	1.19%	0.60%	0.83%	0.15%	0.24%	1.50%	2.53%	1.06%
y = 70 mm	**VF**	**m_g (kg/s)**	**J_g (kg.m/s^2)**	**m_p (kg/s)**	**J_p (kg.m/s^2)**	**VF**	**m_g (kg/s)**	**J_g (kg.m/s^2)**	**m_p (kg/s)**	**J_p (kg.m/s^2)**
T=-5C, run 1	0.9529	7.93E-03	2.69E-01	6.40E-02	4.67E-01	0.9532	8.05E-03	2.71E-01	6.66E-02	4.65E-01
T=-5C, run 2	0.9522	7.77E-03	2.71E-01	6.17E-02	4.64E-01	0.9511	7.95E-03	2.65E-01	6.86E-02	4.71E-01
T=-5C, run 3	0.9535	7.72E-03	2.71E-01	6.10E-02	4.65E-01	0.9549	8.10E-03	2.74E-01	6.61E-02	4.62E-01
average	0.9529	7.81E-03	2.70E-01	6.22E-02	4.66E-01	0.9531	8.03E-03	2.70E-01	6.71E-02	4.66E-01
std dev	0.0006	1.10E-04	1.40E-03	1.59E-03	1.40E-03	0.0019	7.87E-05	4.75E-03	1.29E-03	4.75E-03
STD/avg	0.07%	1.41%	0.52%	2.55%	0.30%	0.20%	0.98%	1.76%	1.92%	1.02%
y = 100 mm	**VF**	**m_g (kg/s)**	**J_g (kg.m/s^2)**	**m_p (kg/s)**	**J_p (kg.m/s^2)**	**VF**	**m_g (kg/s)**	**J_g (kg.m/s^2)**	**m_p (kg/s)**	**J_p (kg.m/s^2)**
T=-5C, run 1	0.9572	8.62E-03	2.03E-01	8.57E-02	5.33E-01	0.9571	8.70E-03	2.08E-01	8.50E-02	5.28E-01
T=-5C, run 2	0.9608	9.40E-03	2.23E-01	8.10E-02	5.13E-01	0.9601	9.19E-03	2.19E-01	8.38E-02	5.17E-01
T=-5C, run 3	0.9569	8.45E-03	1.98E-01	8.66E-02	5.38E-01	0.9566	8.40E-03	2.01E-01	8.61E-02	5.35E-01
average	0.9583	8.82E-03	2.08E-01	8.44E-02	5.28E-01	0.9579	8.76E-03	2.09E-01	8.50E-02	5.27E-01
std dev	0.0022	5.08E-04	1.29E-02	2.99E-03	1.29E-02	0.0019	3.98E-04	9.07E-03	1.16E-03	9.07E-03
STD/avg	0.23%	5.76%	6.22%	3.54%	2.45%	0.20%	4.54%	4.34%	1.36%	1.72%
y = 130 mm	**VF**	**m_g (kg/s)**	**J_g (kg.m/s^2)**	**m_p (kg/s)**	**J_p (kg.m/s^2)**	**VF**	**m_g (kg/s)**	**J_g (kg.m/s^2)**	**m_p (kg/s)**	**J_p (kg.m/s^2)**
T=-5C, run 1	0.9582	8.78E-03	1.74E-01	8.94E-02	5.61E-01	0.9616	9.60E-03	1.79E-01	9.60E-02	5.57E-01
T=-5C, run 2	0.9606	9.10E-03	1.83E-01	8.67E-02	5.53E-01	0.9594	9.59E-03	1.79E-01	9.70E-02	5.57E-01
T=-5C, run 3	0.9553	8.26E-03	1.60E-01	9.38E-02	5.76E-01	0.9585	9.17E-03	1.69E-01	9.90E-02	5.67E-01
average	0.9580	8.71E-03	1.72E-01	9.00E-02	5.63E-01	0.9599	9.46E-03	1.76E-01	9.74E-02	5.60E-01
std dev	0.0027	4.28E-04	1.14E-02	3.56E-03	1.14E-02	0.0016	2.43E-04	5.50E-03	1.50E-03	5.50E-03
STD/avg	0.28%	4.91%	6.60%	3.96%	2.02%	0.17%	2.57%	3.14%	1.55%	0.98%

Table 5.2: Experimental repeatability. Void fraction, and mass flow, and momentum rate values were calculated at each axial location using both the LDV data points and the Gaussian curve profiles.

5.7 Chapter 5 References

W. K. George. "The self-preservation of turbulent flows and its relation to initial conditions and coherent structures," in W. K. George and R. Arndt, <u>Advances in Turbulence</u>, pp. 39-73, Hemisphere, New York (1989).

L. Massimilla. "Gas Jets in Fluidized Beds," in J.F. Davidson, R. Clift, and D. Harrison, <u>Fluidization, Second Ed.</u>, pp. 133-171, Academic Press (1985).

J.M.D. Merry. "Penetration of a horizontal gas jet into a fluidized bed," Trans. Instn. Chem. Engrs. (49) 189-195 (1971).

F.M. White. <u>Viscous Fluid Flow</u>. McGraw-Hill, (2006).

H. Schlichting. <u>Boundary-Layer Theory, 7th Ed</u>. Translated by J. Kestin. McGraw-Hill (1979)

C. Xuereb, C. Laguerie, T. Baron. "Etude du comportement de jets continues horizontaux ou inclines introduits dans un lit fluidise par un gaz I: Morphologie des jets," Powder Tech .**67**, 46-56 (1991)

C. Xuereb, C. Laguerie, T. Baron. "Etude du comportement de jets continues horizontaux ou inclines introduits dans un lit fluidise par un gaz Deuxieme partie: profiles de vitesse du gaz dans les jets horizontaux," Powder Tech. **64** (3), 271-283 (1991)

W. Yanta & R. Smith. "Measurements of Turbulence Transport Properties with a Laser Doppler Velocimeter," Paper No. 73-169, AIAA 11th Aerospace Sciences Meeting, Washington, DC. (1973)

CHAPTER 6:

EFFECT OF FLUIDIZATION ON JET DYNAMICS AND PHASE VELOCITY SCALING

In the previous chapter, the gas and particulate phase velocities were used to determine the volume fraction, mass flow, and momentum rate for each phase at the given axial locations. In this chapter, the effect of fluidization velocity on the jet dynamics is examined. Using the same batch of 838 μm HDPE miropellets and maintaining the same gas jet inlet conditions (V_j = 92 m/s and T_j = -5°C), the emulsion was fluidized at V_{fl}/V_{mf} = 0, 0.7, 1, 1.15, 1.3, 1.5. The maximum centerline velocity and half-velocity points for each phase are determined at the given axial locations. As described by the analysis in the prior chapter, this data is then used to calculate volume fraction, mass flow, and momentum rates for each phase based on the Gaussian velocity profile shapes.

In addition to the integral flow values, phase velocity scaling was also investigated. The scaling is based on the development of similarity velocity profiles for the two phases. Additional experiments were carried out with 1) 838 μm HDPE miropellets with V_{fl}/V_{mf} = 1.15 held constant while varying V_j and 2) various types of bed particles while maintaining V_j = 92 m/s and V_{fl}/V_{mf} = 1.15 constant.

6.1 Effect of Fluidization Velocity

As mentioned in the introduction, Roach (1993) proposed that the centerline maximum velocity and plume width were both functions of the fluidization rate. Increasing the fluidization velocity decreases the maximum centerline velocity and widens the velocity profiles for both phases as shown in Figure 6.2, Figure 6.3, Figure 6.5, and Figure 6.6. As expected, Figure 6.1 shows that the centerline gas phase velocity for all bubbling bed cases is significantly reduced when compared to the empty bed case

due to momentum transfer to the particulate phase. However, Figure 6.5 reveals that the gas phase velocity profile width at minimum fluidization is comparable to the empty bed. The gas velocity profile is narrower when the emulsion is fluidized below this point and widens with increasing fluidization.

Figure 6.4 reveals that the ratio of the maximum gas phase velocity to the maximum particulate phase velocity seems unaffected by the fluidization state of the emulsion. This phenomenon will be discussed in the next section. Figure 6.7 indicates that increasing fluidization velocity tends to widen the gas velocity profile with respect to the particulate phase velocity profile as more interstitial gas is entrained.

Another important parameter affected by fluidization that Roach did not mention is the phase volume fraction in the jet plume. In Figure 6.8, it is evident that void fraction has a strong dependency on the fluidization state of the emulsion. In a spouted bed (no fluidization), the momentum averaged void fraction is roughly 94%. At 50% excess fluidization, this value increases to about 98%. Once again, this corresponds to a significant change in the solids fraction, ($1-\varepsilon$), and thus the particulate phase transport rates.

The gas phase mass flow rates at the various fluidization rates are compared with the jet inlet value and the empty bed case in Figure 6.9. This figure indicates that when the emulsion is fluidized below the minimum fluidization rate, gas originating from the jet inlet diffuses into the emulsion downstream to locally fluidize the particles as the gas phase mass flow decreases downstream. Above the minimum fluidization rate, interstitial gas and bubbles in the emulsion are entrained into the jet plume as the gas phase mass flow increases downstream. (Unfortunately, this trend cannot be verified by the lateral velocity flux of the gas phase near the plume boundaries as the interstitial gas is not seeded with LDV ice tracer crystals; only the gas that originates at the inlet is seeded, which mixes laterally outwards.) As the fluidization rate increases, the gas phase mass flow increases and approaches the empty bed values. The two phases compete for entrainment into the jet plume, as is indicated by the decrease in particulate phase mass flow with increasing fluidization (Figure 6.10).

The dependency of the gas and particulate phase momentum rates on the fluidization rate are shown in Figure 6.11 and Figure 6.12, respectively. As the

114

fluidization rate increases, the gas phase momentum increases due to increased interstitial gas entrainment. Once again, the particulate phase momentum decreases with increasing fluidization due to competition with the increased interstitial gas entrainment.

Finally, the particle drag coefficient was calculated using the Gaussian particulate and slip velocity profiles as well as the calculated void fractions as described in the previous chapter. The average value for the axial locations in the jet plume are reported in Table 6.1. The particle drag coefficient values at every fluidization condition are in good agreement with the established empirical value of 0.4.

Note that the uncertainty for the fluidization velocity is ± 2.18 cm/s and that the minimum fluidization velocity for this emulsion is 29 cm/s. This translates into a fluidization ratio uncertainty of 7.5%. Therefore, the V_{fl}/V_{mf} = 1 and 1.15 runs may be within the fluidization resolution limit of this system. All of the prior tests (analysis and uncertainty) were run at V_{fl}/V_{mf} = 1.15 so that the state of the emulsion would be consistently in a fluidized state. However, data acquired at minimum fluidization conditions is often of interest and therefore was obtained as part of this research.
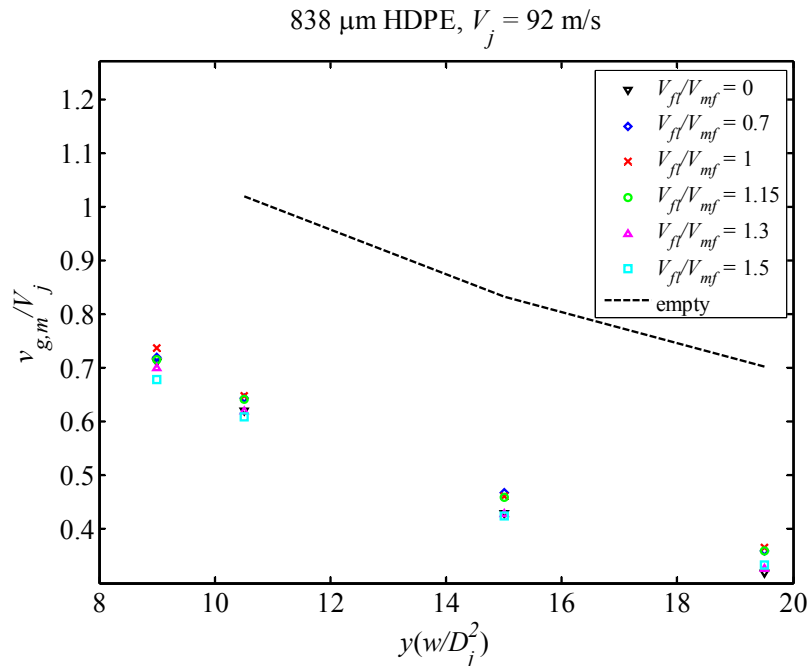
Figure 6.1: Maximum velocity values for the gas phase with varying fluidization velocity compared with the empty bed data. The momentum transfer from the gas to the particulate phase significantly reduces the maximum velocity values.
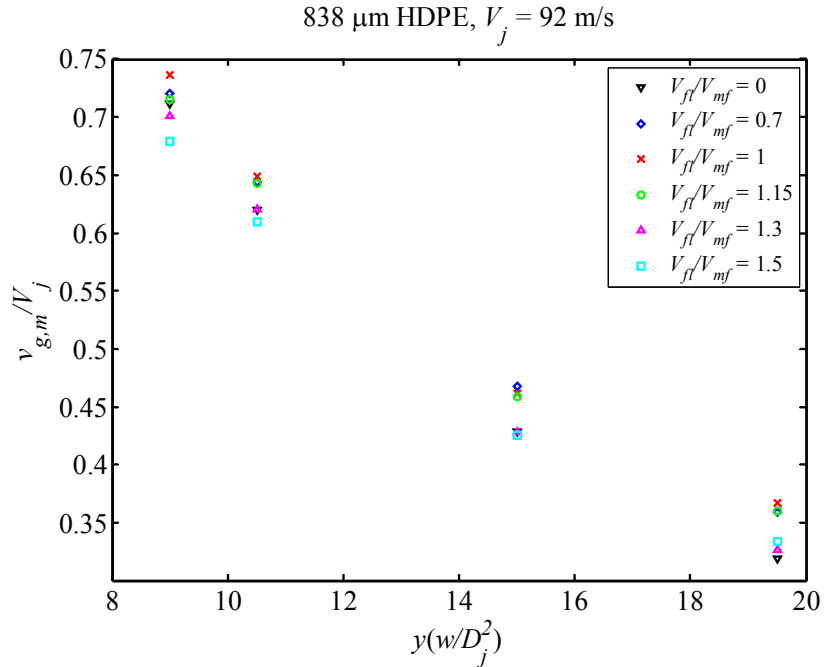
Figure 6.2: Maximum velocity values for the gas phase with varying fluidization velocity. Increasing the fluidization velocity tends to decrease the maximum velocity values.
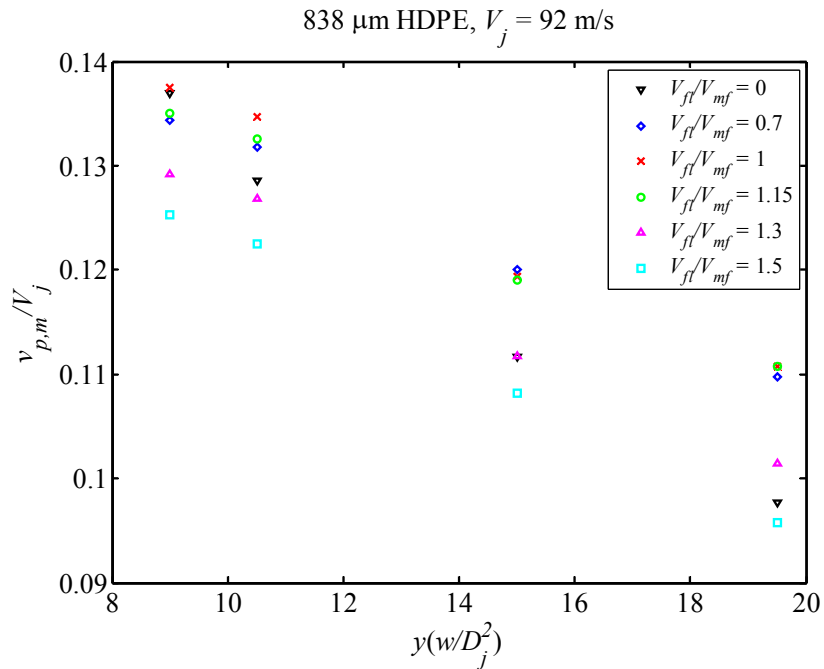
Figure 6.3: Maximum velocity values for the particulate phase with varying fluidization velocity. Increasing the fluidization velocity tends to decrease the maximum velocity values.
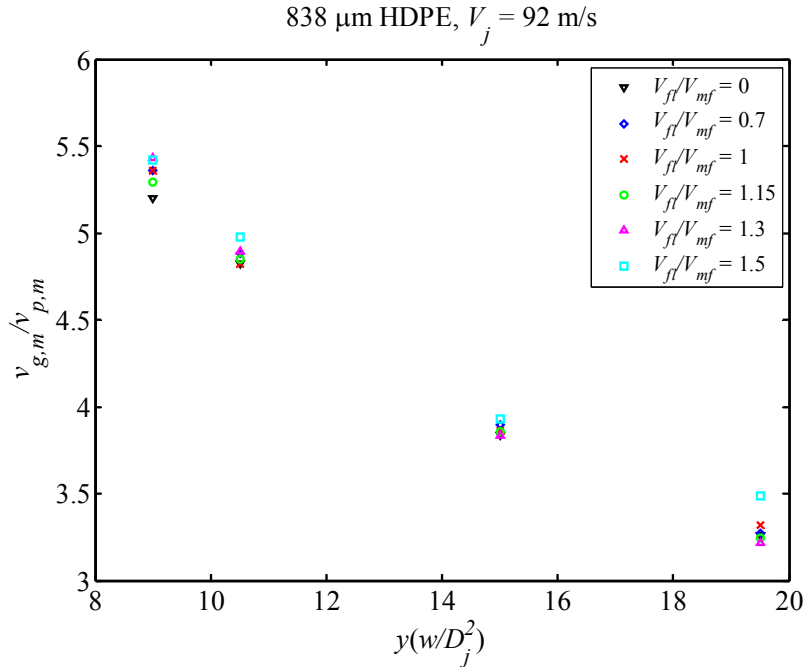
Figure 6.4: Ratio of the maximum velocity values for the gas and particulate phase with varying fluidization velocity. The ratio of maximum velocities appears to be independent of the fluidization velocity.
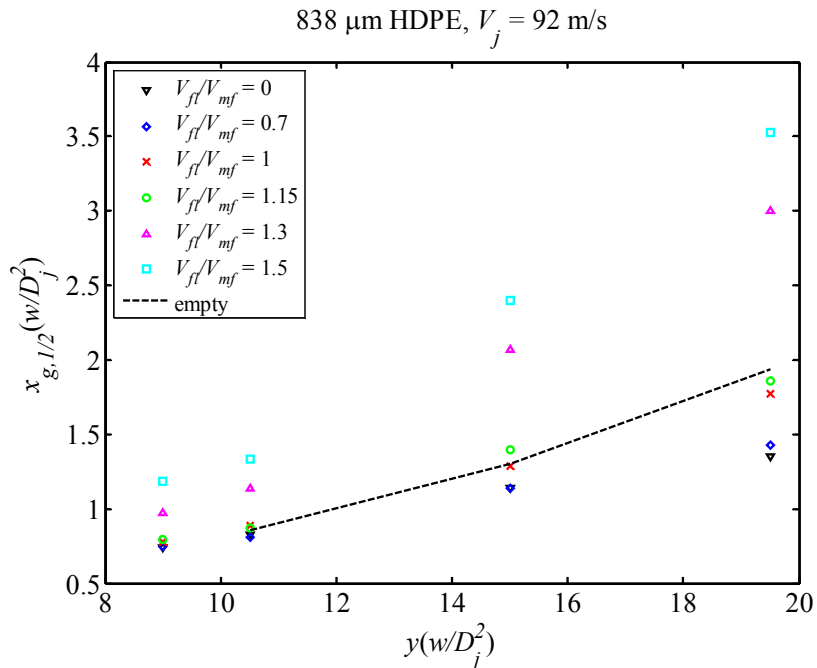
Figure 6.5: Half-velocity point values for the gas phase with varying fluidization velocity compared with the empty bed data. The gas phase velocity profile width at minimum fluidization is comparable to the empty bed. Increasing the fluidization velocity tends to widen the velocity profile.
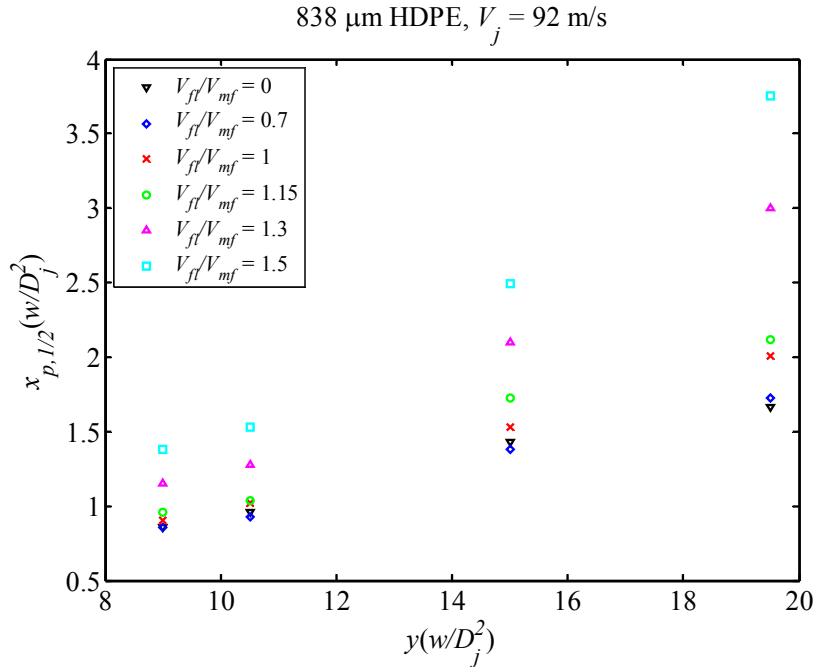
Figure 6.6: Half-velocity point values for the particulate phase with varying fluidization velocity. Increasing the fluidization velocity tends to widen the velocity profile.
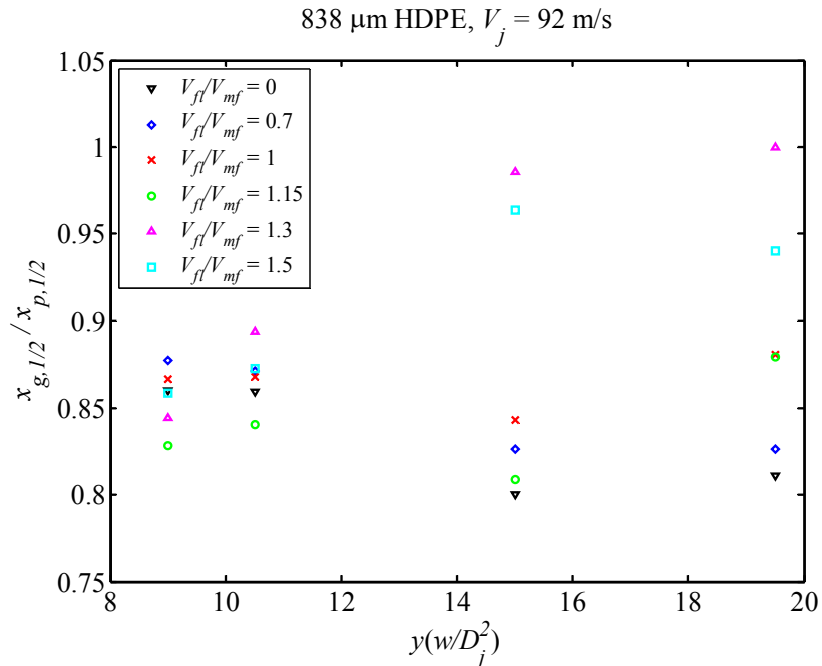
Figure 6.7: Ratio of the half-velocity point values for the gas and particulate phases with varying fluidization velocity. Increasing the fluidization velocity tends to widen the gas velocity profile with respect to the particulate phase velocity profile as more interstitial gas is entrained.
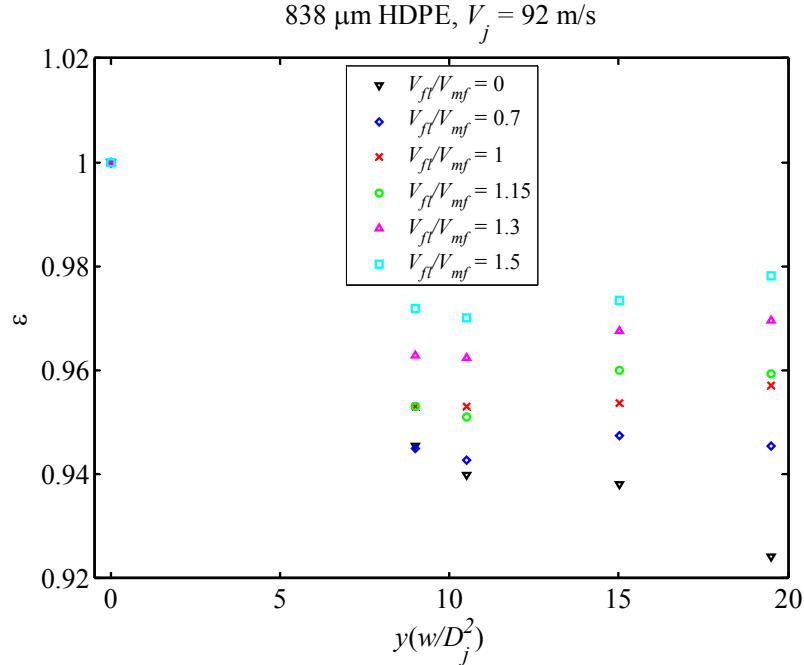
Figure 6.8: Void fraction values with varying fluidization velocity. Increasing the fluidization velocity tends to increase the void fraction in the jet plume.
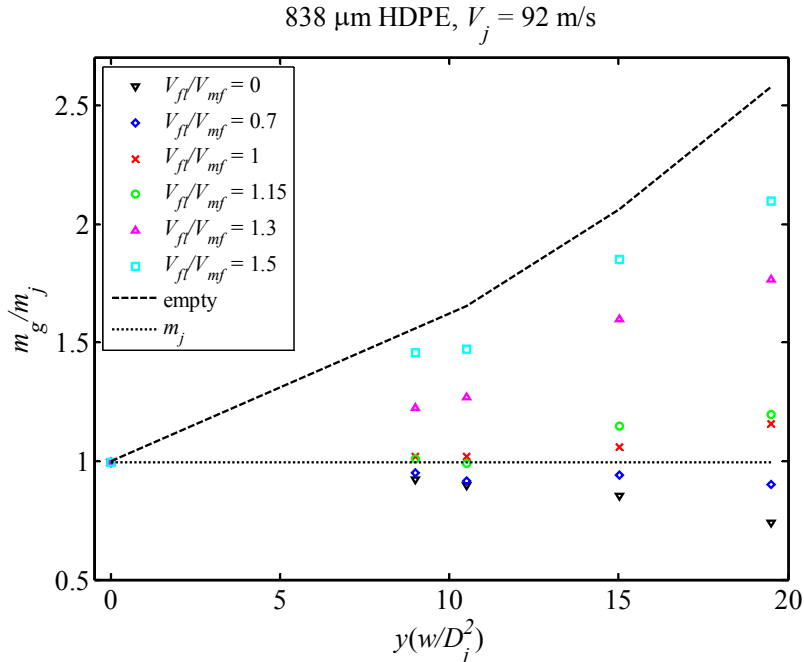
Figure 6.9: Mass flow rates for the gas phase with varying fluidization velocity compared with the empty bed data and jet inlet value. When the emulsion is fluidized below the minimum fluidization rate, gas originating from the jet inlet diffuses into the emulsion downstream to locally fluidize the particles as the gas phase mass flow decreases downstream. Above the minimum fluidization rate, interstitial gas and bubbles in the emulsion are entrained into the jet plume as the gas phase mass flow increases downstream. As the fluidization rate increases, the gas phase mass flow increases and approaches the empty bed values.

119
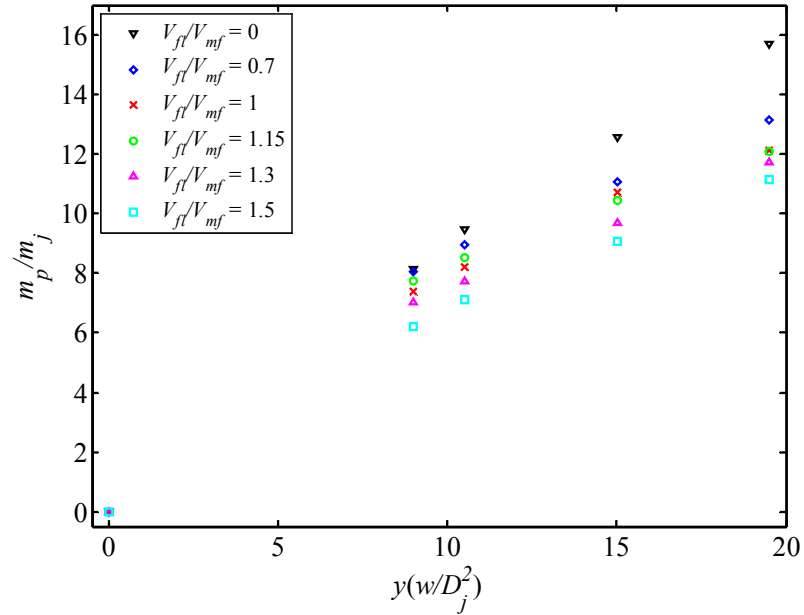
Figure 6.10: Mass flow rates for the particulate phase with varying fluidization velocity. As the fluidization rate increases, the particulate phase mass flow decreases due to competition with the increased interstitial gas entrainment.
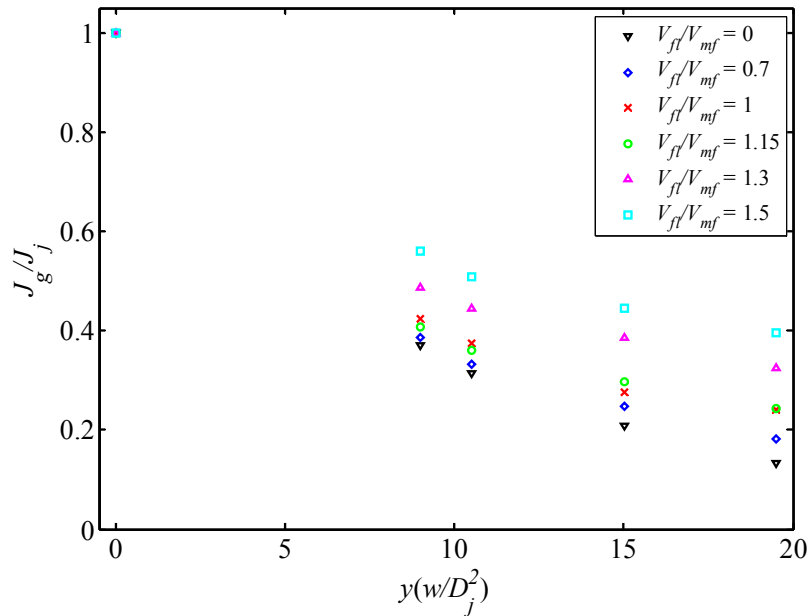

Figure 6.11: Momentum rates for the gas phase with varying fluidization velocity. As the fluidization rate increases, the gas phase momentum increases due to increased interstitial gas entrainment.
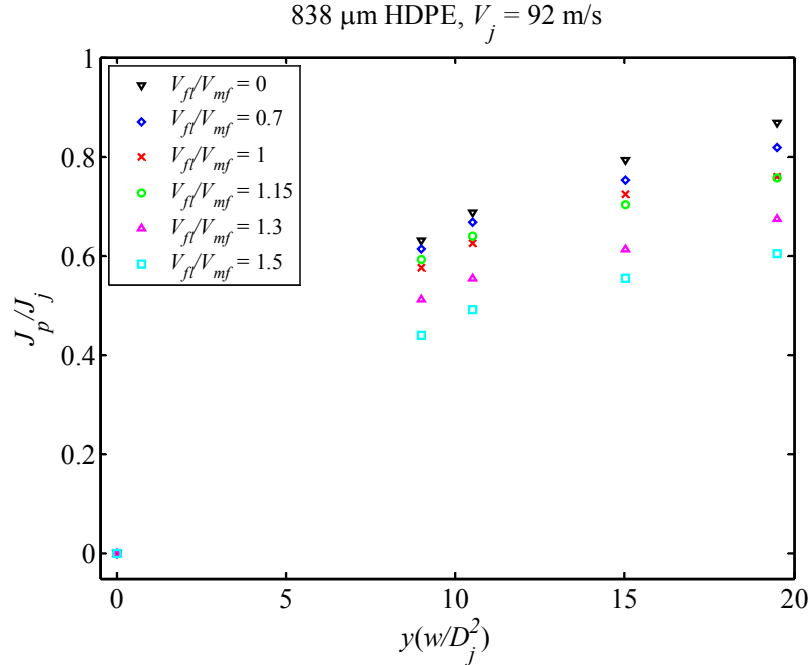
Figure 6.12: Momentum rates for the particulate phase with varying fluidization velocity. As the fluidization rate increases, the particulate phase momentum decreases due to competition with the increased interstitial gas entrainment.

V_{fl}/V_{mf}	C_D
0	0.48
0.7	0.42
1	0.38
1.15	0.38
1.3	0.37
1.5	0.43

Table 6.1: Particle drag coefficients. The values were determined in the same manner as described in Chapter 6, using the Gaussian particulate phase and slip velocity profiles along with the calculated void fraction values.

6.2 Phase Velocity Scaling

In the previous section, the bed particle emulsion and jet inlet velocity remained constant and the fluidization level of the bed was varied. It was noted that the ratio of the maximum velocities for the gas and particulate phases appeared to be independent of fluidization. In this section, the maximum velocities are reported when 1) the particle emulsion and fluidization level is held constant but the jet velocity is varied and 2) the jet velocity and fluidization ratio is held constant but the bed particles are varied.

The gas phase and particulate phase centerline velocities are plotted in Figure 6.13 and Figure 6.14, respectively. As expected, both the maximum velocity for both phases decreases with decreasing jet inlet velocity. Figure 6.7 reveals that once again, the ratio of the gas to particulate phase centerline velocities seems to collapse along the same curve. Unfortunately, full velocity profiles were not obtainable as the lower jet velocity significantly reduced the ice crystal seeding. Lower air flow rates through the dry ice heat exchanger vessel allowed the ice crystals to accumulate along the inside wall as the flexible rubber hose attached to the inlet port did not have enough momentum to whip about vigorously. As a result, mass flow, momentum, and void fraction values were not calculated for these experiments. Additionally, the uncertainty of gas phase velocity values for these runs will be slightly higher due to the decreased burst count.

Figure 6.13: Maximum velocity values for the gas phase with varying jet inlet velocity.

Figure 6.14: Maximum velocity values for the particulate phase with varying jet inlet velocity.

Figure 6.15: Ratio of the maximum velocity values for the gas and particulate phase with varying jet inlet velocity. The ratio of maximum velocities appears to be independent of the jet inlet velocity.

Next, the jet velocity (V_j = 92 m/s) and fluidization levels (V_{fl}/V_{mf} = 1.15) were held constant and the bed particles were changed. These particles included 700 μm PTFE Teflon agglomerates ($\rho_p \sim$ 2,150 kg/m^3), 800 μm poppy seeds ($\rho_p \sim$ 1,050 kg/m^3),

2,200 μm mustards seeds ($\rho_p \sim$ 1,150 kg/m^3), and 950 μm amaranth grains ($\rho_p \sim$ 1,000 kg/m^3). The minimum fluidization velocities for the various emulsions were measured and the individual particles were characterized *via* micrometer measurements and liquid displacement. Accurate particle diameter and density values were not necessarily useful as these particles are not nearly as robust as the extruded HDPE micropellets; the Teflon agglomerates as well as the organic seeds and grains broke down after several minutes in the bubbling bed. Therefore, only the maximum centerline velocities were recorded in the short time that the experiments were run. For all the particle types, the intensity and coincidence subranging technique described in Chapter 3 sufficed. This was confirmed with the distinct binormal velocity distribution that occurs along the centerline due to the high slip velocity.

The wide range of gas phase centerline velocity values are plotted in Figure 6.16. The large mustard seeds had the lowest gas phase velocity while the small PTFE Telfon agglomerates had the highest. Figure 6.17 shows a similar trend for the particulate phase maximum velocities. Though not as clean as with the prior two tests, Figure 6.18 suggests that the ratio of the gas to particulate phase centerline velocities seems to collapse along the same curve.

The centerline velocity data from all the experiments is plotted in Figure 6.19, Figure 6.20, and Figure 6.21. Note that the non-intrusive, simultaneous gas and particulate phase measurements make the observation of the centerline velocity ratio trend possible. The most noticeable deviation occurs at the $y = 60$ and 70 mm locations with the amaranth grains and $y = 100$ and 130 mm locations with the mustard seeds. As mentioned before, these organic particles were susceptible to breaking down in the bubbling bed, which created oil and dust in the emulsion as well as erratic particle shapes. Therefore, these deviations from the trend curve could be due to cohesive forces, dust contamination, and variations in particle drag coefficients.
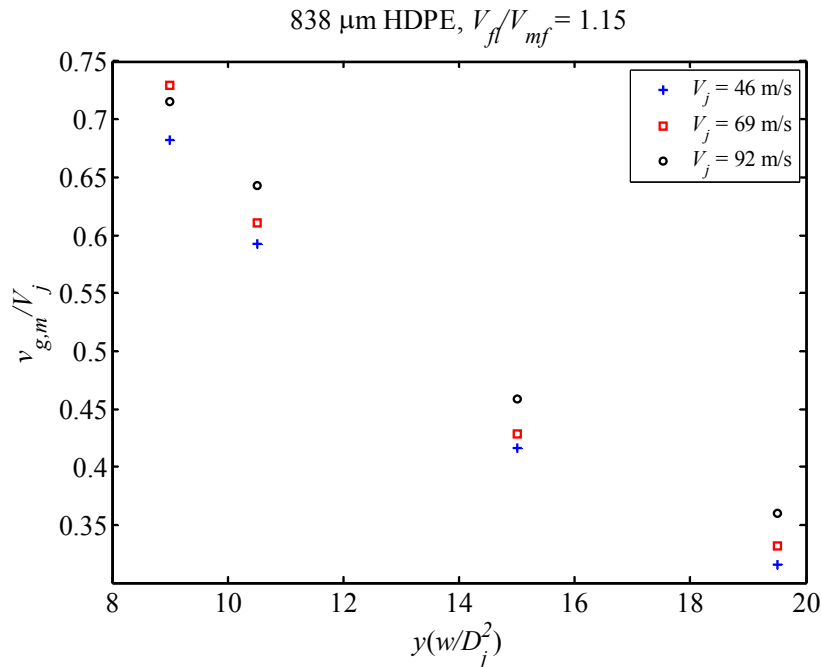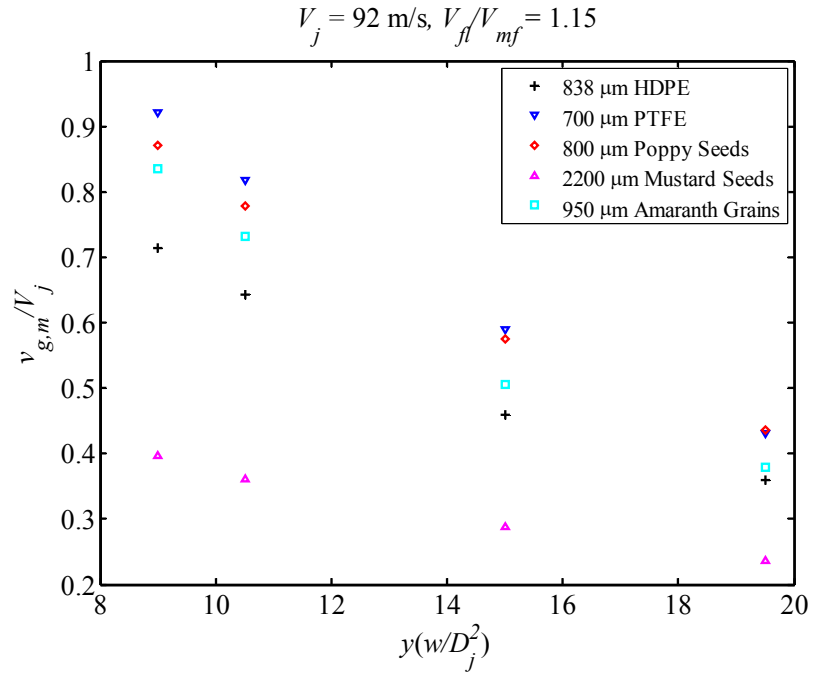
Figure 6.16: Maximum velocity values for the gas phase with varying the bed particles.
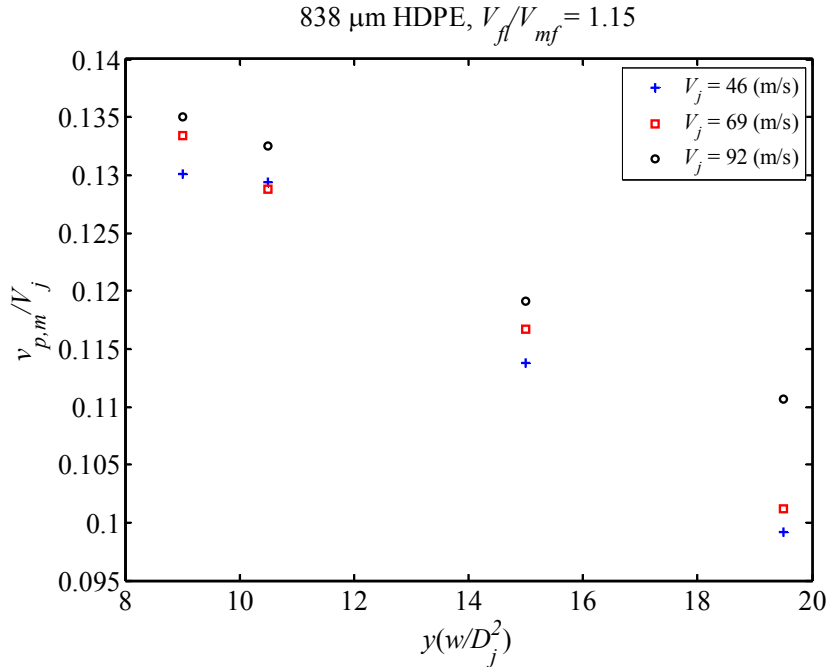

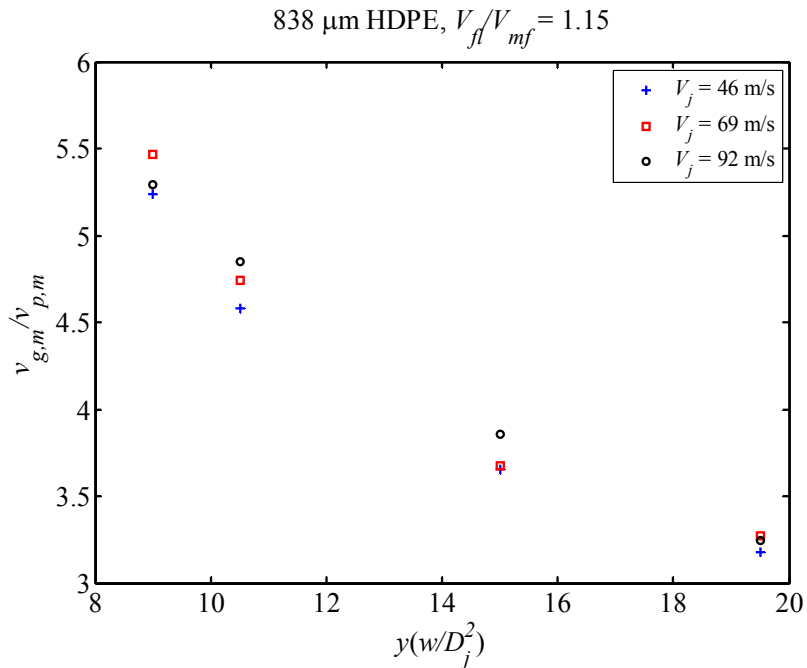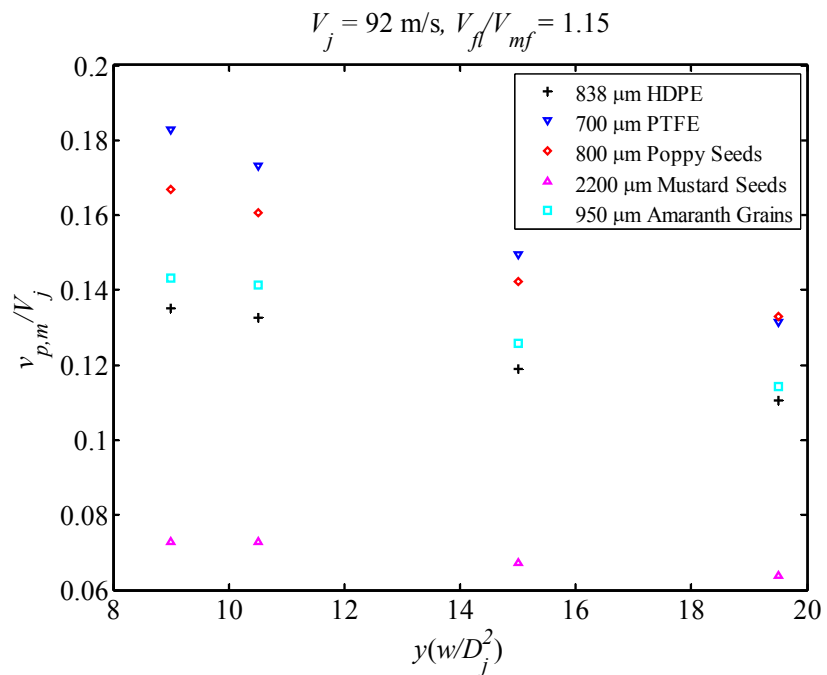Figure 6.17: Maximum velocity values for the particulate phase with varying the bed particles.

125
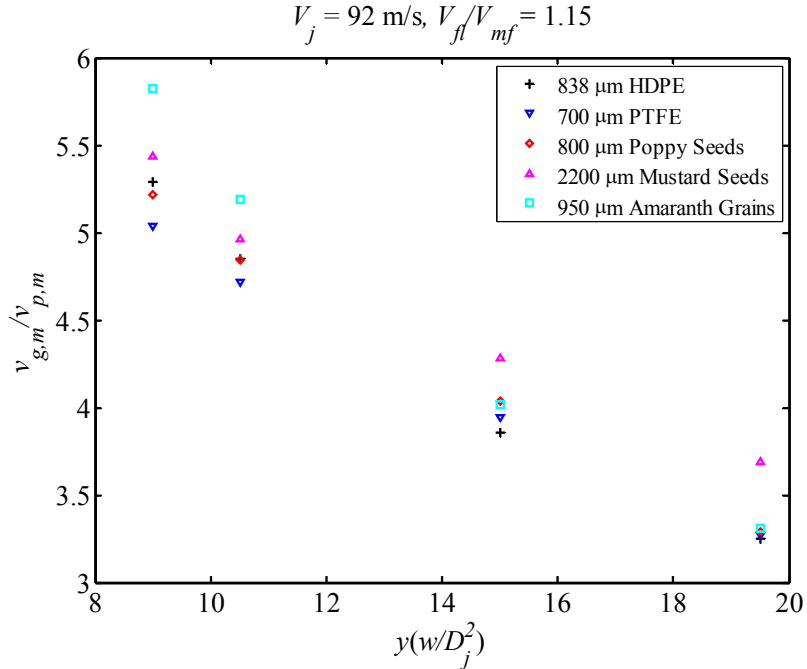
Figure 6.18: Ratio of the maximum velocity values for the gas and particulate phase with varying bed particles. The ratio of maximum velocities appears to be independent of the bed particles.
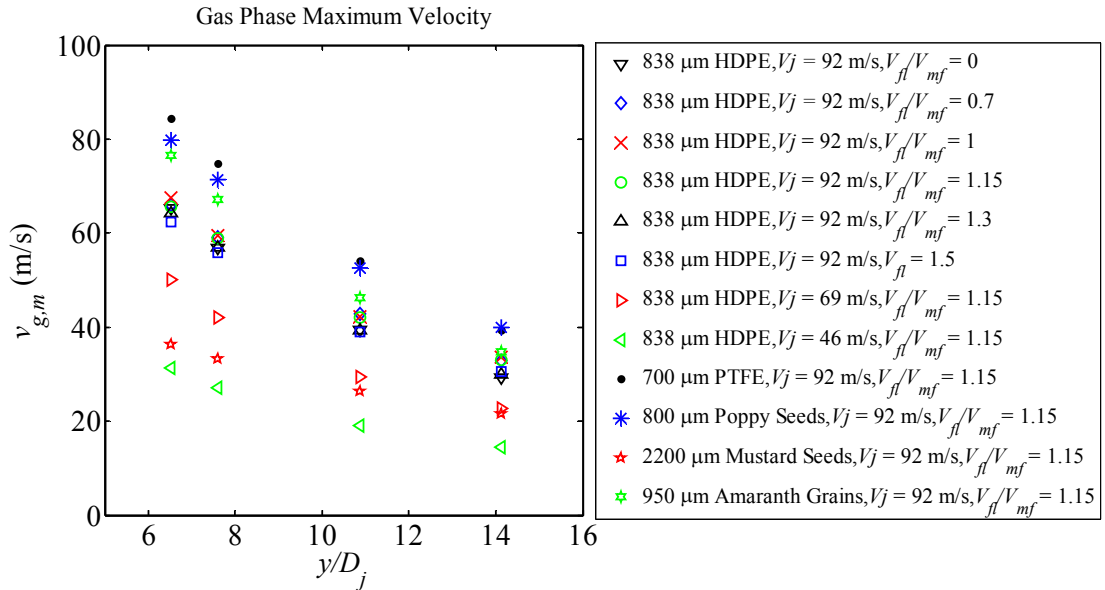
Figure 6.19: Maximum velocity values for the gas phase for all cases.
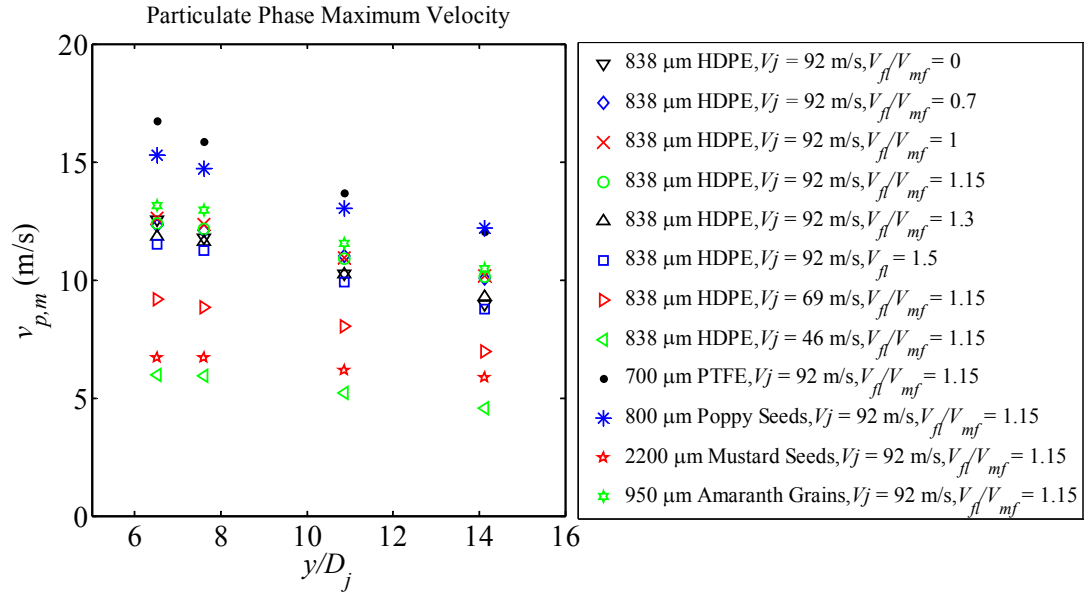
Figure 6.20: Maximum velocity values for the particulate phase for all cases. Note that Eulerian particulate phase velocity never increases with streamwise distance.
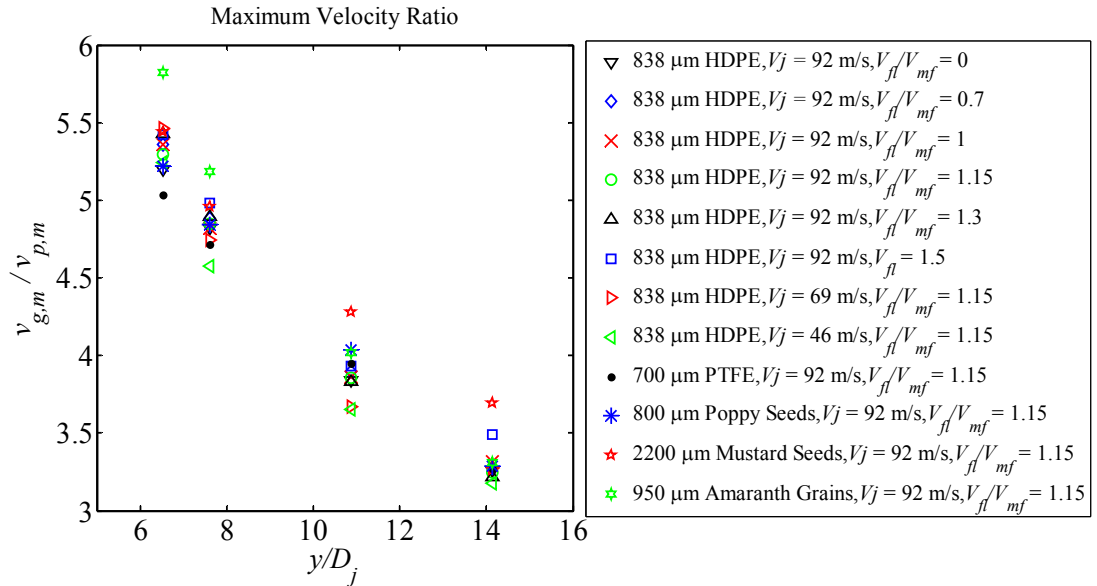
Figure 6.21: Ratio of the maximum velocity values for the gas and particulate phase for all cases. The ratio of maximum velocities appears to collapse along the same curve.

For a single particle tracking in the Lagrangian frame, the ratio of the surrounding gas velocity to the particle velocity will approach unity and the slip velocity will approach zero due to momentum transfer *via* drag. According to equation (5.16) and equation (5.18) the acceleration of a single particle is a function of the local gas velocity,

127

particle mass, and particle size. Therefore, velocity ratio data obtained in a Lagrangian frame for all the test cases would not necessarily collapse along a single curve as it has for the Eulerian frame LDV measurements.

Physical insight as to why the Eulerian centerline velocity ratio seems to lie is examined. As mentioned before, the Eulerian measurements are field variables of space that accounts for the velocity of every particle that passes through a particular location. Therefore, the data suggest that at a specific axial location

$$\frac{v_{g,m}}{v_{p,m}} = constant \ for \ a \ given \ axial \ distance$$

(6.33)

which is equivalent to

$$\frac{v_{g,m} - v_{p,m}}{v_{p,m}} = constant \ for \ a \ given \ axial \ distance$$

(6.34)

As expected, Figure 6.22 shows that the ratio of the maximum slip velocity to the maximum particulate phase velocity collapses in a similar manner. Squaring the terms in equation (6.34) and multiplying through by the solids fraction

$$\frac{(1-\varepsilon)(v_{g,m} - v_{p,m})^2}{(1-\varepsilon)v_{p,m}^2} = constant \ for \ a \ given \ axial \ distance$$

(6.35)

implies that

$$\frac{(1-\varepsilon)(v_{g,m} - v_{p,m})^2}{(1-\varepsilon)v_{p,m}^2} \sim \frac{f_D}{\dot{J}_P} = constant \ for \ a \ given \ axial \ distance$$

(6.36)

Equation (6.36) suggests that the ratio of the drag force coupling and the particulate phase momentum is constant at a given location downstream from the jet inlet. Note that

$$\dot{J}_P = \dot{J}_j - \dot{J}_g$$

(6.37)

so that the same can be said of the gas phase momentum and drag force coupling. This phenomenon seems applicable for high speed gas jets in a bubbling bed with spherical particle entrainment when $Re_p > 1000$ so that $C_D \sim 0.4$.

It is important to keep in mind that the Eulerian velocity values for each phase are mass averaged values. As stated in Chapter 4, the mass averaged velocity is simply the ratio of momentum to mass flow. Assuming self-similar velocity profiles, the mass

averaged velocities for the gas and particulate phases for a given axial location can be written as

$$V_{g,m} = \frac{\dot{J}_g}{\dot{m}_g} = \frac{C_2 \rho_g w \int_{-b}^{b} \varepsilon v_g^2 dx}{C_1 \rho_g w \int_{-b}^{b} \varepsilon v_g dx} = \frac{C_2 \rho_g w \left(v_{g,m}^2 x_{g,1/2}\right) \int_{-2}^{2} \varepsilon f_g^2 d\xi}{C_1 \rho_g w \left(v_{g,m} x_{g,1/2}\right) \int_{-2}^{2} \varepsilon f_g d\xi} = v_{g,m} \left[\frac{C_2 \int_{-2}^{2} \varepsilon f_g^2 d\xi}{C_1 \int_{-2}^{2} \varepsilon f_g d\xi} \right] \quad (6.38)$$

$$V_{p,m} = \frac{\dot{J}_p}{\dot{m}_p} = \frac{C_2 \rho_p w \int_{-b}^{b} (1-\varepsilon) v_p^2 dx}{C_1 \rho_p w \int_{-b}^{b} (1-\varepsilon) v_p dx} = \frac{C_2 \rho_p w \left(v_{p,m}^2 x_{p,1/2}\right) \int_{-2}^{2} (1-\varepsilon) f_p^2 d\xi}{C_1 \rho_p w \left(v_{p,m} x_{p,1/2}\right) \int_{-2}^{2} (1-\varepsilon) f_p d\xi}$$

$$= v_{p,m} \left[\frac{C_2 \int_{-2}^{2} (1-\varepsilon) f_p^2 d\xi}{C_1 \int_{-2}^{2} (1-\varepsilon) f_p d\xi} \right] \quad (6.39)$$

where f is a function that describes the shape of the normalized velocity profile for the respective phases. If the volume fractions are considered to be uniform across the jet cross-section and Gaussian velocity profiles are used, these expressions simply reduce to

$$V_{g,m} = \left(\frac{C_2}{C_1} \frac{1.5}{2.09} \right) v_{g,m} \quad (6.40)$$

$$V_{p,m} = \left(\frac{C_2}{C_1} \frac{1.5}{2.09} \right) v_{p,m} \quad (6.41)$$

and taking the ratio yields

$$\frac{V_{g,m}}{V_{p,m}} = \frac{v_{g,m}}{v_{p,m}} \quad (6.42)$$

Therefore, the mass-averaged velocity ratio for the two self-similar phase velocity profiles is equivalent to the ratio of the maximum velocities at a given streamwise location. This expression, combined with equations (6.33) and (6.36), suggests that the mass-averaged velocity ratio for the two phases tends to develop in a similar fashion for all high particle Reynolds number jet plumes and is governed by simple gas-particle drag coupling.

Note that the jet cross-sectional area, the 3D velocity gradient correction coefficients, nor the finite Gaussian integral values are present in equations (6.36) and (6.42). Thus, the observed velocity ratio trend should not be limited to the current fluidized bed riser geometry. Therefore, the axial distance is simply scaled with respect to the jet diameter in Figure 6.19, Figure 6.20, Figure 6.21, and Figure 6.22. However, as mentioned in the previous chapter, the lack of knowledge of a virtual origin for the velocity profiles would perhaps render any power-law curve fitting attempts arbitrary and therefore may not provide any additional physical insight on the jet dynamics.
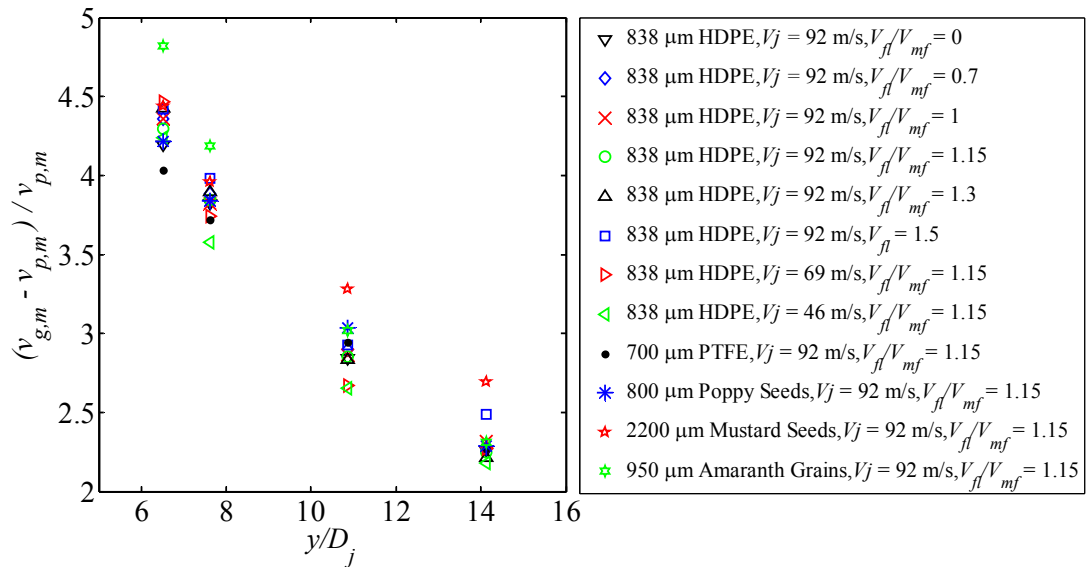

Figure 6.22: Ratio of the maximum velocity values for the slip and particulate phase for all cases. The ratio of maximum velocities appears to collapse along the same curve.

6.3 Chapter 6 References

P.E. Roach. "The penetration of jets into fluidized beds," Fluid Dynam. Res. **11** (5), 197-216 (1993).

CHAPTER 7:

CONCLUSIONS

7.1 Summary of Achievements and Contributions

From the literature, it is evident that there is a need for quantitative gas and particulate phase velocity measurements in jet plumes in bubbling fluidized beds. This information is needed to understand and model the transport phenomena that occur in this region of rapid mass and momentum transfer. The work presented in this dissertation describes the novel measurement technique and data analysis procedure employed to gain unique physical insight on these gas-particulate systems.

A non-intrusive LDV technique was developed to obtain the gas and particulate phase velocities simultaneously. LDV measurements of large bed particles are challenging because the inherent laser intensity fluctuations mix with the burst Doppler frequencies, producing spurious peaks that can contaminate the data. This issue was resolved by optimizing the Bragg Cell angle, laser beam diameter, the direction of fringe pattern propagation, and electronic band pass filter settings.

In order to obtain gas phase velocity measurements, the jet gas was seeded with ice crystal tracers, which were formed by rapidly cooling the humid jet air *via* a dry ice heat exchanger to approximately -5°C. This novel seeding technique is ideal for high speed gas phase measurements in fluidized beds since the ice crystals do not damage the viewing windows nor do they contaminate the particulate emulsion. LDV bursts from the bed particles and gas tracers were simultaneously acquired and differentiated based on their intensity and coincidence to determine the particulate and gas phase velocities. Measurements of this type have not been reported in the literature, to the author's knowledge.

Before attempting to quantify and analyze two-phase measurements in the bubbling bed jet plume, the behavior of the single-phase gas jet in the empty 2D bed was examined. The self-similar velocity profile growth was consistent the development of a free 2D turbulent jet. In addition to velocity profiles jet plume, the jet inlet velocity profile, bed gap velocity profile, and fluidization distributor velocity profiles were recorded. Coefficients to account for the velocity gradients across the width of the bed gap were calculated, which enabled accurate mass flow and momentum rates to be determined from the velocity profiles in the jet plume.

Once the vertical jet in the empty bed had been fully characterized, the bed was filled with high density polyethylene (HDPE) micropellets. These particles are considered Geldart Group B particles, which bubble immediately beyond minimum fluidization. The gas and particulate phase velocity profiles were presented and analyzed. This included similarity profile scaling as well as void fraction, mass flow, and momentum transport calculations. Furthermore, applying the Eulerian equation of motion to the particulate phase with the measured velocity profiles, the bed particle drag coefficient was recovered and was found to be consistent with the theoretical value.

Roach (1993) proposed that fluidization velocity has a first order influence on the jet dymanics and concluded that experiments with single jets over a wide range of fluidization velocity ratios are needed to further characterize and quantify this influence. Using the same batch of 838 μm HDPE miropellets and maintaining the same gas jet inlet conditions (V_j = 92 m/s and T_j = -5°C), the emulsion was fluidized at V_{fl}/V_{mf} = 0, 0.7, 1, 1.15, 1.3, 1.5. It was found that the maximum centerline velocity decreases and the velocity profile width increases for both phases with increasing fluidization.

As before, these data were then used to calculate volume fraction, mass flow, and momentum transport rates for each phase based on the Gaussian velocity profile shapes. The phase volume fraction in the jet plume is an important parameter that is often not considered to be a function of fluidization velocity. However, it was found that that void fraction has a strong dependency and increases with the fluidization state of the emulsion. The calculated gas phase mass flow rates suggest that that when the emulsion is fluidized below the minimum fluidization rate, gas originating from the jet inlet diffuses into the emulsion downstream to locally fluidize the particles as the gas phase mass flow

decreases downstream. Above the minimum fluidization rate, interstitial gas and bubbles in the emulsion are entrained into the jet plume as the gas phase mass flow increases downstream. Likewise, as the fluidization rate increases, the gas phase momentum increases due to increased interstitial gas entrainment. The particulate phase mass flow and momentum rates decrease with increasing fluidization due to competition with the increased interstitial gas entrainment.

It was noted that the ratio of the maximum velocities for the gas and particulate phases appeared to be independent of fluidization. This phenomena was further examined by carrying out experiments where 1) the particle emulsion and fluidization level is held constant and the jet velocity is varied and 2) the jet velocity and fluidization ratio is held constant and the bed particles are changed. These tests revealed that once again, the ratio of the gas to particulate phase centerline velocities is observed to collapse along the same curve. The non-intrusive, simultaneous gas and particulate phase measurements make the observation of the centerline velocity ratio trend possible.

A physical explanation as to why the Eulerian centerline velocity ratio seems to follow the same trend was explored. It was determined that the ratio of the drag force coupling to the particulate or gas phase momentum is constant at a given location downstream from the jet inlet. Additionally, the mass-averaged velocity ratio for the two phases, which is equivalent to the ratio of the centerline velocities, tends to develop in a similar fashion. This phenomenon is observed for high speed gas jets in bubbling beds with spherical particle entrainment when Re_p >1,000 so that C_D ~ 0.4. The jet cross-sectional area, the 3D velocity gradient correction coefficients, and the finite Gaussian integral values cancel out in this analysis, thus the observed velocity ratio trend should not be limited to the current fluidized bed geometry.

7.2 Future Work

Though this work is comprehensive and consistent, there is still more research to be done concerning gas jets in bubbling fluidized beds. The seemingly simplest continuation of this work would be to obtain velocity profiles with different types of particles in the emulsion. It would be ideal to vary particle properties such as size, shape, and density in a controlled manner. However, robust, non-abrasive particle types are

rare. The majority of particle types damage or foul the quartz viewing windows (*i.e.* glass and metal spheres) or breakdown (organic materials and polymerized spheres).

Along with mean velocity profiles, turbulence statistics are of interest in the jet plume. The effect of particle loading on turbulence levels in dilute circulating fluidized beds has been successfully studied using similar measurement techniques (Hadinoto *et al.*, 2005). Additionally, turbulence in particle laden jets has been measured and analyzed (Barlow & Morrison, 1990; Mergheni *et al.*, 2009). However, these experiments were carried out with free jets where the particles are fed into the jet nozzle tube. These unbounded, initial particle loaded jets configurations experience no particle entrainment and therefore are not analogous to jets in bubbling beds.

Finally, independent measurements of volume fraction profiles in the jet plume would be useful for verification the momentum averaged values obtained in this study, which could be done *via* x-ray densitometry.

7.3 Chapter 7 References

R. S. Barlow & C. Q. Morrison. "Two-phase velocity measurements in dense particle-laden jets," Exp. Fluids. **9** (1-2), 93-104 (1990).

K. Hadinoto, E.N. Jones, C. Yurteri, J.S. Curtis. "Reynolds number dependence of gas-phase turbulence in gas-particle flows." Int. J. Multiphase Flow **31** (4), 416–434 (2005)

M.A. Mergheni, J.C. Sautet, G. Godard, H. Ben Ticha, S. Ben Nasrallah. "Experimental investigation of turbulence modulation in particle-laden coaxial jets by Phase Doppler Anemometry." Exp. Therm Fluid Sci. **33** (3), 517-526 (2009)

P.E. Roach. "The penetration of jets into fluidized beds," Fluid Dynam. Res. **11** (5), 197-216 (1993).